



HAL
open science

Co-conception des systemes optiques avec masques de phase pour l'augmentation de la profondeur du champ : evaluation du performance et contribution de la super-résolution

Rafael Falcon Maimone

► **To cite this version:**

Rafael Falcon Maimone. Co-conception des systemes optiques avec masques de phase pour l'augmentation de la profondeur du champ : evaluation du performance et contribution de la super-résolution. Optique [physics.optics]. Université Paris Saclay (COMUE), 2017. Français. NNT : 2017SACLO006 . tel-01687374

HAL Id: tel-01687374

<https://pastel.hal.science/tel-01687374>

Submitted on 18 Jan 2018

HAL is a multi-disciplinary open access archive for the deposit and dissemination of scientific research documents, whether they are published or not. The documents may come from teaching and research institutions in France or abroad, or from public or private research centers.

L'archive ouverte pluridisciplinaire **HAL**, est destinée au dépôt et à la diffusion de documents scientifiques de niveau recherche, publiés ou non, émanant des établissements d'enseignement et de recherche français ou étrangers, des laboratoires publics ou privés.

NNT : 2017SACL0006

THÈSE DE DOCTORAT
DE L'UNIVERSITÉ PARIS-SACLAY
PRÉPARÉE INSTITUT D'OPTIQUE GRADUATE
SCHOOL

Ecole doctorale n°527

Electrical, optical, bio: physics and engineering (EOBE)

Spécialité de doctorat: Physique

par

M. RAFAEL FALCÓN MAIMONE

Co-conception des systèmes optiques avec masques de phase pour
l'augmentation de la profondeur du champ : évaluation de la
performance et contribution de la super-résolution

Thèse présentée et soutenue à Palaiseau, le 19 Octobre 2017.

Composition du Jury :

Mme. ANNE SENTENAC	Directrice de recherche Institut Fresnel	(Présidente)
M. JULIEN FADE	Maître de Conférences Université de Rennes 1	(Rapporteur)
M. JEAN-FRANÇOIS GIOVANNELLI	Professeur Université de Bordeaux	(Rapporteur)
M. FRÉDÉRIC CHAMPAGNAT	Maître de recherche ONERA	(Examineur)
Mme. CAROLINE KULCSÁR	Professeure Institut d'Optique	(Directrice de thèse)
M. FRANÇOIS GOUDAIL	Professeur Institut d'Optique	(Co-directeur de thèse)

“Fairy tales are more than true, not because they tell us that dragons exist, but because they tell us dragons can be beaten.”

Neil Gaiman

Acknowledgements

This manuscript is the culmination of three years of hard, creative and interesting work, made possible by the ADOPSYS project and the remarkable efforts of all its organizers. I am deeply thankful for what this project has given me, the opportunity to grow as a researcher, to learn state-of-the art science and to meet great professors and young scientists, many of which I now have the honor to call friends.

I would like to thank Caroline Kulcsár and François Goudail, my thesis co-supervisors. With their knowledge and wisdom, they have guided me throughout the years that lead to this work. It has been a difficult yet rewarding path, and I could not have done it without the support, insight and overall good vibes of the SPIM group members; from the professors to the interns, each one of them has helped me in their own way to succeed in this enterprise.

There is as well the incomparable support, love and trust of my family, who have always supported me in every endeavor I partake. My parents have always been my greatest inspiration; showing me that whatever we do in life, we should be sympathetic to others, always trying to be helpful and never put our wishes over the wellbeing of others.

There are no words to describe the importance my friends have had in my life. When one finds themselves so far from home, your friends truly become your family, giving you a hand in the times of sorrow but also sharing your greatest achievements. I could not leave out from these lines my dear Asia, who has been there for me from the first days of this wonderful journey and has, through her love and her patience, become the pillar that gives stability to my life. She is truly my best friend.

.....
The work reported in this manuscript is supported in part by the People Programme (Marie Curie Actions) of the European Union's Seventh Framework Programme (FP7/2007-2013) under REA Grant Agreement No. PITN-GA-2013-608082 (ADOP-SYS) that provides a PhD fellowship to Rafael Falcón.

Contents

Acknowledgements	v
Introduction	1
1 Phase masks for depth of field extension	5
1.1 Defocus on a conventional system	5
1.1.1 Wavefront propagation	5
1.1.2 Paraxial defocus	7
1.1.3 Effects of defocus on the response of a circular pupil	8
1.2 Depth of field extension via wavefront coding	9
1.2.1 Depth of field extension	9
1.2.2 Invariable MTF with a cubic phase mask	10
1.3 Definition of an image quality criterion and a deconvolution filter	12
1.3.1 Post-processing to improve the image quality	12
1.3.2 Image quality as optimization criterion	13
1.4 Co-design of phase mask and deconvolution	15
1.4.1 Finding an optimal mask	15
1.4.2 Principle of co-design	17
1.5 Conclusions	18
2 Performance limits of phase masks for DoF extension	19
2.1 Co-optimization of a binary annular phase mask	19
2.1.1 Binary annular phase masks for depth of field extension	19
2.1.2 Optimization methodology	20
2.1.3 Particle Swarm global optimization algorithm	22
2.1.4 Optimization results	23
2.2 Performance limits of binary annular phase masks	24
2.2.1 Image quality as a function of the ring radii	24
2.2.2 Performance of the optimal masks through the DoF range	25
2.2.3 Considerations on mask manufacture and design	27
2.3 Frequency response of the masks and deconvolution	28
2.3.1 Effective MTF	28
2.3.2 Frequency response as a function of the number of rings	29
2.4 Robustness of the BAPM performance	31
2.4.1 Sensitivity to aberrations	31
2.4.2 Robustness to scene model	34
2.4.2.1 Simulated scenes	34
2.4.2.2 Real scenes	36
2.4.3 Visual performance comparison	37
2.5 Conclusions	39
3 Optimization and evaluation of different mask shapes	41
3.1 Importance of the performance criterion	41

3.1.1	The Strehl ratio	42
3.1.1.1	Definition of the Strehl ratio	42
3.1.1.2	Strehl ratio as a performance criterion	42
3.1.2	Comparison of SR-based and MSE-based performance criteria	43
3.1.2.1	Image quality as a function of the defocus	43
3.1.2.2	Mean and minimum image quality criteria	45
3.1.3	Visual inspection	46
3.2	Continuous phase masks for depth of field extension	47
3.2.1	Polynomial phase masks	48
3.2.1.1	PPM optimization results	48
3.2.1.2	PPM performance comparison	49
3.2.2	Aspheric phase masks	50
3.2.2.1	APM optimization results	51
3.2.2.2	APM performance comparison	52
3.2.3	Free-form phase masks	52
3.2.3.1	FFPM optimization results	53
3.2.3.2	FFPM performance comparison	55
3.2.4	Comparison of all optimized masks	55
3.2.4.1	Different mask profile comparison	56
3.2.4.2	Performance comparison of different masks	56
3.2.4.3	Comparison at the full depth of field	57
3.3	Hybrid system response for different masks	58
3.3.1	Impulse response comparison	59
3.3.2	Frequency response comparison	60
3.3.3	Visual comparison of the frequency response	63
3.4	Conclusions	64
4	Aliasing of hybrid systems and superresolution	69
4.1	Effects of sampling on a conventional system	69
4.1.1	Sampling on a conventional system	69
4.1.2	Aliasing	71
4.1.3	Effects of sampling on image quality	74
4.1.3.1	Aliasing reduction by filtering	74
4.2	Superresolution	75
4.2.1	Superresolution model	75
4.2.2	Shift and add reconstruction	78
4.2.3	Simulation results	79
4.3	Superresolution for industrial inspection	80
4.3.1	Superresolution experimental setup	81
4.3.2	Assessment on the resolution improvement	82
4.3.3	Tests on industrial samples	83
4.3.3.1	Package molds	84
4.3.3.2	Silicon microcomponent	86
4.4	Phase masks for Dof extension and superresolution	88
4.4.1	Effects of the pixel size on the depth of field	88
4.4.2	Aliasing on phase masks	90
4.4.3	Superresolution and DoF extension	90
4.5	Conclusions	93
	General conclusions	95

Résumé de la these

99

Bibliography

111

A mi padre...

Introduction

Throughout the last century, the engineering scene has seen a surge of instruments, machines and methodologies inspired by nature. From simple things such as Velcro, mimicking the cockleburr's seeds, up to boat hulls covered in a sharkskin facsimile, scientists and engineers have implemented designs that took thousands of years of evolution to reach their current optimal form. One clear example of nature's optimization is the eye: its design varies dramatically between species, each adapted for the environment they live into maximize their survivability. But the eyes are far from a perfect imaging system; much of the work is done by the brain, processing what the eyes see. The evolution of vision happened simultaneously in the eye and the way the brain processes the signals it receives.

With the dawn of digital technologies and ever faster computers, we can now go beyond copying nature's designs and digitally optimize complex systems ourselves. Optical system design and image processing are two closely related disciplines that have benefited greatly from the digital era. Optical combinations passed from having a handful spherical lenses a hundred years ago to having couple dozens of aspherical lenses. Fast computing and efficient algorithms allow to process hundreds of images in just fractions of a second, allowing techniques such as real-time facial recognition, independent drone navigation and automated speeding tickets on the roads. Traditionally, optical systems are optimized to satisfy certain requirements and only then post-processing is constructed given the specifications of the optics.

The simultaneous co-design of the optical system and the post-processing algorithms, in order to have one that compensates for the shortcomings of the other, is analogous to our example of the evolution of the eye. Nature's main method for change is 'blind', random mutations discarding suboptimal results until a desirable performance is obtained. In optical design, the engineers have found optimization criteria that reflect their technological objectives and also account for the optical system's parameters. On the other hand, while in nature the most important performance evaluation is natural selection itself (Endler, 1986), in science and engineering the optical designer conceives performance evaluation tools to assess the results from optimizations.

In our work we focus on these evaluation tools in the context of co-design of phase masks and deconvolution for depth of field extension. In this technique, a wavefront encoding element, the phase mask, is placed in the aperture stop of an optical system to obtain a quasi-invariant point spread function across longer field depths than for the original system (Dowski and Cathey, 1995). This quasi-invariance to defocus usually blurs the final image, so that a deconvolution has to be applied (Cathey and Dowski, 2002). Because the deconvolution filter depends on the phase mask profile, a co-design approach is necessary to obtain an optimal performance (Diaz et al., 2009).

In the first chapter of this manuscript we develop the mathematical formalism that will allow us to jointly optimize phase masks and their deconvolution filter in the context of DoF extension. We begin by describing the defocus aberration and how the use of phase masks can make an optical system quasi-invariant to it. We continue by defining the Wiener-like deconvolution filter, which minimizes, on average over the considered depth of field, the error between the scene and the deconvolved image in a linear Gaussian framework. Then we define an optimization criterion, named image quality, which takes into account the contribution of both the phase mask and the filter. This criterion is used for the rest of the manuscript to evaluate the performance and compare different co-designed phase masks.

Chapter 2 focuses on the optimization and a thorough analysis of the performance of the binary annular phase mask, a phase plate with concentric rings of different phase value. We study the optimization process and its complications, which guided our choice of the optimization algorithm. We optimized the masks with an increasing number of rings for different ranges of depth of field extension. We have designed this optimization strategy so that we could answer original and fundamental questions in the co-design of binary masks, such as the amount of rings necessary for an optimal performance, their general performance limitations and how robust is their performance in the presence of unexpected residual aberrations.

The methodology applied for the optimization and analysis of binary annular phase masks in chapter 2 can be applied to any other mask model. In chapter 3 we first show that the performance criterion used to design the mask has an important impact on the obtained masks. We show that criteria such as the Strehl ratio and the MTF invariability can lead to suboptimal performances in terms of the image quality. We analyze and compare the performance of different continuous phase masks in terms of their number of parameters, profile shape and overall image quality and show that certain mask types are better adapted to different depth of field ranges. We draw a link between the final image quality and the modulation transfer function of the optical systems. We then show that phase masks behave as low-pass filters with a very distinct cutoff frequency, and that the Wiener filter only amplifies spatial frequencies lower than this cutoff.

The analysis of the frequency response of the phase masks becomes even more important when they are being used in optical systems that are not diffraction limited. The blur produced by the mask is then likely to interfere with techniques such as superresolution, which exploits the presence of aliasing in a series of undersampled images to reconstruct a high resolution image of the scene. In chapter 4 we explore this problematic. We start by defining the mathematical models and considerations used in superresolution process, which encompasses the shift and add superresolution algorithm (Elad and Hel-Or, 2001). Examples on real sequences illustrate the resolution improvement that can be obtained. In collaboration with our industrial partner, KLA-Tencor, we applied the shift and add algorithm to study the efficiency of this superresolution algorithm in the industrial inspection of electronic microcomponents. We show that thanks to superresolution, the resolution of their existing optics can be doubled and that the increase in resolution is enough to be able to observe defects on the microcomponents that would have been impossible to detect otherwise. Finally, we show the conditions necessary for superresolution to be possible when a phase mask optimized for depth of field extension is introduced in the system. We prove, for the first time to our knowledge, that resolution improvement

is possible thanks to superresolution techniques on image sequences obtained from a system designed for DoF extension using binary annular phase masks.

Chapter 1

Phase masks for depth of field extension

In the introduction we mentioned the need of tackling optical design problems with the post-processing in mind, so that one can maximize the desired output. In this chapter we study phase-only masks used for depth of field (DoF) extension. This concept was first introduced in (Dowski and Cathey, 1995), by using a cubic-phase mask to turn the point spread function (PSF) of an optical system invariant to defocus, with the side effect of deforming the PSF so that the final image is blurred. It was then refined in (Cathey and Dowski, 2002) to include a deconvolution filter that compensates for the blur and recovers the image quality.

In this chapter we follow the mathematical formalism developed in the work of (Diaz, 2011) and reach an image quality definition that allows us to optimize the mask shape and its deconvolution simultaneously. We first describe the wavefront error caused by defocus, we then introduce the concept of wavefront coding, that is, manipulating the wavefront shape at the pupil by means of a phase mask. We use these concepts to define a quality criterion for the processed image and the deconvolution filter that maximizes it. Finally, we show the importance of co-optimization by comparing the performance of masks obtained with different methods.

1.1 Defocus on a conventional system

1.1.1 Wavefront propagation

All conventional optical systems work under the same basic principle: the light coming from an object in the scene passes through a series of optical elements which generate an image on a photosensitive surface, namely, the detector. Let us consider a thin-lens system where a point in the object O is projected onto a point M in the image plane after passing through a lens set in the pupil plane at the point P , with angular coordinates (ρ_P, θ_P) , see Fig. 1.1.

The complex amplitude of a spherical wavefront that generated the point O at the pupil, before it passes through the lens, is given by the Huygens-Fresnel propagation principle:

$$A_O(P) = \frac{e^{-ikr_{OP}}}{r_{OP}}, \quad (1.1)$$

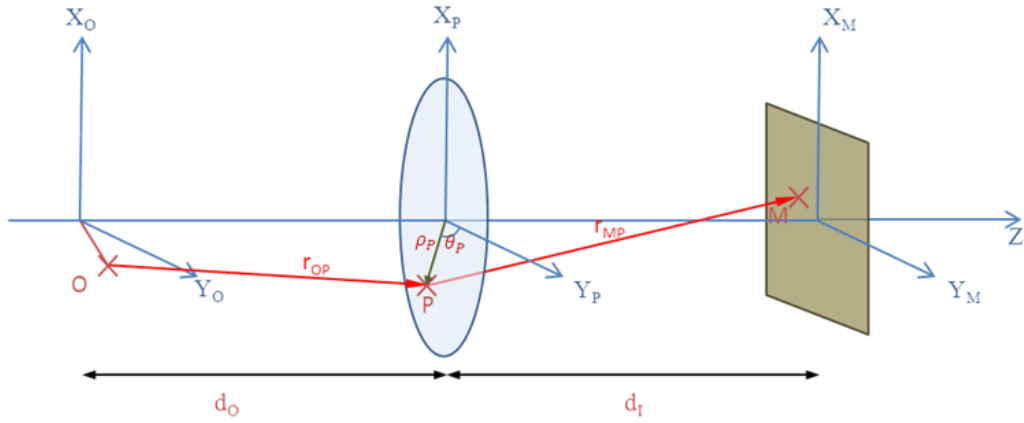


FIGURE 1.1: A conventional optical system. The point O of the object is projected through the point P in the lens onto the point M on the image plane

with $k = 2\pi/\lambda$ the wave number and r_{OP} the vector connecting O and P . After passing through the lens, the wavefront coming from the point P is shifted with respect to the light passing through the optical axis by a distance δ so that $(f + \delta)^2 = f^2 + \rho_P^2$, where f is the focal length of the lens (Fig. 1.2). This means that for any point P , after the lens, the amplitude is given by:

$$A_P(P) = A_O(P)e^{-ik\delta}. \quad (1.2)$$

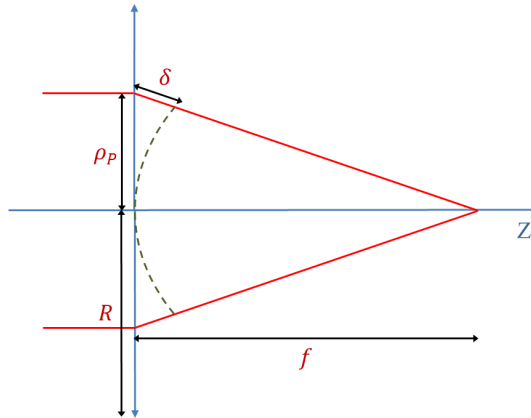


FIGURE 1.2: A lens shifts the wavefront leaving the point P by a distance δ , focusing it on the image plane.

The field amplitude at the point M in the image is given by the contribution of all points in the pupil coming from O , using equation (1.2) and $\delta = \sqrt{f^2 + \rho_P^2} - f$:

$$A(M) = -\frac{i}{\lambda} \iint S(x_P, y_P) \frac{e^{ikr_{OP}}}{r_{OP}} e^{-ik\sqrt{f^2 + \rho_P^2} - f} \frac{e^{-ikr_{PM}}}{r_{PM}} dx_P dy_P, \quad (1.3)$$

where $S(x_P, y_P)$ is the aperture of the pupil.

1.1.2 Paraxial defocus

If we consider ρ_P to be relatively small compared to the object and image distances, d_O and d_I respectively, the so-called paraxial approximation can be used:

$$r_{OP} \approx d_O + \frac{(x_P - x_O)^2 + (y_P - y_O)^2}{2d_O}, \quad (1.4)$$

$$r_{PM} \approx d_I + \frac{(x_M - x_P)^2 + (y_M - y_P)^2}{2d_I}, \quad (1.5)$$

$$\delta \approx \frac{\rho_P^2}{2f}. \quad (1.6)$$

By using equations (1.4), (1.5) and (1.6) in equation (1.3), we obtain:

$$\begin{aligned} A(M) &\approx -\frac{i}{\lambda} \frac{e^{ikd_O}}{d_O} \frac{e^{ikd_I}}{d_I} e^{\frac{ik(x_O^2 + y_O^2)}{2d_O}} e^{\frac{ik(x_M^2 + y_M^2)}{2d_I}} \\ &\times \iint S(x_P, y_P) e^{-ik \left[\left(\frac{x_O}{d_O} + \frac{x_M}{d_I} \right) x_P + \left(\frac{y_O}{d_O} + \frac{y_M}{d_I} \right) y_P \right]} e^{\frac{i\pi}{\lambda} \left(\frac{1}{d_O} + \frac{1}{d_I} - \frac{1}{f} \right) (x_P^2 + y_P^2)} dx_P dy_P, \end{aligned} \quad (1.7)$$

and thus the intensity in the image space:

$$I(M) \propto \left| \iint S(x_P, y_P) e^{-ik \left[\left(\frac{x_O}{d_O} + \frac{x_M}{d_I} \right) x_P + \left(\frac{y_O}{d_O} + \frac{y_M}{d_I} \right) y_P \right]} e^{\frac{i\pi}{\lambda} \left(\frac{1}{d_O} + \frac{1}{d_I} - \frac{1}{f} \right) (x_P^2 + y_P^2)} dx_P dy_P \right|^2. \quad (1.8)$$

We can recognize from the expression of Eq. (1.8) the impulse response of the optical system, which is the Fourier transform of the pupil function multiplied by an additional phase, centered in the image plane at the point $(x_M, y_M) = -d_I/d_O(x_O, y_O)$. The phase term can be identified as the optical path difference due to defocus aberration:

$$\psi = \frac{\pi R^2}{\lambda} \left(\frac{1}{d_O} + \frac{1}{d_I} - \frac{1}{f} \right), \quad (1.9)$$

with the coordinate normalization $x'_P = x_P/R$ and $y'_P = y_P/R$, where R is the radius of the pupil. Note that this equation can account for depth-of-field (d_I fixed and d_O variable) or depth-of-focus (d_I variable and d_O fixed) for the same value of ψ . Other aberrations can be introduced in the system in this way by making use of the Seidel coefficients and we will explore their effects more in-depth in chapter 2. The impulse response, better known as PSF, from a defocused system can now be rewritten as:

$$h_\psi(x_M, y_M) \propto \left| \text{FT} \left[S(x'_P, y'_P) e^{i\psi(x'^2_P + y'^2_P)} \right] \right|^2, \quad (1.10)$$

where FT denotes the Fourier transform. This expression for h_ψ shows the degradation of a point of the object after passing through a defocused optical system. Finally

the optical transfer function (OTF) $\tilde{h}_\psi(\mu, \nu)$ which is, by construction, the autocorrelation of the pupil function, represents the response in the spatial frequency domain, can also be defined as:

$$\tilde{h}_\psi(\mu, \nu) = \text{FT} [h_\psi(x_M, y_M)]. \quad (1.11)$$

By making use of equation (1.10) in (1.11), we obtain the expression of the OTF:

$$\begin{aligned} \tilde{h}_\psi(\mu, \nu) = & \iint S(x'_P + \mu, y'_P + \nu) e^{i\psi((x'_P + \mu)^2 + (y'_P + \nu)^2)} \\ & \times S^*(x'_P - \mu, y'_P - \nu) e^{-i\psi((x'_P - \mu)^2 + (y'_P - \nu)^2)} dx'_P dy'_P. \end{aligned} \quad (1.12)$$

where \cdot^* stands for complex conjugate. The modulus of the OTF is known as the modulation transfer function (MTF) and is denoted as $H_\psi(\mu, \nu) = |\tilde{h}_\psi(\mu, \nu)|$.

1.1.3 Effects of defocus on the response of a circular pupil

Most imaging optical systems present circular pupils, which makes it an interesting case to study the effects of defocus. For convenience, let us rewrite the field amplitude in equation (1.7) for a point at infinity:

$$A(M) \approx -\frac{i}{\lambda} \frac{e^{ikd_I}}{d_I} e^{ik(x_M^2 + Y_M^2)/2d_I} \iint S(x'_P, y'_P) e^{-ik(x_M x'_P + y_M y'_P)} e^{i\psi(x'^2_P + y'^2_P)} dx'_P dy'_P. \quad (1.13)$$

This gives, in polar coordinates:

$$A(M) \approx -\frac{i}{\lambda} \frac{e^{ikd_I}}{d_I} e^{ik(\rho_M^2/2d_I)} \iint_{0,0}^{2\pi,R} e^{-ik(\rho_M \rho_P (\cos \theta_M - \theta_P))} e^{i\psi \rho_P^2} d\rho_P d\theta_P, \quad (1.14)$$

$$\approx -\frac{2i\pi}{\lambda} \frac{e^{ikd_I}}{d_I} e^{ik(\rho_M^2/2d_I)} \int_0^R \rho_P J_0\left(\frac{k}{d_I} \rho_M \rho_P\right) e^{i\psi \rho_P^2} d\rho_P, \quad (1.15)$$

where $J_\alpha(x)$, $\alpha = 0$, is the zeroth-order Bessel function, which takes the form:

$$J_\alpha(x) = \sum_{n=0}^{\infty} \frac{-1^n}{n!(n+\alpha)!} \left(\frac{x}{2}\right)^{2n+\alpha}. \quad (1.16)$$

From equation (1.15), we can numerically calculate the PSF and the MTF of the optical system and evaluate the effects of defocus on the optical system. In Fig. 1.3 we see the comparison between the on-focus system ($\psi = 0$) and the system with a defocus of $\psi = 0.75\lambda$ and $\psi = 1.5\lambda$. Note that the defocus is normalized to units of wavelength as is any other phase magnitude throughout this manuscript.

As it can be noticed from Fig. 1.3 (top), the modulation transfer function of defocused systems has a stronger attenuation of high frequencies than the on-focus system;

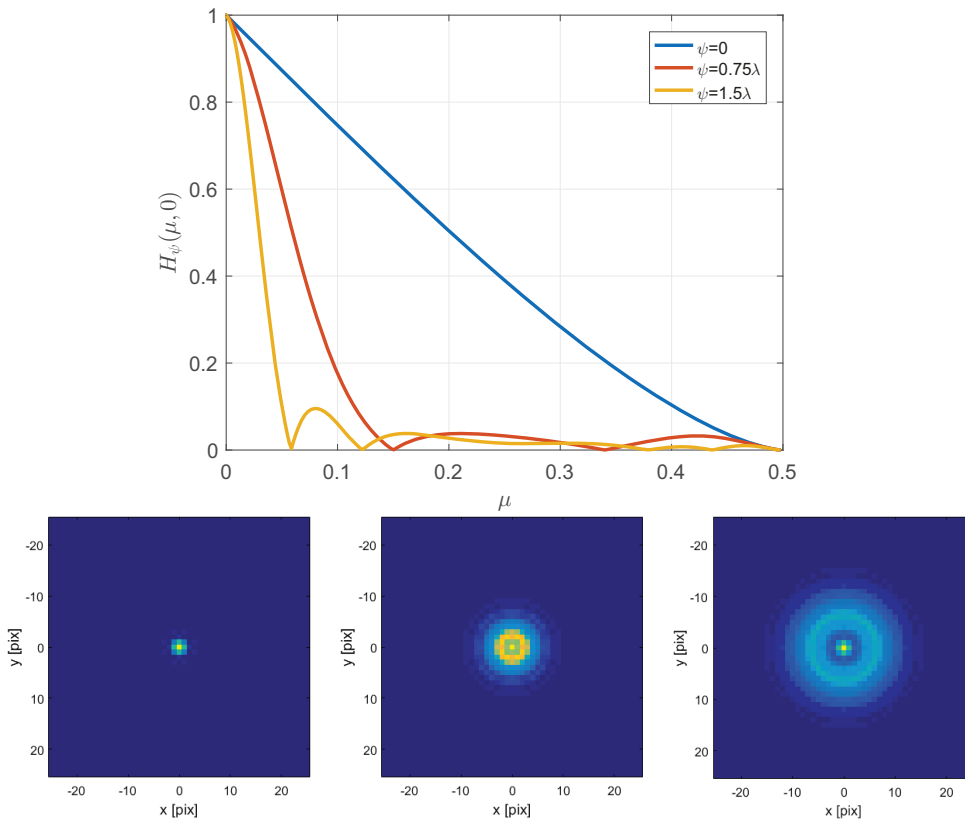


FIGURE 1.3: Top: modulation transfer function of a traditional optical system for defocus values $\psi = \{0, 0.75, 1.5\}\lambda$. Bottom: PSF of the same system affected by a defocus of values (left to right) $\psi = \{0, 0.75, 1.5\}\lambda$.

this means that the high-spatial frequency details on the scene will be blurred out. This blur is evident in the PSFs from Fig. 1.3 (bottom), where we can see that as ψ increases, a point in the object is projected as an increasingly broader spot on the image plane.

1.2 Depth of field extension via wavefront coding

1.2.1 Depth of field extension

The problematic of increasing the depth of field of an optical system has been the object of study for many years. The most common way to achieve this is by reducing the aperture of the optical system; as we can see in eq. (1.9), we can increase the value of d_O (or alternatively, d_i) and keep the wavefront error due to defocus ψ constant by reducing the value of the aperture radius R . This approach and many others where an amplitude mask is used in the pupil (Mino and Okano, 1971), (Ojeda-Castañeda, Andres, and Diaz, 1986) have the disadvantage of reducing the power reaching the detector, and thus, decreasing the signal-to-noise ratio (SNR) of the image. Before the proposal of phase-only masks for DoF extension, we could only find one work where the aperture was not apodized (Mino and Okano, 1971), but it

involved several expositions of the same scene and deconvolution with a different filter for each exposition.

The use of phase masks for wavefront coding was first introduced by Dowski and Cathey (Dowski and Cathey, 1995), where they propose the use of a cubic-profile phase mask, with no apodization, to turn the impulse response of an optical system invariant to defocus. In this way, the power reaching the detector is not reduced as with apodization. Additionally, since the system (and thus the PSF) is invariant to defocus, only a single deconvolution filter is needed for post-processing (Cathey and Dowski, 2002).

Using the approach of Dowski and Cathey, other works have proposed other phase-only mask profiles that achieve invariance of different optical quantities. For example, in (Castro and Ojeda-Castañeda, 2004) circularly asymmetric-profile masks are used to turn the axial intensity distribution at the image plane invariant to defocus, or in (Hu et al., 2013), where they utilize quartic-profile phase masks to make the Strehl ratio invariant to defocus.

1.2.2 Invariable MTF with a cubic phase mask

Let us now describe in some depth the approach of (Dowski and Cathey, 1995), where they consider a cubic phase mask to increase the depth of field. To show this we consider an optical system with a phase mask of profile $\varphi(x_P, y_P)$ on its pupil, the pupil $S(x_P, y_P)$ is then described by:

$$S(x_P, y_P) = \begin{cases} \frac{1}{\sqrt{2}} e^{i\pi\varphi(x_P, y_P)}, & (x_P^2 + y_P^2) < 1 \\ 0, & (x_P^2 + y_P^2) > 1. \end{cases} \quad (1.17)$$

In their work, Dowski and Cathey consider a rectangular-separable phase mask profile; this is a characteristic of cubic phase masks in particular and simplifies the mathematical demonstration, but it is not a requisite for depth of field extension. By making use of equation (1.12) one obtains the following expression for the OTF:

$$\begin{aligned} \tilde{h}(\mu) &= \int e^{i\pi\varphi(x_P+\mu/2)} e^{i(x_P+\mu/2)^2\psi} e^{-i\pi\varphi(x_P-\mu/2)} e^{-i(x_P-\mu/2)^2\psi} dx_P, \\ &= \int e^{i\pi\varphi(x_P+\mu/2)} e^{-i\pi\varphi(x_P-\mu/2)} e^{ix_P\mu\psi} dx_P. \end{aligned} \quad (1.18)$$

To follow the work of Dowski and Cathey, let us assume that we have a cubic phase mask in our pupil, defined as $\varphi(x_P) = \alpha x_P^3$, leading to

$$\tilde{h}(\mu) = \int e^{i\pi\alpha(x_P+\mu/2)^3} e^{-i\pi\alpha(x_P-\mu/2)^3} e^{ix_P\mu\psi} dx_P. \quad (1.19)$$

According to the stationary-phase approximation (Courant and Hilbert, 1965), if the phase term $i\alpha[(x_P + \mu/2)^3 - (x_P - \mu/2)^3]$ oscillates fast enough, the integral in eq.(1.19) can be approximated by its stationary term, giving as a result:

$$\tilde{h}(\mu) \approx \left(\frac{1}{12|\alpha\mu|} \right)^{1/2} \exp\left(i\pi \frac{\alpha\mu^3}{4}\right) \exp\left(-i \frac{\psi^2\mu}{3\pi\alpha}\right). \quad (1.20)$$

Equation (1.20) can be made insensitive to the defocus term ψ with a sufficiently large $|\alpha|$:

$$\tilde{h}(\mu) \approx \left(\frac{1}{12|\alpha\mu|} \right)^{1/2} \exp\left(i\pi \frac{\alpha\mu^3}{4}\right), \quad \text{for large } |\alpha|. \quad (1.21)$$

To illustrate this, we can see in figure 1.4 the MTF and the PSF of an optical system with a cubic phase mask of profile given by the parameter $\alpha = 10\lambda$, suffering different degrees of defocus. We can see that for all values of ψ , the MTFs is greatly degenerated as compared to the diffraction limited system, but the shapes are the same, as predicted by equation (1.21). We can also see in figure 1.4 the shape of the PSFs, which are quasi-invariant, but present a very strong deformation and is oriented towards the bottom right; these deformations create undesired blur in the image space, which can be corrected partially by digital deconvolution (Cathey and Dowski, 2002).

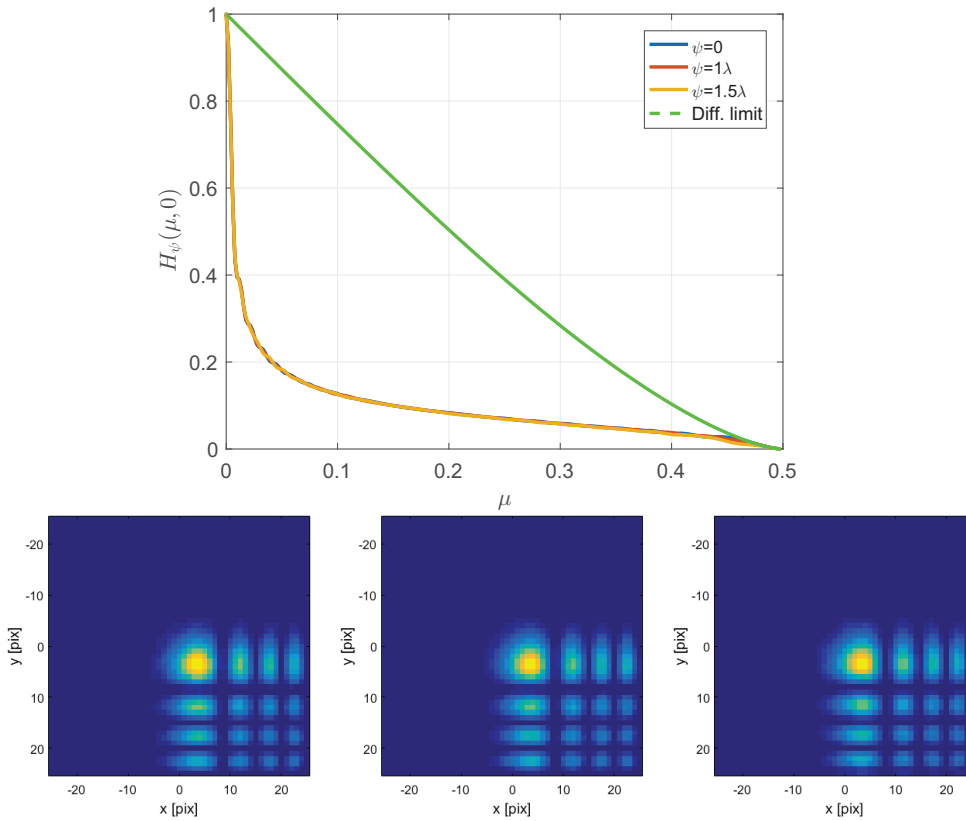


FIGURE 1.4: Top: modulation transfer function of an optical system with a CPM with $\alpha = 10\lambda$ for defocus values $\psi = \{0, 0.75, 1.5\}\lambda$; the dashed line represents the diffraction limit. Bottom: PSF of the same system affected by defocus of values (left to right): $\psi = \{0, 0.75, 1.5\}\lambda$, the MTFs and PSFs are quasi-identical for all defocus values

1.3 Definition of an image quality criterion and a deconvolution filter

Digital image processing is commonly used in optics to numerically process a captured image, to extract information or simply to make it more visually attractive. It is thus often used to increase the visual quality of images captured by an optical system that may have known optical defects. In this section we will introduce a numerical quantification of the image quality (IQ) and the deconvolution filter that maximizes it for a given optical system.

1.3.1 Post-processing to improve the image quality

Let us begin by mathematically describing the image produced by an optical system when captured by a digital detector. Given an object $O(x, y)$ in the scene and an optical system with PSF $h(x, y)$, the image captured by the detector can be defined as:

$$I(x, y) = h(x, y) * O(x, y) + n(x, y), \quad (1.22)$$

where $*$ is the convolution product and $n(x, y)$ represents the detection noise. The filter $d(x, y)$ that minimizes the mean squared error (MSE) between the object and the deconvolved image is the so-called Wiener filter (Wiener, 1949), defined in the frequency domain as:

$$\tilde{d}(\mu, \nu) = \frac{\tilde{h}(\mu, \nu)^*}{|\tilde{h}(\mu, \nu)|^2 + \frac{S_{OO}(\mu, \nu)}{S_{nn}(\mu, \nu)}}, \quad (1.23)$$

where $\tilde{\cdot}$ stands for the Fourier transform, $S_{OO}(\nu)$ and $S_{nn}(\nu)$ are the power spectral densities of the object and the noise respectively. In figure 1.5 we see a scene blurred by spherical aberration and the corrected image by use of a Wiener filter.



FIGURE 1.5: Example of an image blurred by spherical aberration (left) and the deconvolved image via a Wiener filter (right)

The Wiener filter could be used to deconvolve an image blurred by defocus, but because it depends on the PSF of the optical system, it can only work for a scene at a

specific defocus value ψ_i . In the following sections we will introduce a more adequate criterion than the standard MSE, to account for a broad range of DoF, together with the a filter that minimizes it.

1.3.2 Image quality as optimization criterion

In this subsection we will follow the mathematical derivations presented in the doctoral thesis of F. Diaz (Diaz, 2011) to obtain a relevant criterion for phase mask co-optimization for DoF extension. These derivations coincide with the results in previous works (Robinson and Stork, 2007), where the quality metric for optimization proposed is the mean squared error (MSE) between the object scene and the deconvolved image(s). This approach has the advantage, as we will see in the following, to take into account artifacts in the deconvolved image inherent to the optical system itself (e.g. aberrations), the detection (e.g. noise, sampling) and the deconvolution (e.g. noise amplification). For the sake of simplicity, we will not consider the effects of sampling until chapter 4.

Given the equation (1.22) we can define the deconvolved image as:

$$\widehat{O}(r) = d(r) * [h_{\psi}^{\varphi}(r) * O(r) + n(r)], \quad (1.24)$$

where h_{ψ}^{φ} is the PSF of a system suffering from a defocus ψ and with a phase mask of profile φ . We can now define the mean squared error:

$$MSE(\varphi, \psi) = \mathbb{E} \left[\int \left| \widehat{O}(r) - O(r) \right|^2 dr \right], \quad (1.25)$$

where $\mathbb{E}[\cdot]$ represents the mathematical expectation over the noise $n(r)$ and the object $O(r)$ which are both assumed to be zero-mean and independent stationary processes. For the sake of conciseness, all the mathematical developments are expressed using a 1D continuous formalism to represent the finite discrete 2D one, e.g., using the integral $\int \cdots dr$ to represent a finite double sum $\sum_{i=1}^L \sum_{j=i}^M \cdots$ over the pixels of the image. Under the assumption of independence between the scene and the noise, it can be demonstrated that, from equations (1.24), (1.25) and using the Plancherel theorem, we can rewrite the MSE as:

$$MSE(\varphi, \psi) = \int \left| \widetilde{d}(\nu) \widetilde{h}_{\psi}^{\varphi}(\nu) - 1 \right|^2 S_{oo}(\nu) d\nu + \int \left| \widetilde{d}(\nu) \right|^2 S_{nn}(\nu) d\nu. \quad (1.26)$$

Our goal is to find a deconvolution filter $\widetilde{d}(\nu)$ and a mask profile φ that minimize $MSE(\varphi, \psi)$ for any value of $\psi \in [\psi_{\min}, \psi_{\max}]$. For this purpose the averaged MSE can be defined as:

$$\overline{MSE}(\varphi) = \frac{1}{\psi_{\max} - \psi_{\min}} \int_{\psi_{\min}}^{\psi_{\max}} MSE(\varphi, \psi) d\psi. \quad (1.27)$$

For practical purposes, one does not integrate over all the values of ψ , but instead one averages over K values of $\psi_k \in \{\psi_1 = \psi_{\min}, \dots, \psi_K = \psi_{\max}\}$, leading to the redefinition of the averaged mean squared error:

$$\overline{MSE}(\varphi) = \frac{1}{K} \sum_{K=1}^K MSE(\varphi, \psi_k). \quad (1.28)$$

The *averaged* Wiener filter that minimizes eq.(1.28) is then deduced:

$$\tilde{d}_{\psi}^{\varphi}(\nu) = \frac{\frac{1}{K} \sum_k \left(\tilde{h}_{\psi_k}^{\varphi}(\nu) \right)^{\star}}{\frac{1}{K} \sum_{k=1}^K \left| \tilde{h}_{\psi_k}^{\varphi}(\nu) \right|^2 + \frac{S_{nn}(\nu)}{S_{oo}(\nu)}}. \quad (1.29)$$

One can use the averaged MSE from (1.28) as a criterion to co-optimize φ and d_{φ}^{ψ} , but the risk is to find an optimal $\overline{MSE}(\varphi, \psi)$ which has a very low $MSE(\varphi, \psi_k)$ value at some ψ_i but a very high one at another ψ_j . For this reason Diaz proposes using a *minimax* approach, where the criterion is:

$$MSE_{\max}(\varphi) = \max_k [MSE(\varphi, \psi_k)], \quad (1.30)$$

to be minimized over φ . In this way, the optimized mask profile φ will minimize the worse MSE in the range of ψ_k . Throughout this manuscript we will use an equivalent, yet more convenient, way to evaluate the performance of a hybrid optical system, which is the image quality:

$$IQ(\varphi, \psi) = \frac{E_O}{MSE(\varphi, \psi)}, \quad (1.31)$$

where E_O is the energy of the scene defined as $E_O = \int |O(r) - E[O(r)]|^2 dr$. Using this definition, equations (1.28) and (1.30) can be redefined in terms of image quality:

$$IQ_{\text{mean}}(\varphi) = \frac{E_O}{\overline{MSE}(\varphi)}, \quad (1.32)$$

$$IQ_{\text{min}}(\varphi) = \frac{E_O}{MSE_{\max}(\varphi)}. \quad (1.33)$$

Thus, the optimal mask profile can be defined as:

$$\varphi_{\text{opt}} = \arg \max_{\varphi} [IQ_{\text{crit}}(\varphi)], \quad (1.34)$$

with $IQ_{\text{crit}}(\varphi, \psi)$, corresponding to the chosen criterion IQ_{min} or IQ_{mean} . We will refer to the optimal image quality as:

$$IQ_{\text{opt}} = IQ_{\text{crit}}(\varphi_{\text{opt}}), \quad (1.35)$$

which is the image quality of the optimal mask.

At this point, we can notice that, unlike the work in (Dowski and Cathey, 1995) and (Zhao et al., 2014), where the objective was to make the PSF or the MTF (and consequently $MSE(\varphi, \psi)$) as invariant to defocus as possible, the optimization criteria of

equations (1.32) and (1.33) do not. In particular, the criterion from eq. (1.33) focuses instead on optimizing the value of $MSE_{\max}(\varphi)$ only for the the ψ_k with the worst image quality. This insures that $MSE(\varphi_{\text{opt}}, \psi)$, for any ψ in the desired DoF range, is always lower or equal to the $MSE(\varphi_{\text{inv}}, \psi)$ for a φ_{inv} obtained by methods that aim for invariability.

1.4 Co-design of phase mask and deconvolution

As we saw in section 1.2.2, it is possible to design a cubic phase mask that is guaranteed to produce an MTF invariable to defocus if the value of α is sufficiently high. Then we showed that a Wiener filter can be applied to recover the image quality. It has been shown that the invariability approach does not necessarily convey the best image quality of the post-processed image (Robinson and Stork, 2007), (Diaz et al., 2009). In this section we show the process of calculating the masks that is best for a given optimization problems using the mathematical definitions we have shown in section 1.3.2.

1.4.1 Finding an optimal mask

In order to illustrate the importance of co-design, we use as an example the cubic phase mask previously shown to turn the MTF invariant to defocus. To do this, we calculate the value of the criterion from eq. (1.33), that is $IQ_{\min}(\varphi)$, as a function of the parameter α of the cubic phase mask for a DoF range of $\psi \in [0, 1.5]\lambda$. As we can see in Fig. 1.6, the maximum value of the quality criterion for this specific co-design problem is at $\alpha_{\text{opt}} = 1.9\lambda$, far lower than the value $\alpha = 10\lambda$ required for an invariant MTF. It will later be shown, on chapter 2, that the MTF is not an ideal metric of performance when co-designing an optical system where a deconvolution step is required.

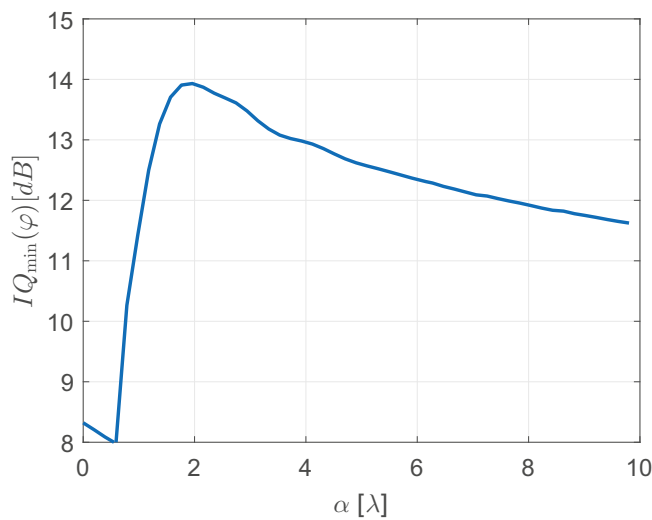


FIGURE 1.6: Plot of $IQ_{\min}(\varphi)$ as a function of the cubic mask parameter α

In Fig. 1.7, we show the MTFs and the PSFs of a system using a cubic phase mask with $\alpha = \alpha_{\text{opt}} = 1.9\lambda$ at the defocus values $\psi = \{0, 0.75, 1.5\}\lambda$. For comparison, according to the so called Rayleigh's quarter wavelength rule (Born, Wolf, and Bhatia, 1999), (Maréchal, 1947), in a classical diffraction limited optical system the effects of defocus are considered to be noticeable when $|\psi_{\text{max}}| \geq 0.25\lambda$. We can see that neither the MTF nor the PSF are now invariant to defocus and that slight variations exist for different values of ψ . This shows that, as proposed, invariability of the MTF does not necessarily convey optimal image quality results.

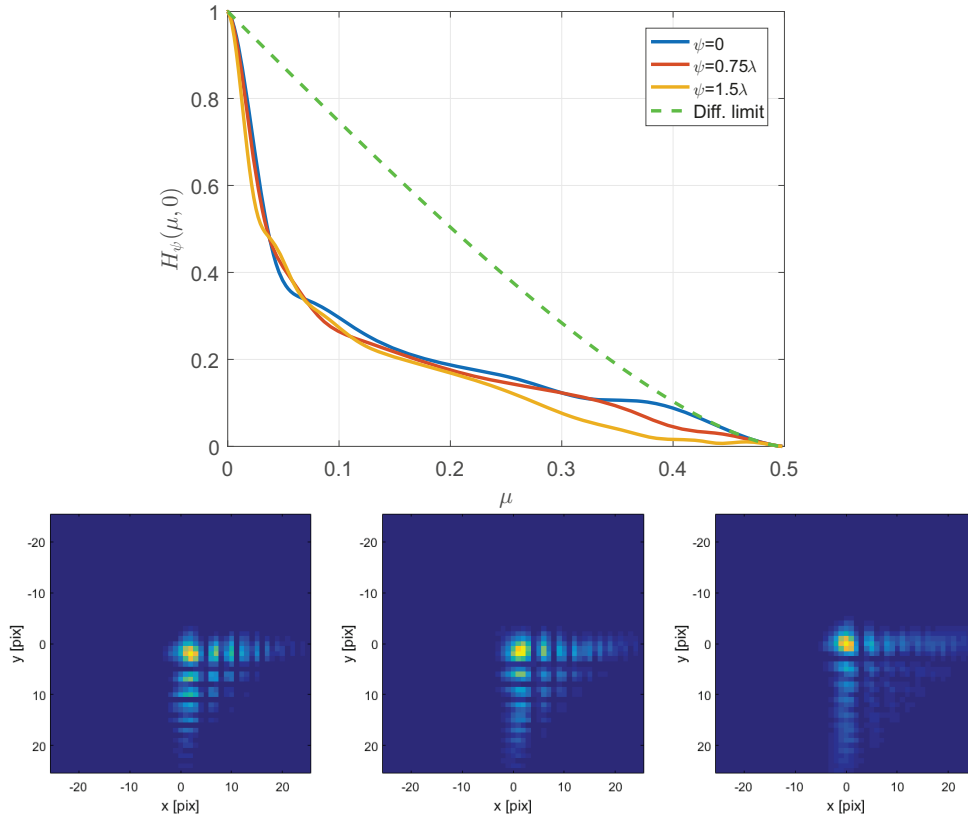


FIGURE 1.7: Top: modulation transfer function of an optical system with a CPM with $\alpha = 1.7$ for defocus values $\psi = \{0, 0.75, 1.5\}\lambda$, the dashed line represents the diffraction limit. Bottom: PSF of the same system affected by a defocus of, from left to right, $\psi = \{0, 0.75, 1.5\}\lambda$.

We see this in figure 1.8, where the mask designed for an invariant MTF has a much noisier deconvolved image than the mask co-designed for the desired DoF range ($\psi \in [-1.5, 1.5]\lambda$) to have the maximum value of $IQ_{\min}(\varphi)$.

For systems with multiple variables, the approach of calculating the value of IQ_{\min} for all values of the mask parameters used in this section is not possible due to computational times increasing exponentially with the number of variables. For this reason, to co-design an optical system for depth of field extension, an iterative joint-optimization has to be performed so that the phase mask and the Wiener filter are simultaneously modified on each optimization cycle.

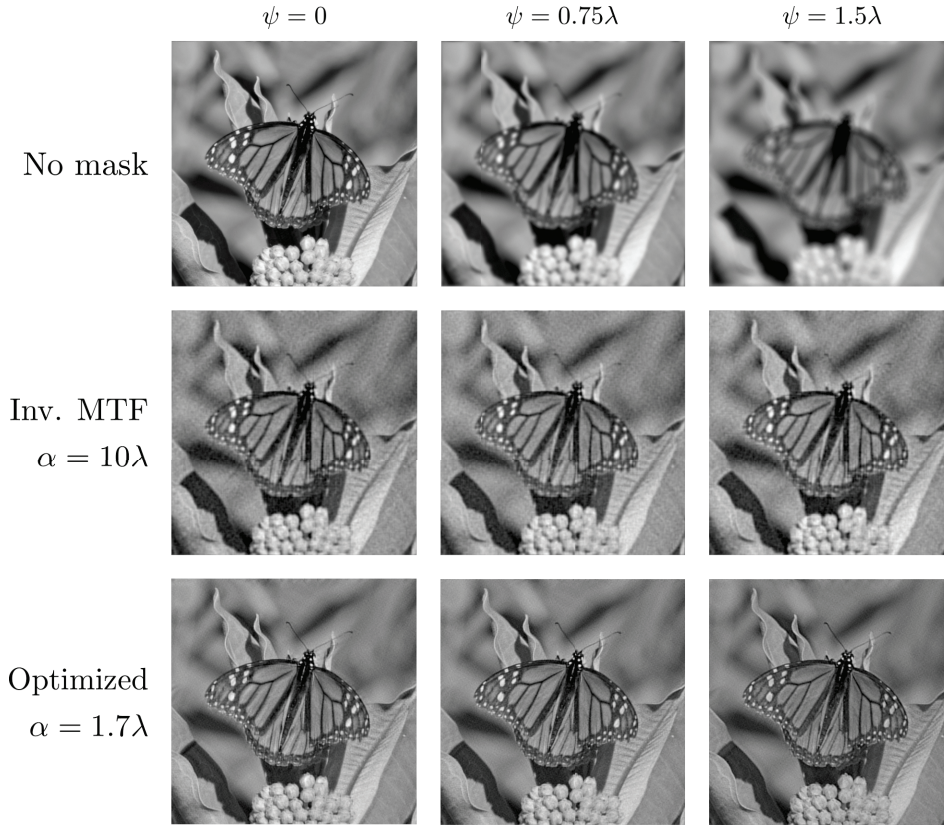


FIGURE 1.8: Comparison of images obtained under different degrees of defocus with: (top) a conventional system; (middle) a system with a CPM and deconvolution designed to have an invariant MTF; (bottom) a system with a co-designed CPM and deconvolution

1.4.2 Principle of co-design

As we have shown in the previous section, masks that aim for invariability may cause undesirable artifacts in the deconvolved image, as well as amplifying noise during deconvolution. For this reason and due to the complexity of the multi-variable problem, a joint optimization of the phase mask and the deconvolution filter has been proposed, in order to have the right compromise between DoF extension and noise amplification for a specific optical design problem (Diaz, 2011).

Figure 1.9 shows a flowchart with general steps for co-optimization of a phase mask and its deconvolution. We can see that on each cycle of the optimization loop, both the phase mask and the filter are modified, but the only variables are the mask parameters.

In reality, the optimization is performed without calculating the final images $\widehat{O}_{\varphi\psi_k}(r)$, since the quality criterion from equation (1.30) can be calculated faster by using equation (1.26) directly in the frequency domain.

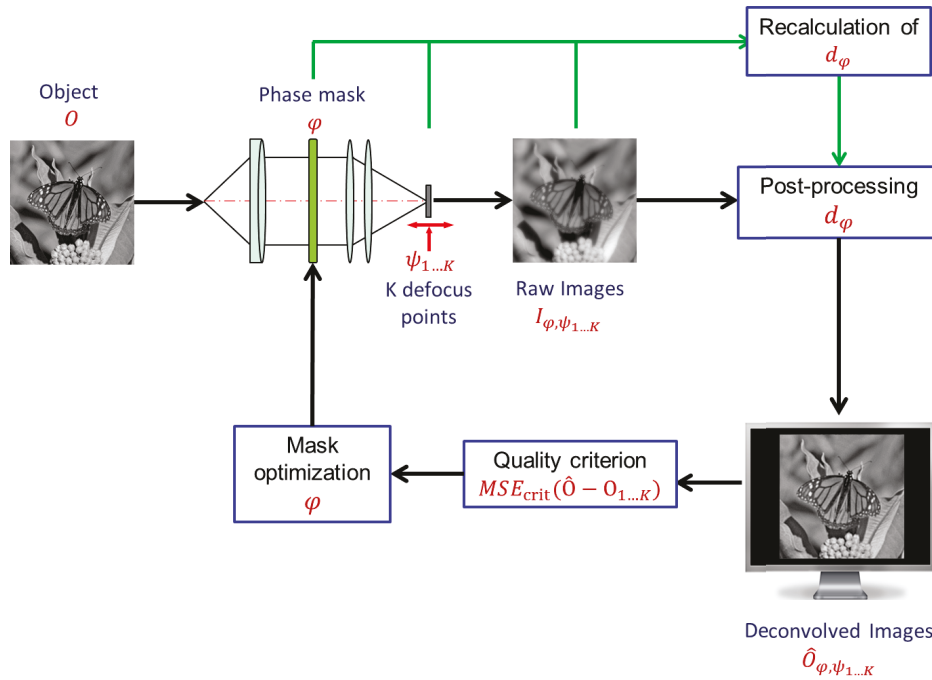


FIGURE 1.9: Co-design flowchart, showing the steps to optimize a mask and the deconvolution filter

1.5 Conclusions

Optical systems can suffer greatly from the blurring effects of aberrations, particularly from defocus. It has been shown that digital deconvolution can help mitigate these effects, as long as the aberration is known, but in the case of defocus it varies so greatly over the z -axis that a single deconvolution filter cannot be used. This is the interest of wavefront coding, where a phase mask in the pupil can be used to have an a PSF blur invariant to defocus, so that a single deconvolution filter can be used.

We have shown that this approach works, but masks that make the system invariant to defocus are not necessarily the optimal solution in terms of final image quality. Another approach was proposed, where the phase mask profile is co-designed taking into account the subsequent deconvolution, proving that a PSF that is only quasi-invariant to defocus is sufficient to be used for depth of field extension.

In systems with more parameters, a co-optimization is required to obtain the optimal mask, since a simple solution-map search like the one we used in this chapter would be impractical. In the following chapters we tackle the problem of optimization of a binary annular phase mask with multiple parameters, explore the characteristics of their optimization and study the range and limits of their performance.

Chapter 2

Performance limits of phase masks for DoF extension

In the previous chapter we have shown how a conveniently designed mask can modify the wavefront from an optical system to make it invariant to defocus. We have then demonstrated the importance of co-optimization of both the mask and the deconvolution, and that invariability of the MTF is not a requirement for optimal performance in terms of image quality.

In this chapter we now study the characteristics of binary annular phase masks (BAPM) and their depth of field (DoF) extension capabilities. These masks present various attractive features, such as a symmetric PSF and ease of manufacture. We will use the methodology described in chapter 1 to co-optimize the masks and their respective Wiener filter.

We first describe the characteristics of the binary annular phase masks which help us show the need of a global optimization algorithm. We provide an in-depth analysis of their performance and the limits they have. Finally we do thorough analyses of their robustness to different aberrations and scene models.

2.1 Co-optimization of a binary annular phase mask

In this section we study the main properties of the BAPM and compare them with other commonly used phase masks. This study then drives us to choose a global optimization algorithm that can deal with the different complications from the BAPM optimization landscape. Lastly, we analyze the mask profiles of the local optima found by the optimization.

2.1.1 Binary annular phase masks for depth of field extension

Binary annular phase masks consist of a series of N concentric annular regions of phase modulation of alternatively 0 or π radians at the nominal wavelength λ . Each annular constant phase area corresponds to what we will refer as *ring*, so that an N -ring mask of clear aperture radius R is parametrized by $N - 1$ normalized radius values $\varphi = \{\rho_1, \dots, \rho_{N-1}\}$, with $\rho = \rho'_p = \rho_p/R$ (Fig. 2.1).

To illustrate some of the features of the binary annular phase masks, in Fig. 2.2 we compare the monochromatic PSF of three different masks: the cubic mask obtained

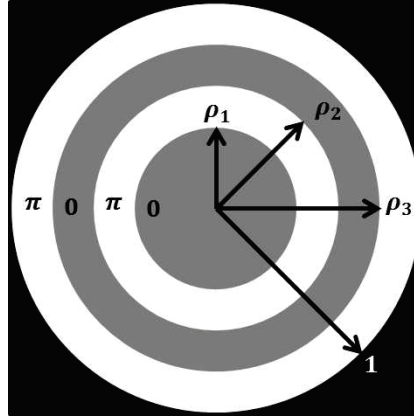


FIGURE 2.1: Example of a 4-ring annular binary phase mask. Gray areas induce a phase of $\varphi = 0$ and white areas a phase of $\varphi = \pi$.

in section 1.2.2, a quartic phase mask (QPM), a circularly symmetric mask which we will further study in Chapter 3, with profile $\varphi = \beta(\rho^4 - \frac{1}{2}\rho^2)$ and a BAPM. These three masks have been optimized for the DoF range $\psi_{max} = 1.5\lambda$. In Fig. 2.2 (top) we show a cut at the X_M axis of the PSF around the focal point as a function of the defocus ψ , In Fig. 2.2 (bottom) we show the PSF at $\psi = 0$.

A characteristic of circularly symmetric masks is that they always produce an equally circularly symmetric PSF around the Z-axis. In contrast, most non-circularly symmetric phase masks, such as the CPM, have the heavily skewed PSFs. This skewing comes with a shift of the center of the PSF as a function of ψ , as we can appreciate on the cut across X_M of Fig. 2.2 for the CPM.

We can see that the PSF of the QPM is not symmetric as a function of ψ around $\psi = 0$, while the CPM and BAPM are symmetric. Most circularly symmetric masks have asymmetric PSFs as a function of ψ . This is not the case of the BAPM, since the rings have precisely 0 or π phase steps, with $-\pi = \pi$ modulo 2π and therefore the BAPM can be considered to behave as what is commonly called an *odd profile mask*. Odd masks have the property that $\varphi(x, y) = -\varphi(-x, -y)$, and therefore the value of the PSF in equation (1.10), is the same for positive or negative values of ψ . Although this analysis is only valid for monochromatic light, phase masks have been used in common wave bands, like near infrared (Diaz et al., 2011) and visible (Burcklen et al., 2015).

As we can see, the binary annular phase masks present a series of attractive features for co-design, such as the circularly symmetric PSF, which makes the subsequent deconvolution less prone to visual artifacts. Finally, in practical terms, BAPMs are also considerably easier to manufacture than other mask types: their binary profile makes them very simple to manufacture by means of photolithography in contrast to continuous masks and, particularly for non-rotationally symmetric mask profiles, conventional diamond turning would be impossible to use.

2.1.2 Optimization methodology

In this section we present the optimization of BAPM using the ring radii φ as optimization parameters for a given DoF range ψ_{max} and a given number of rings N .

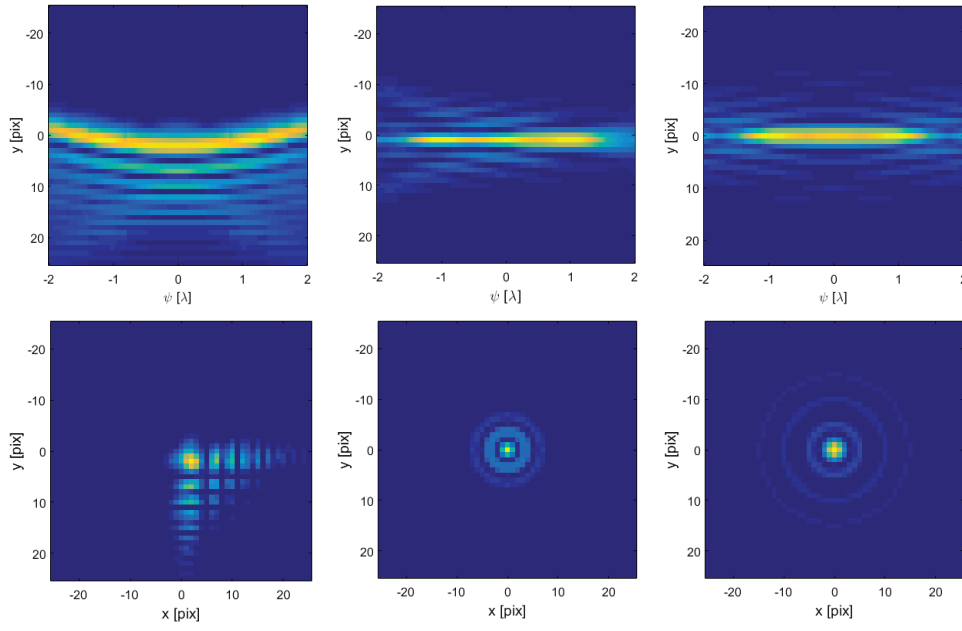


FIGURE 2.2: Comparison of the PSF of three different masks, from left to right: Cubic phase mask, quartic phase mask and binary annular phase mask. On top we see a cut across at $X_M = 0$ of the PSF for defocus values in the range $\psi = [-2, 2]\lambda$. On the bottom we see a cut at $\psi = 0$ of the three PSF

Since binary annular masks introduce a phase modulation of 0 or π radians and as the optical system is aberration-free, the value of $IQ(\varphi, \psi)$ is symmetric around the focal point $\psi = 0$. Thus, to save computational time, our optical system is optimized only for positive values of $\psi \in \{\psi_1 = 0, \dots, \psi_K = \psi_{\max}\}$ with the underlying assumption that the total DoF range is $[-\psi_{\max}, +\psi_{\max}]$ around the focal point. The evaluation points of the DoF range are chosen such that they are evenly spaced and that $\psi_k - \psi_{k-1} = 0.5\lambda$, this step size has been observed to be sufficient to obtain a near-optimal mask profile for a given ψ_{\max} .

To calculate the MSE from Eq. (1.26) and the filter from Eq. (1.29) we use a generic ideal scene model with a power-law PSD (Ruderman, 1997) $S_{oo}(\nu) = G\nu^{-a}$, with a being fixed to 2.5 and the constant G being given by the SNR value assuming $\int S_{nn}(\nu)d\nu = 1$.

The optimization of the mask with profile φ is not simple since the function $IQ_{\min}(\varphi)$ (Eq. (1.33)) presents several local maxima and is highly nonconvex. This is clearly seen in Fig. 2.3 (left), where we have represented the value of $IQ_{\min}(\varphi)$ for a 2-ring mask as a function of the radius ρ_1 and for different values of ψ_{\max} . It can be noticed that depending on the value of ψ_{\max} , there may be several local maxima of $IQ_{\min}(\varphi)$. Moreover, these local maxima have very similar values for a given value of ρ_1 in the range $\psi_{\max} \in \{2.0, 2.5, 3.0\}\lambda$. Similarly, we have represented in Fig. 2.3 (right) the variation of $IQ_{\min}(\varphi)$ for a three-ring mask as a function of ρ_1 and ρ_2 for $\psi_{\max} = 2.0\lambda$; the most prominent local maxima are marked with black crosses, many of them presenting similar values of $IQ_{\min}(\varphi)$.

To optimize binary phase masks with a larger number of rings, a graphical representation of $IQ_{\min}(\varphi)$ is no longer possible and therefore a global optimization algorithm is needed.

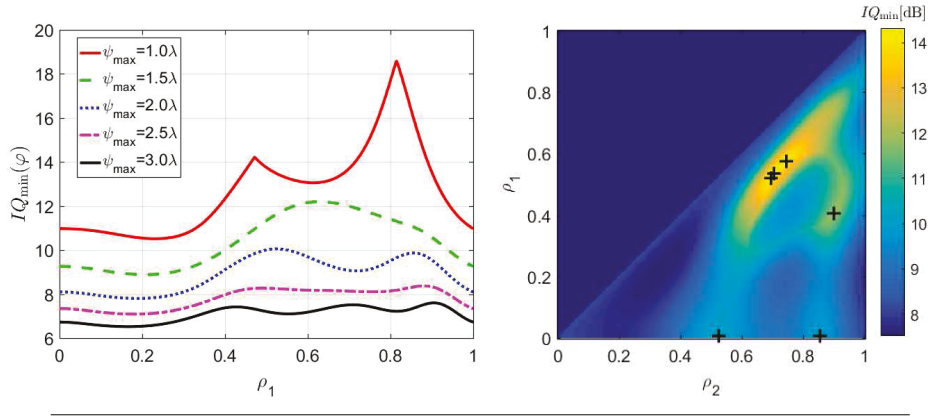


FIGURE 2.3: Evolution of $IQ_{\min}(\varphi)$ for (left) 2-ring masks calculated for $\psi_{\max} \in [1.0, 1.5, 2.0, 2.5, 3.0]\lambda$ and (right) 3-ring masks for $\psi_{\max} = 2.0\lambda$; the crosses mark the most prominent local maxima.

2.1.3 Particle Swarm global optimization algorithm

For all optimizations in this manuscript we have chosen the population-based Particle Swarm algorithm (Shi and Eberhart, 1998). This algorithm is commonly used in multi-variable optimizations that contain non-convex, non-derivable optimization landscapes and has been used in the design of optical elements such as gratings (Shokooh-Saremi and Magnusson, 2007), antenna array design (Gies and Rahmat-Samii, 2003) and design and manufacture of electronic and mechanic components (Yıldız, 2009).

The particle swarm global optimization consists of a collection of M particles with a random uniform distribution within the lower bound (lb) and upper bound (ub) of our optimization problem, $lb = 0$ and $ub = 1$ for BAPMs. The algorithm also gives each particle an initial position x_0^i and a velocity v_0^i . At each iteration j the position $p^i = x_j^i$ is updated as the position with the best value of the objective function the particle i has found, and the best position found over all particles is stored in d_j .

At each iteration, the particles move within the optimization landscape with a speed v_j^i ,

$$v_j^i = W_j * v_{j-1}^i + y_1 u_1^i (p^i - x_j^i) + y_2 u_2^i (d_j - x_j^i), \quad (2.1)$$

where u_1^i and u_2^i are normalized uniformly distributed random vectors of length N , y_1 and y_2 are the *self adjustment weight* and *social adjustment range* respectively, and are set by the user before the optimization begins, in order to manipulate the influence of the neighbors in the particle's speed. $W_j \in [0.1, 1.1]$ is an *inertial weight*, it decreases as the algorithm progresses and increases with the number of stagnant iterations, meaning iterations with relative change in the value of the objective function $b_j = MSE_{\max}(d_j)$ below a certain threshold.

The termination of the optimization loop is triggered when a certain number of stagnant iterations is reached. Alternatively, the optimization stops when a maximum number of optimization cycles is reached, but this scenario is unlikely and generally undesirable.

2.1.4 Optimization results

The randomness of the algorithm added to the complexity of the optimization problem makes it not always possible to find the global maximum in a single optimization run. For this reason, a large number of optimization runs, with randomly generated starting points, were calculated in parallel on a 48 core cluster of computers, leading to up to 40 different local maxima found, depending on the complexity of the optimization landscape. After multi-hour computations with computation time increasing with N , the best obtained masks for each case were then selected as optimal.

We have noticed that the number of local maxima of the optimization landscape increases along with the number of rings. It also starts to increase with the required DoF range, it reaches its maximum value for ψ_{\max} around 2.0λ and then slightly decreases when ψ_{\max} reaches 2.5λ as the optimization landscape becomes smoother. Similarly to the cases shown in Fig. 2.3, different mask shapes with very similar $IQ_{\min}(\varphi)$ values were found. As an example, we show in Fig. 2.4 two of the best masks obtained for 6 rings and $\psi_{\max} = 2.5\lambda$. These masks have different shapes but very similar image quality. This being said, we can observe that the last ring of Fig. 2.4.b is very thin so that from a technological point of view, the mask in Fig. 2.4.a would certainly be easier (or cheaper) to manufacture.

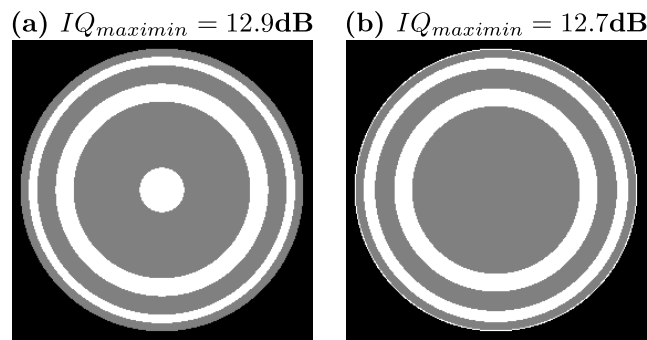


FIGURE 2.4: Comparison of two equivalent local maxima of $J(\varphi)$ obtained by optimization for 6-ring masks and for $\psi_{\max} = 2.5\lambda$.

Some global pattern can be observed on the shapes of the optimal masks as ψ_{\max} and the number of rings increase. In Fig. 2.5 we show the profiles of the optimal masks obtained for DoF ranges $\psi_{\max} = 2.0\lambda$ and 2.5λ , with 5, 6 and 7 rings each. A similar feature on all the masks is a wide annular region between two rings at $\rho_{k-1} \cong 0.60$ and $\rho_k \cong 0.75$. We can see that, for a given DoF, when the number of optimization parameters (rings) increases, the masks have similar profiles with the new rings appearing after the aforementioned annular region. This can probably be related to the parabolic shape of the wavefront error due to defocus, with the central part being relatively flat and thus not requiring to be engineered to enhance the image quality.

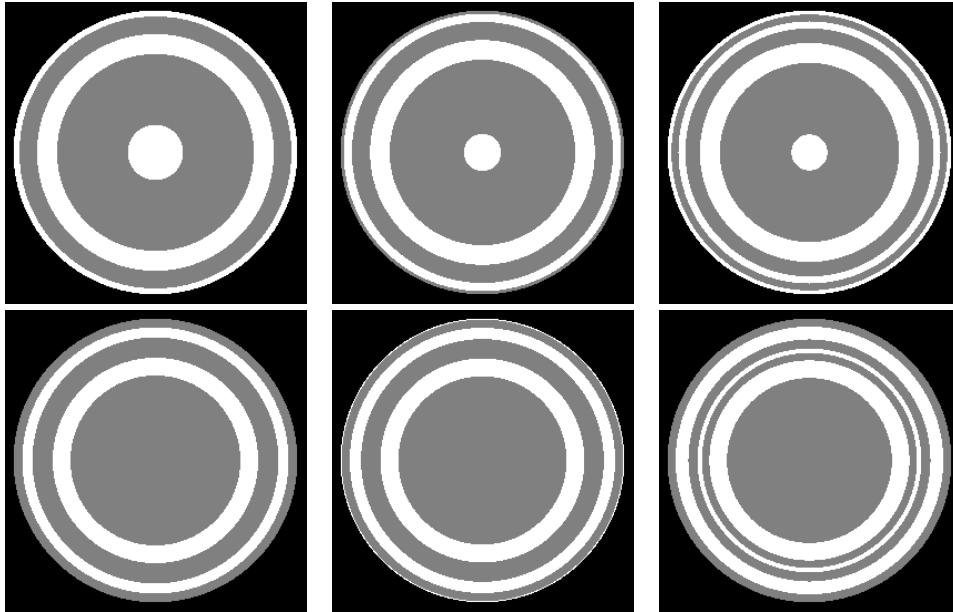


FIGURE 2.5: Masks optimized with (from left to right) 5, 6 and 7 rings and for DoF ranges $\psi_{\max} = 2.0\lambda$ (top row) and $\psi_{\max} = 2.5\lambda$ (bottom row).

2.2 Performance limits of binary annular phase masks

We now evaluate the performance of the BAPM we have optimized with the method shown in Section 2.1.2. We do so by observing the changes in the performance obtained by using an increasing amount of rings at a given DoF range. This study will help us identify what are the limits in DoF extension of binary annular phase masks and how these limits are affected by the number of rings.

2.2.1 Image quality as a function of the ring radii

In most optimization problems, increasing the number of parameters that are optimized automatically increases the value of the performance criterion. In the case of DoF extension via phase masks, it is therefore reasonable to suppose that increasing the number of rings would allow the co-designed system to reach higher DoF or to improve the image quality achievable.

In this section we evaluate the behavior of IQ_{opt} as a function of the number of rings for different values of ψ_{\max} , the values obtained can be seen in Fig. 2.6. We observe that the image quality naturally increases as more rings are added, but rapidly levels off in all cases. Take the case when $\psi_{\max} = 1.0\lambda$, the increase on IQ_{opt} from 2 to 3 rings is of $[\Delta IQ]_{2 \rightarrow 3} = 0.92\text{dB}$, a considerable gain in this range, but adding extra rings does not increase significantly the image quality.

When $\psi_{\max} = 1.5\lambda$, the overall behavior of IQ_{opt} as a function of the number of rings is the same as for $\psi_{\max} = 1\lambda$, with the difference that the value of IQ_{opt} is lower at all points. Another important difference is that last significant gain of quality happens when passing from 3 to 4 rings, for a value of $[\Delta IQ]_{3 \rightarrow 4} = 0.55\text{dB}$, leveling-off afterwards.

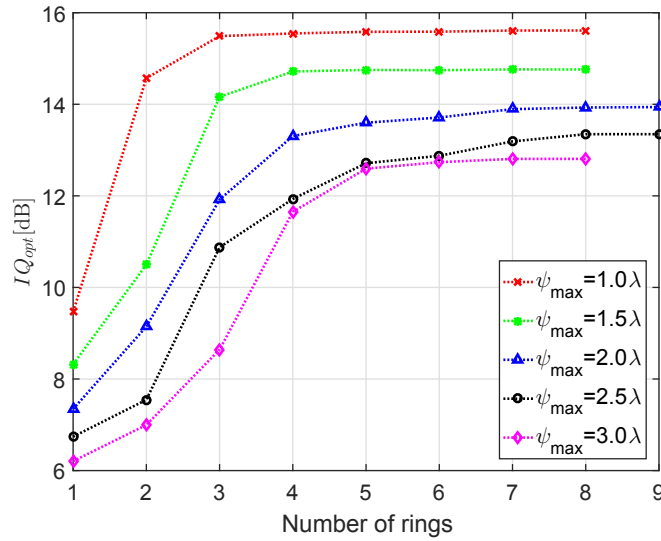


FIGURE 2.6: Performance comparison of optimal annular phase masks with different amount of rings for $\psi_{\max} \in \{1.0, 1.5, 2.0, 2.5, 3.0\}\lambda$. The case where the number of rings is equal to 1 is equivalent to having no mask.

The increase in performance between 3 and 4 rings becomes larger when the DoF increases, $[\Delta IQ]_{3 \rightarrow 4} = 1.4\text{dB}$ for $\psi_{\max} = 2.0\lambda$, $[\Delta IQ]_{3 \rightarrow 4} = 1.8\text{dB}$ for $\psi_{\max} = 2.5\lambda$ and $[\Delta IQ]_{3 \rightarrow 4} = 3.0\text{dB}$ for $\psi_{\max} = 3.0\lambda$. This trend clearly shows a need for extra rings as ψ_{\max} increases.

However, for all values of ψ_{\max} , a saturation of the performance with the number of rings is observed. When $\psi_{\max} = 1.0\lambda$, it occurs after 3 rings and for $\psi_{\max} = 1.5\lambda$, after 4 rings. When $\psi_{\max} = 2.0\lambda$, the behavior is slightly different, since the growth of IQ_{opt} slows down gradually, until it stops at 7 rings. The case of $\psi_{\max} = 2.5\lambda$ is somehow more intricate, but, again, shows no practical improvement after 7 rings.

This behavior seems to be due to the optimization landscape being the most nonconvex and prone to local maxima at values of ψ_{\max} around 2.0λ . On the other hand, when $\psi_{\max} = 3.0\lambda$, the IQ stops increasing as soon as with 5 rings, with a rather low IQ maximal value. This shows that we have reached a limit on how much the DoF of a system can be extended with an annular binary phase mask and a mean Wiener filter, regardless of how complex that mask is.

2.2.2 Performance of the optimal masks through the DoF range

To understand better the behavior of the hybrid imaging system throughout the DoF range, it is useful to see the evolution of $IQ(\varphi_{\text{opt}}, \psi)$ as a function of ψ . This is shown in Fig. 2.7 for the masks obtained for the DoF ranges of $\psi_{\max} = 1.5, 2.0, 2.5$ and 3.0λ , and for different numbers of rings.

The first observation is that, as ψ_{\max} increases from one graph to the next, all curves get lower values for a given number of rings. This indicates that, as ψ_{\max} increases, the problem becomes more difficult and the reachable optimal performance decreases.

When $\psi_{\max} = 1.5\lambda$, it is seen that all the curves for more than 4 rings yield a quasi-constant performance throughout the DoF range and are almost identical. This is consistent with the fact, observed in Fig. 2.6, that for this DoF range, the increase of performance levels off after 4 rings. When $\psi_{\max} = 2.0\lambda$, the variation of IQ as a function of ψ is wider; we observe a drastic change of the curve shape between 3-ring and 4-ring masks, then the curves are smoother and become flatter, to reach a stable behavior from 7 rings onwards.

When $\psi_{\max} = 2.5\lambda$, the performance of the 5-ring and 6-ring masks is very similar, but adding a 7th ring makes it possible to suppress the valley around $\psi = 0.72\lambda$ while following the path of the 6-ring mask afterward; this leads to the small increase of IQ_{opt} observed for this value of ψ_{\max} when going from 6 to 7 rings. When $\psi_{\max} = 3.0\lambda$, we see that the mask with 3 rings is clearly insufficient to compensate for such a large value of the defocus, and all the optimized masks have a similar performance after 5 rings.

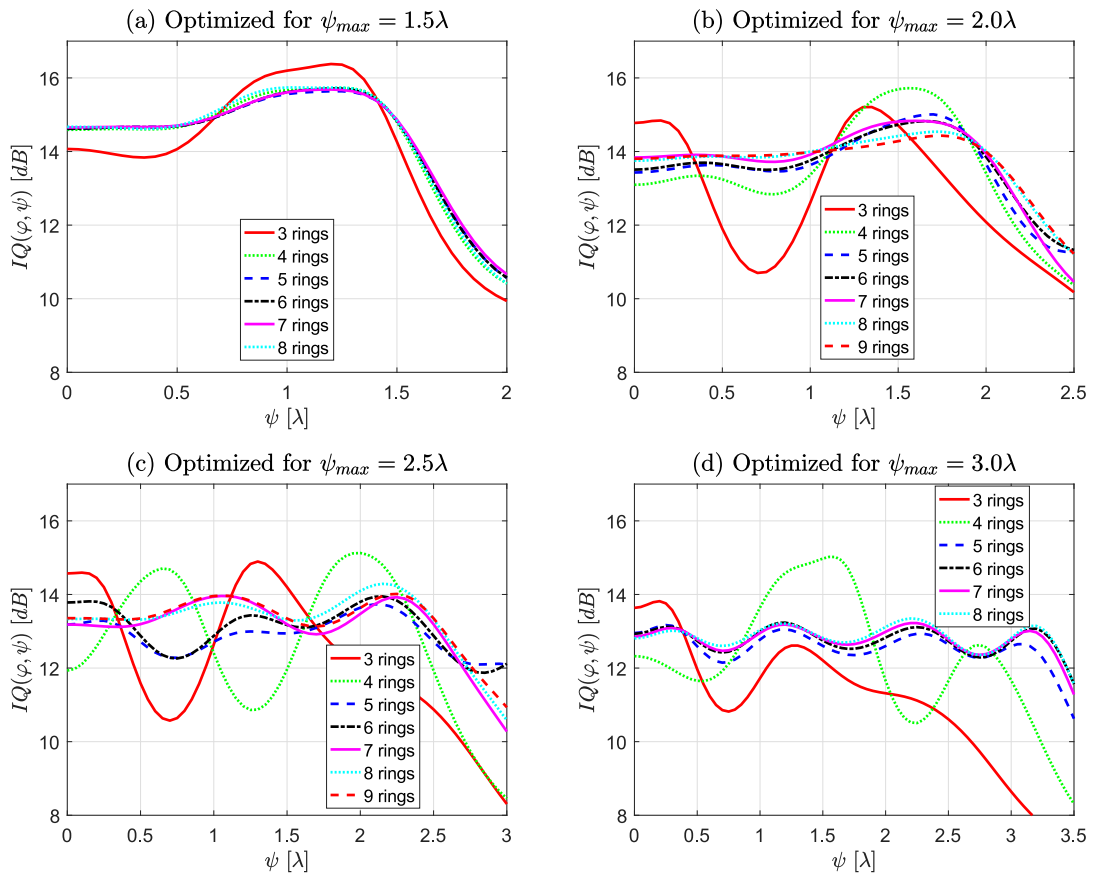


FIGURE 2.7: Performance comparison of masks optimized for different ψ_{\max} and number of rings as a function of ψ .

Finally, it is interesting to notice that in all cases, increasing the number of rings tends to reduce the peak to valley variation of $IQ(\varphi, \psi)$ even if it does not increase considerably the minimum of $IQ(\varphi, \psi)$ compared to the situation with less rings.

2.2.3 Considerations on mask manufacture and design

Binary annular phase masks optimized for DoF extension have been manufactured for different imaging applications, such as extending the DoF of non-cooled infrared cameras (Diaz et al., 2011), or athermalization of high definition cameras in the visible spectrum (Burcklen et al., 2015). The process of manufacture and implementation depends greatly on the application, since the manufacturing method will depend on constraints such as the spectral range and the usable materials, the pupil size of the targeted system and the cost of the manufacturing. Many manufacturing methods can be envisaged, such as direct diamond turning, molding, photolithography associated with chemical, plasma or reactive ion etching, effective index sub-wavelength patterning, among others. Each method has its own limitations in terms of materials that can be etched, on the minimal lateral size of the pattern that can be imprinted, on the maximum depth of the etch, and on the overall area that can be worked at affordable cost or within a realistic duration.

Since the masks we optimize in this chapter depend only on the DoF range ψ_{\max} and N , the number of rings, they can be used for systems working at any wavelength or pupil diameter. For example, let us consider a system with effective focal length $f = 20$ mm and F-number $F\# = 2$. If the spectral operating range is in the visible ($\lambda = 587$ nm), a mask optimized for $\psi_{\max} = 2.5\lambda$, as represented in Fig. 2.4, provides a depth-of-focus (DoFs) for an object at infinity, of $\Delta z_i = \pm 2(\psi_{\max}/\lambda)\lambda f^2/R^2 = \pm 8(\psi_{\max}/\lambda)\lambda(F\#)^2$, that is ≈ 47 μm . This value should be compared to the DoFs of a diffraction limited standard lens of the same F-number ($\Delta z_{\text{standard}} = \pm 2\lambda(F\#)^2$) of ≈ 4.7 μm , showing, as expected, a tenfold increase of the DoFs, since the DoFs of a diffraction limited standard lens corresponds to $\psi_{\max} = 0.25\lambda$ according to the Rayleigh's quarter wavelength rule. The same generic masks of Fig. 2.4 could also be used to extend the DoF of a system with longer effective focal length $f = 200$ mm and $F\# = 4$. In this case, the DoFs would be ≈ 190 μm while the DoFs of a standard lens of the same F-number is ≈ 19 μm .

For the $f = 20$ mm, $F\# = 2$ system, and a DoF extension of $\psi_{\max} = 2.5\lambda$, the radius of the mask should thus be $R = 5$ mm. A mask with such a radius can be manufactured with many different technologies, such as diamond turning or photolithography. Let us now assume that the mask in Fig. 2.4.a is used: the smallest normalized ring width is $\Delta\rho = \rho_k - \rho_{k-1} = 0.05$, which corresponds to a real width of $\Delta r = R \cdot \Delta\rho = 0.25$ mm = 250 μm . This value is a priori affordable by all the above-mentioned manufacturing methods. On the other hand, the mask of Fig. 2.4.b, which provides the same DoF extension as the one in Fig. 2.4.a, has a minimal normalized ring width of $\Delta\rho = 0.01$, which leads to an actual width of $\Delta r = 50$ μm , which is too thin for usual diamond turning but clearly affordable for photolithography or subwavelength patterning. The generic mask of Fig. 2.4.a could also be used to extend the DoF of the long focal system ($f = 200$ mm, $F\# = 4$). In this case, the real diameter of the mask would be 50mm, and some technologies, such as microlithography or subwavelength patterning, would be difficult to use at an affordable cost. On the other hand, the minimum ring width would be $\Delta r = 1.5$ mm, well within the capabilities of diamond turning.

In terms of manufacturing costs, an important consequence of the image quality leveling-off at a given number of rings is that the less complex a mask is, the cheaper it is to manufacture it. As we have shown by comparing the masks of Fig. 2.4, the fact that several local optima with similar performances are found, means that the optical

designers can choose the mask with a profile more appropriate for the manufacturing tools they have access to. In the case of the optimal phase masks we have found, for $\psi_{max} \leq 3\lambda$ and $N \leq 7$, there is always a mask with near-optimal performance having a smallest normalized ring width greater than 0.05. They thus could all be easily manufactured for the two optical systems we have taken as examples.

2.3 Frequency response of the masks and deconvolution

The modulation transfer function is one of the most used criteria in conventional optical system design, among others, such as the Strehl ratio or the spot size. In this section we will define an *effective* MTF, that considers the effects of deconvolution, and use it to study the optimized masks and their Wiener filter. We will finally assess the relevance of such and how it compares with the image quality defined in Eq. (1.31).

2.3.1 Effective MTF

A great deal of information on the effects of the optical system on the captured image are directly linked to the modulation transfer function $H(\mu, \nu)$. A typical guideline to assess the behavior of an optical system, among others, is the cutoff frequency ν_c ; the point where the MTF drops significantly so that frequencies $\nu \geq \nu_c$ will be blurred in the final image. A system is said to be *well resolved* when it satisfies the Nyquist criterion $2\nu_c < \nu_s$, where ν_s is the sampling frequency.

On a hybrid imaging system, the MTF is not enough to assess the total impact on the final image, since the post-processing is not taken into account. From Eq. (1.24), a system where a filter $d(x, y)$ is applied to the captured image has the following final image expression in the Fourier domain:

$$\text{FT}(\widehat{O}) = \tilde{d}(\mu, \nu) \cdot H(\mu, \nu) \cdot \tilde{O}(\mu, \nu) + \tilde{d}(\mu, \nu) \cdot \tilde{n}(\mu, \nu) \quad (2.2)$$

We can identify from this expression a term for the *effective* MTF

$$H_{eff}(\mu, \nu) = \tilde{d}(\mu, \nu) \cdot H(\mu, \nu), \quad (2.3)$$

and a term for the noise amplification due to filtering $\tilde{d}(\mu, \nu) \cdot \tilde{n}(\mu, \nu)$. The importance of considering the effective MTF is better exemplified in Fig. 2.8 where we show the frequency response of a system with a 5-ring BAPM optimized for a DoF of $\psi_{max} = 1.5\lambda$. The defocus value $\psi_k = 0.5\lambda$, used to calculate the MTF shown, satisfies Eq. (1.33); it is the point of the lowest IQ value for which IQ_{opt} is calculated. On top is the frequency response of the Wiener filter, on the bottom-left the MTF of the optical system (blue) and the detection noise (green) and on the bottom-right the effective MTF and the effect of deconvolution on the noise. Note that, since the pupil, the mask, and the Wiener filter are circularly symmetric, these 1-dimensional representations of the effective MTF are sufficient to understand the behavior in two dimensions.

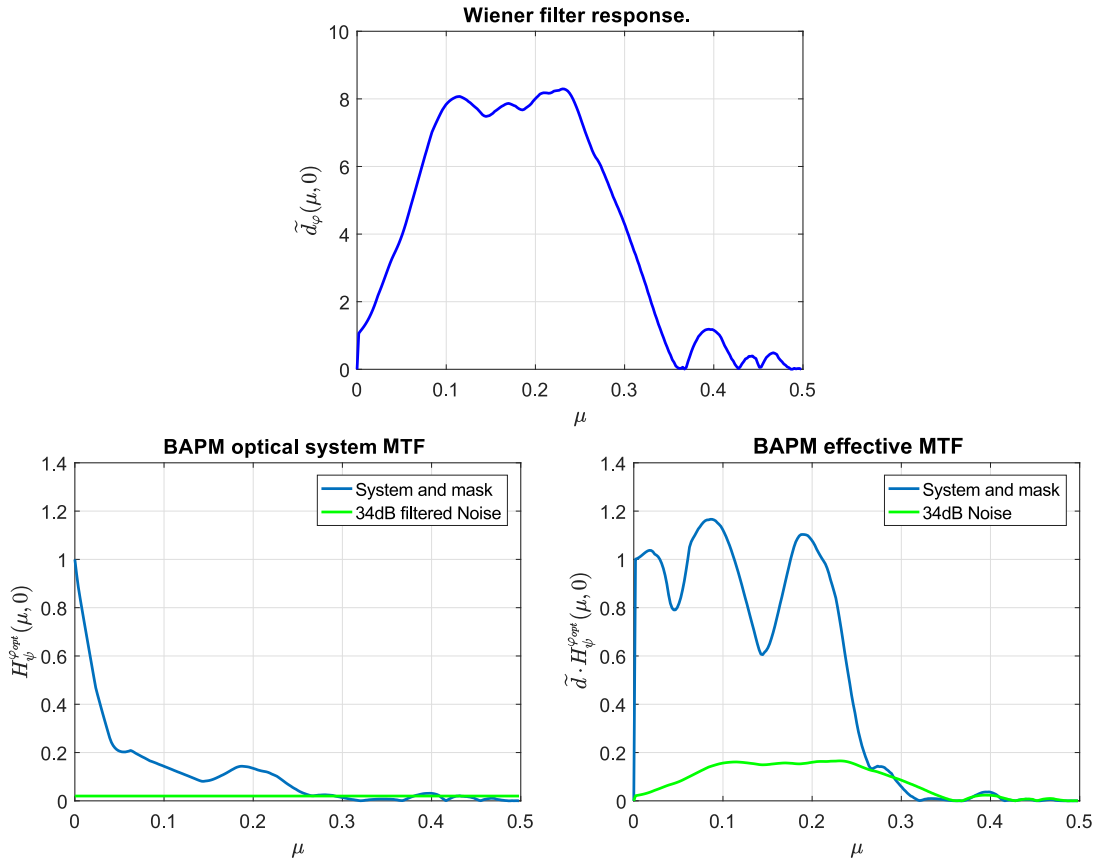


FIGURE 2.8: Effect of the Wiener filter on the optical transfer function of a 5-ring mask co-optimized for a DoF of $\psi_{\max} = 1.5\lambda$. The MTF's are shown at the defocus point $\psi_k = 0.5\lambda$, which presents the lowest value of IQ

We can see in the MTF of the BAPM that there is a rapid drop of contrast at low frequencies, and that beyond $\mu = 0.26$ the value of the MTF is below the noise level at almost every point. On the other hand, the effective MTF stays at rather high values at all frequencies lower than $\mu = 0.26$, with a just dip at $\mu = 0.16$. We see that this BAPM has a very definite cutoff frequency at $\mu = 0.26$ before and after deconvolution. Moreover, due to the noise amplification, frequencies that were originally close to the noise level cannot be recovered by means of Wiener filtering.

2.3.2 Frequency response as a function of the number of rings

It has been established in section 2.2 that co-optimized optical systems with a BAPM and a Wiener filter have an image quality that increases with the number of rings and that levels-off for a certain number of rings. We have also shown that the effective MTF from equation (2.3) can give us more information about the spatial frequency response of a hybrid imaging system than just the conventional MTF. In this section we will use the image of a butterfly shown in figure 2.9 as the scene. For the deconvolved images we use the generic Wiener filter shown in equation (1.29) using the image model $S_{OO} \propto \nu^{-2.5}$ and supposing a detection noise of 34dB.



FIGURE 2.9: Photograph of a butterfly, used as the scene for many of the signal processing examples through this work

On the left column of Fig. 2.10 we show the effective MTF of the hybrid optical system co-optimized for a DoF of $\psi_{\max} = 2.5\lambda$ with a number of rings increasing from 2 to 6. As in Fig. 2.8, the defocus values ψ_k used to calculate the H_{eff} shown satisfy Eq. (1.33) and are the point of the lowest IQ value for which IQ_{opt} is calculated. On the center column we can see the deconvolved image of the butterfly at that same value of ψ_k and on the right column we see a detail of the same image.

For the 2-ring mask, the effective MTF has a very steep drop at $\mu = 0.02$ and stays low for higher frequencies, staying below the noise level at $\mu = 0.22$. This is noticeable on the deconvolved image where only the low-frequency details are visible and the image is severely blurred. We can also notice ringing in the detail on the right. For the 3-ring mask, the effective MTF is overall better and the cutoff frequency is at $\mu = 0.32$, coinciding with the considerable increase in image quality we see from 2 to 3 rings in Fig. 2.6. On the other hand, there are considerable decreases of contrast for $\mu = 0.03$ and $\mu = 0.08$. Comparing the deconvolved images of the 2-ring and the 3-ring masks, we see that for the 3-ring mask high frequency details are more apparent; we can completely distinguish the details on the wings and the antennae are sharp, but there is some ringing around high-contrast details, such as at the edge of the wings. In the detail we see that the background is not as smooth as in Fig. 2.9. These defects are most likely due to the decreases of contrast seen at $\mu = 0.02$ and $\mu = 0.09$ (see Fig 2.10).

On the plot of the effective MTF for the 4-ring mask we see again only one reduction at low frequencies, $\mu = 0.04$, but it is not as pronounced as for the 3-ring mask. Interestingly, the cutoff frequency here is much shorter than for the 3-ring, at $\mu = 0.19$. In the deconvolved image we can see that the ringing is much less pronounced than for the previous two masks. In the the zoom-in, on the other hand, the finer details are more blurred than for the 3-ringed mask, but the background is more homogeneous. We know from Fig. 2.6 that this mask has a considerably better value of IQ_{opt} than the 3-ring mask, meaning that, for scenes with power spectra similar to $S_{OO} \propto \nu^{-2.5}$, lower frequency details contribute more to the image quality, as defined in eq. (1.31), than the higher frequency ones.

For the 5-ring mask the effective MTF has a less varying shape for frequencies below $\mu = 0.11$, and drops smoothly to its cutoff frequency at around $\mu = 0.22$, further than with 4-rings, but still shorter than for 3-rings. We can see in the deconvolved image that the ringing artifact is almost gone and that the image is overall better defined.

We see that it is sharper than for the 4-ring mask, but suffers slightly more from noise amplification in the background. Finally, for the 6-ring mask, the shape of the effective MTF is similar than for the 5-ring mask, but with slightly higher values at most points until its cutoff frequency at $\mu = 0.24$. In the deconvolved image it is difficult to see much difference with the 5-ring case; only in the zoom-in we can spot some differences, like a slight reduction in the blur, as well as some details close to the edge of the wings being more noticeable.

We have seen from this study that the effective MTF is a useful tool to analyze the behavior of a hybrid optical system. Thanks to it, we observed that the BAPM cuts down high-frequency details while the Wiener filter amplifies the contrast for low-frequencies. This low-pass filtering has been observed in all the optimized masks to a certain degree, but, as we could observe from the 3-ring mask, having a larger cutoff frequency does not guarantee higher image quality. Nevertheless, there may be cases where considering the cut-off frequency during the optimization may be advantageous, for example, to consider effects of aliasing; this will be studied in chapter 4.

Finally we can conclude that, although the effective MTF is useful to assess the performance of a hybrid imaging system, this assessment has to be based on several characteristics from the MTF and the scene, making *IQ* a much simpler, yet reliable, quantification of the performance.

2.4 Robustness of the BAPM performance

Until now, the masks and deconvolution filters were optimized by assuming a generic scene model with power-law PSD $S_{oo}(\nu) \propto \nu^{-2.5}$ and an aberration-free system. To check the robustness of our results and conclusions to these assumptions, we now evaluate the performance of the masks optimized for this model on systems that possess some amount of 3rd order aberrations, or that act on scenes whose PSDs follow a power law with different coefficients. We finally validate the masks on scenes simulated by sharp real-world photographs.

2.4.1 Sensitivity to aberrations

The binary phase masks obtained in the previous section were optimized considering an aberration-free system. If these masks were to be used in a real system, they could have to deal with a small amount of residual aberrations additionally to the defocus. Aberration correction with phase masks for DoF extension has been studied in the past. In the works of (Prasad et al., 2004) and (Tucker, Cathey, and Dowski, 1999), asymmetric masks are used to extend DoF and to correct a certain degree of spherical aberration. The study of phase masks has also been focused on the correction of aberrations, without extending the DoF, an example being (Mezouari, Muyo, and Harvey, 2006), where the authors studied the use of quartic phase masks to correct coma or astigmatism

To study the sensitivity of the mask performance to residual aberrations, we first include in our simulated optical system a known amount of aberrations with a wavefront error expressed by the following Seidel terms (Smith, 1966): $W_s = \alpha\rho^4$ for

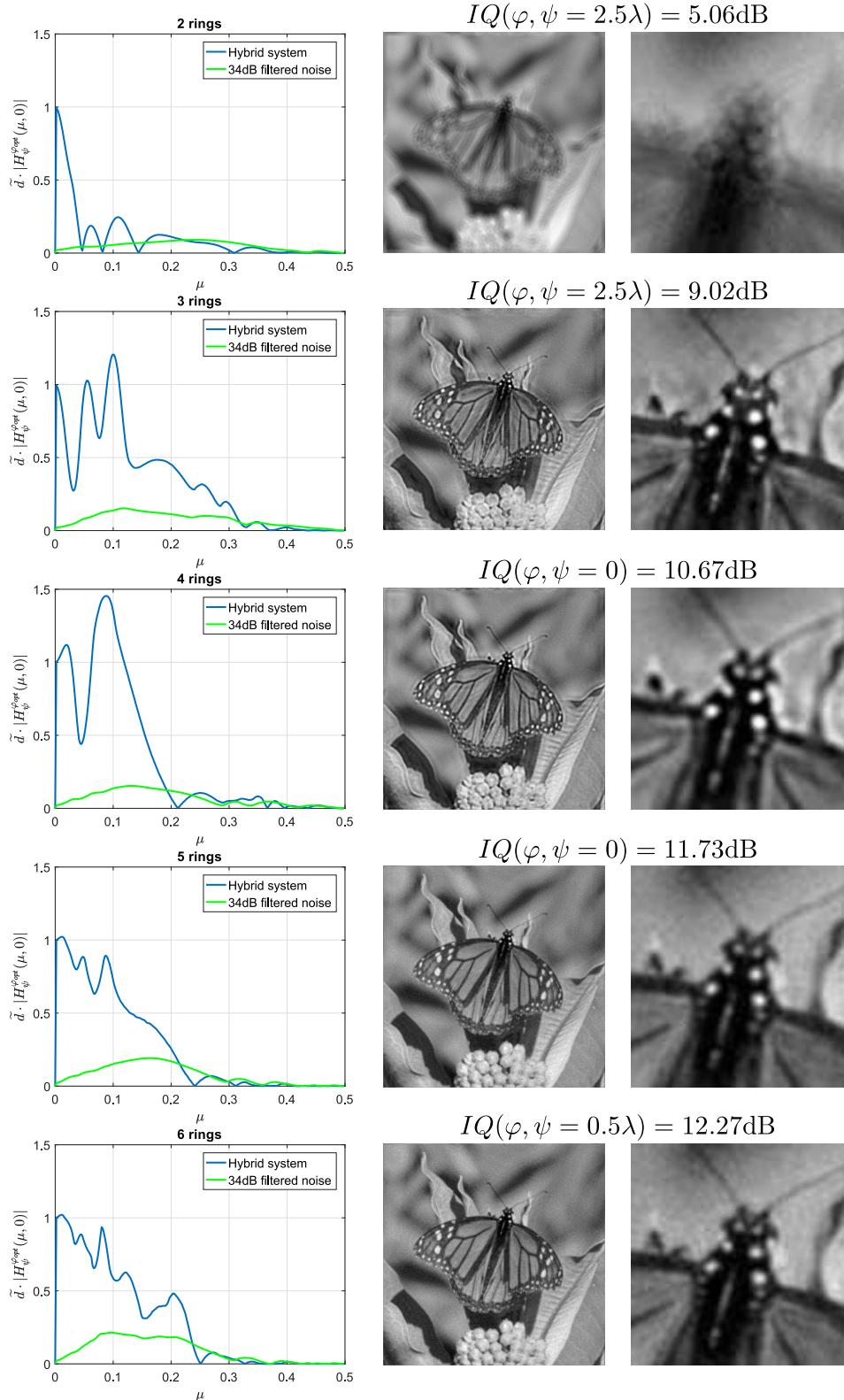


FIGURE 2.10: Comparison of the different masks optimized for $\psi_{\max} = 2.5\lambda$, shown at the defocus point ψ_k with the lowest value of IQ_{\min} , used to optimize. Effective MTF (left), deconvolved images (center), detail in the images (right)

spherical aberration, $W_c = \beta\rho^3 \cos(\theta)$ for coma and $W_a = \gamma\rho^2 \cos(2\theta)$ for astigmatism. The Seidel aberration terms are a very convenient way to decompose the wavefront error and they are commonly used to simulate aberrations.

As a reference, a conventional optical system was simulated to show the effects on $IQ(\psi, \varphi)$ of each aberration in addition to defocus. As mentioned in section 1.4.1, according to the Rayleigh's quarter wavelength rule, a peak-to-valley wavefront error due to aberration larger than $\lambda/4$ in a diffraction limited optical system is considered to be visually noticeable. The tolerable RMS error depends strongly in the application. On a non diffraction-limited system, such as professional photographic cameras, the design could allow more residual aberrations as long as the PSF spot radius is below a certain threshold. On the other hand, high-precision diffraction limited scientific equipment is usually required to have residual wavefront errors on the order of $\lambda/20$ (Suematsu et al., 2008) or even $\lambda/100$ for photolithography (Hudyma, 2000).

In Fig. 2.11.a, Fig. 2.11.c, Fig. 2.11.e and Fig. 2.11.g, the image quality is shown as a function of the DoF obtained with the 5-ring binary annular phase mask optimized for $\psi_{\max} = 2.0\lambda$ after spherical, coma, astigmatism, or a combination of the three were added to the pupil function of the optical system. Each aberration was neither taken into account when optimizing the mask, nor when calculating the averaged Wiener filter and therefore in these graphs we evaluate the sensitivity of the mask to aberrations that were not considered for their conception. On the other hand Fig. 2.11.b, Fig. 2.11.d, Fig. 2.11.f and Fig. 2.11.h show the values of the image quality as a function of the DoF on a traditional system when affected by the aforementioned aberrations. Notice that we now use the full DoF range from $-\psi_{\max}$ to $+\psi_{\max}$ in the graphs, including the negative values, since some aberrations break the symmetry of the PSF around $\psi = 0$.

We can observe in Fig. 2.11.a that for spherical aberration, the values of $IQ(\varphi, \psi)$ close to $\psi = 0$ stay very close to the aberration-free case, but as $|\psi|$ increases, the values of $IQ(\varphi, \psi)$ are reduced. We can see that for $\alpha > 0.2\lambda$, the minimum values of $IQ(\varphi, \psi)$ drop by almost 2dB, and drop by 3.3dB for $\alpha = 0.5\lambda$. Comparatively, for the classical system shown in Fig. 2.11.b, $IQ(\varphi, \psi)$ drops by 2.9dB from $\alpha = 0$ to $\alpha = 0.5\lambda$ at $\psi = 0$. We can also notice the shift of the "point of best focus" towards $-\psi$ as α grows and that, without a mask, the values of $IQ(\psi, \varphi)$ drop rapidly outside of this point; $IQ(\varphi, \psi) = 6.6\text{dB}$ for $\psi = 2\lambda$ and $\alpha = 0.5\lambda$, whereas with the 5-ring BAPM, $IQ(\varphi, \psi) = 10.6\text{dB}$ for the same defocus and spherical aberration. This shows that the systems optimized solely for DoF correction are somewhat sensitive to small spherical aberrations while still extending the DoF considerably. The drop in image quality is comparable to conventional systems at the focal point $\psi = 0$.

For coma, we can see in Fig. 2.11.c that when passing from $\beta = 0$ to $\beta = 0.5\lambda$, $IQ(\varphi, \psi)$ has a drop of less than 1dB between $\psi = -1\lambda$ and $\psi = 1\lambda$ but drops by 2.9dB outside of this range. In comparison, in Fig. 2.11.d, the drop is 4.2dB for the conventional system at $\psi = 0$, reaching an $IQ(\varphi, \psi)$ below that of the system with a phase mask. This comparison shows that the system with the binary phase mask is more robust to coma aberration than a conventional system, even if the mask optimization did not take it into account.

For astigmatism, shown in Fig. 2.11.e and Fig. 2.11.f, we can see that the drop in $IQ(\varphi, \psi)$ is 3.6dB for the system with a binary phase mask and 4.0dB for the conventional system. The behavior is, similarly to coma, more stable between $\psi = -1\lambda$ and

$\psi = 1\lambda$ and varies more dramatically beyond this range.

Finally, for the combined effects of the aberrations in Fig. 2.11.g and Fig. 2.11.h, we can see a maximum drop of $IQ(\psi, \varphi)$ of 2.7dB for the system with a binary mask and deconvolution and of 2.7dB for the conventional system at $\psi = 0$. We can see the effects of spherical aberration on the values of $IQ(\psi, \varphi)$, for the system with a phase mask, from the strong dissymmetry in the range $1 < |\psi| < 2$, that occurs similar to what we observe in (Fig. 2.11.a). On the other hand, the conventional system has a more pronounced drop of $IQ(\psi, \varphi)$ at the “point of best focus” than in the case with only spherical aberration, meaning that it is also affected strongly by the other two aberrations.

From this analysis, we can conclude that systems with binary annular phase masks are robust to residual aberrations. The corresponding performance loss is then comparable to conventional systems affected by similar residual aberrations.

2.4.2 Robustness to scene model

To evaluate the robustness of the optimized masks and filters to different scenes, let us consider the minimal value of image quality obtained with the masks optimized for $S_{oo}(\nu) \propto \nu^{-2.5}$ on a scene having another PSD. This image quality will be defined as:

$$IQ_{\min} = \min_k \left[IQ(\varphi_{\text{opt}}^{2.5}, \psi_k) \right]. \quad (2.4)$$

where $\varphi_{\text{opt}}^{2.5}$ defines the optimal mask for $S_{oo}(\nu) \propto \nu^{-2.5}$. It has to be noted that IQ_{\min} is computed using the averaged Wiener filter based on the nominal PSD $S_{oo}(\nu) \propto \nu^{-2.5}$, which is different from the PSD of the scene that is observed.

2.4.2.1 Simulated scenes

We have plotted in Fig. 2.12.a the value of IQ_{\min} obtained with a generic image with PSD $S_{oo}(\nu) \propto \nu^{-2}$, for different values of ψ_{\max} , as a function of the number of rings. Since this PSD has a more high-frequency content, the images have fine details that are difficult to recover with the generic Wiener filter, and we indeed observe that the values of IQ_{\min} are globally smaller than those of IQ_{opt} obtained in Fig. 2.6. However, the global behavior of IQ_{\min} is similar: it grows with the number of rings until, at a certain amount of rings, it levels off and has a much slower growth, additionally, in the cases of $\psi_{\max} = \{2, 2.5, 3\}\lambda$, it levels off for a larger number of rings than in Fig. 2.6.

On the other hand, we have represented in Fig. 2.12.b the value of IQ_{\min} obtained with a generic image with PSD $S_{oo}(\nu) \propto \nu^{-3}$. Since the PSD now has less high-frequency content, the images are easier to deconvolve and we indeed observe that the values of IQ_{\min} are globally larger than in Fig 2.6. The value of IQ_{\min} still grows with the number of rings until it levels off, but it saturates for smaller number of rings than in Fig. 2.6 and Fig. 2.12.a. It is to be noted that the slight decrease of image quality with the number of rings observed in some curves (for example, for $\psi_{\max} = 1\lambda$) is due to the fact that the deconvolution filter, based on the nominal PSD, is not perfectly adapted to the actual PSD of the scene. We can conclude from these simulations that as the high-frequency content of the image increases, the overall

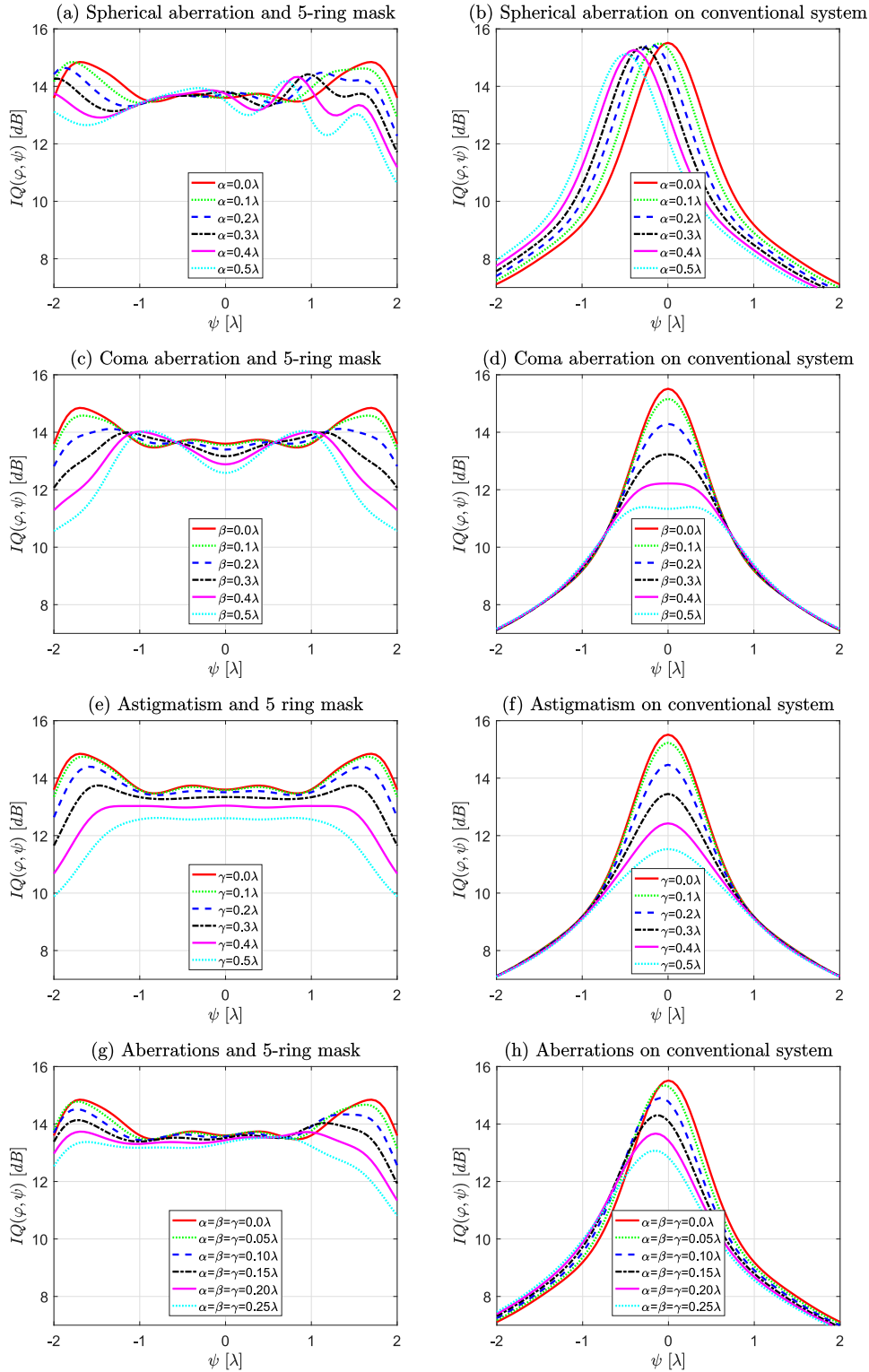


FIGURE 2.11: Comparison of a hybrid system with a 5-ring binary annular phase mask optimized for $\psi_{\max} = 2.0\lambda$ and a conventional systems with the addition of: a)-b) spherical aberration corresponding to $\alpha = \{0, 0.1, \dots, 0.5\}\lambda$; c)-d) coma corresponding to $\beta = \{0, 0.1, \dots, 0.5\}\lambda$; e)-f) astigmatism corresponding to $\gamma = \{0, 0.1, \dots, 0.5\}\lambda$; g)-h) aberrations such that $\alpha = \beta = \gamma = \{0, 0.05, \dots, 0.25\}\lambda$

hybrid imaging performance decreases and more rings are needed to saturate the performance.

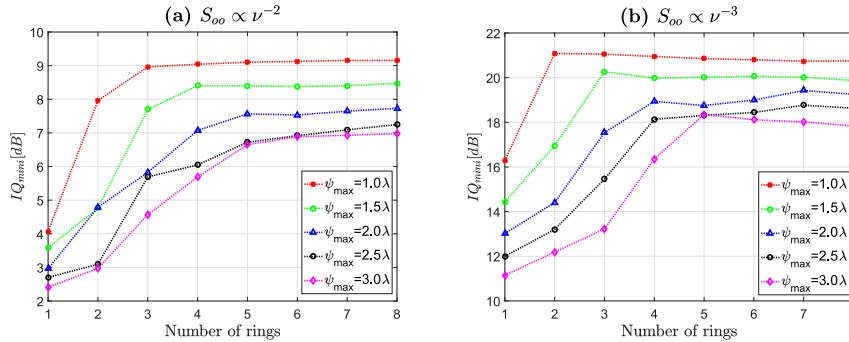


FIGURE 2.12: Performance comparison of optimal annular phase masks obtained for the model $S_{oo}(\nu) \propto \nu^{-2.5}$ and applied to scenes following the model (a) $S_{oo}(\nu) \propto \nu^{-2}$ and (b) $S_{oo}(\nu) \propto \nu^{-3}$.

2.4.2.2 Real scenes

Let us now consider the performance of the optimized masks on real-world scenes. Fig. 2.13.a (referred to in the following as “Lena”) has a small high-frequency content, and we have checked that its PSD $S_{oo}(\nu)$ falls between $\nu^{-2.5}$ and ν^{-3} . On the other hand, Fig. 2.13.b (referred to in the following as “Sea”), contains more high spatial frequency details and we have checked that its PSD falls between $\nu^{-2.5}$ and ν^{-2} . In both cases, the scene has the same resolution as the detector, 512x512 pixels, since we are considering a diffraction limited system and therefore, effects of sampling such as aliasing are not present.



FIGURE 2.13: Natural images used as scenes to test the performance of the hybrid imaging system

In Figs. 2.14.a and 2.14.c, we have represented the values of IQ_{\min} obtained on Lena and on Sea respectively. The conclusions are similar to those drawn from Fig. 2.12, showing that the scene PSD is indeed the main factor influencing the final imaging performance of the hybrid system. On Fig. 2.14.b and Fig. 2.14.d, we have represented the values of IQ_{opt} obtained on Lena (b) and Sea (d) with masks optimized for the PSD model best adapted to each scene, that is, $S_{oo}(\nu) \propto |\tilde{O}(\nu)|^2$, the square modulus of the Fourier transform of the scene. By comparing Fig. 2.14.b with Fig. 2.14.a,

we can see that the behavior of the curves and the obtained values of IQ_{opt} , obtained with the optimal masks, are very close to the values of IQ_{min} obtained with mask optimized with $S_{oo}(\nu) \propto \nu^{-2.5}$. The same conclusion can be drawn from the Sea image (Fig. 2.14.d and Fig. 2.14.c). This shows that the optimization of the masks is robust to the chosen PSD model of the scene.

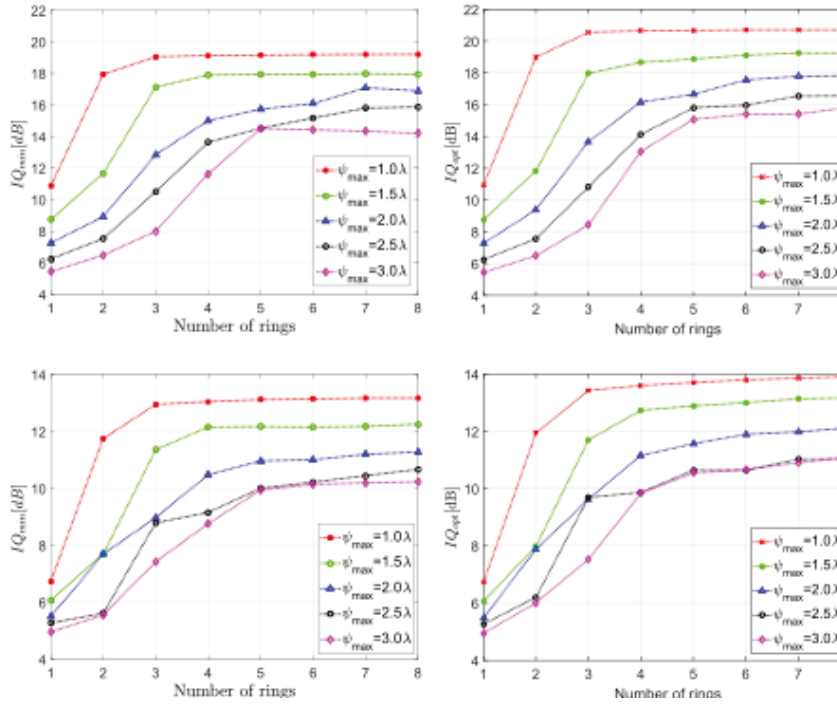


FIGURE 2.14: Variation of IQ_{min} and IQ_{opt} for different values of ψ_{max} and different numbers of rings, using two different scenes: Lena (a and b) and Sea (c and d). The masks are optimized using the model PSD $S_{oo}(\nu) \propto \nu^{-2.5}$ (a and c respectively) and using the PSD of the scenes themselves where $S_{oo}(\nu) \propto |\tilde{O}(\nu)|^2$ (b and d).

2.4.3 Visual performance comparison

Let us now visually assess the performance of the hybrid imaging systems based on the optimized masks on images perturbed with a simulated defocus blur. For simplicity, the deconvolutions are performed in the Fourier domain directly using Eq. (1.29) with no truncation of the deconvolution filter. We have displayed in Fig. 2.15.a the simulated image of Lena that would be obtained by a well-focused diffraction limited optical system followed by deconvolution with a Wiener filter adapted to the observed scene. This "best possible image" will be our reference. In Fig. 2.15.b, we have represented a simulated image of the same scene that would be obtained with an imaging system defocused of $\psi = \psi_{\text{max}} = 2.0\lambda$ followed by deconvolution with an averaged Wiener filter as defined in Eq. (1.29). We can see that for this level of defocus the image is strongly blurred.

In Fig. 2.16 are displayed the simulated images obtained with a hybrid imaging system with masks optimized at $\psi_{\text{max}} = 2.0\lambda$ and composed of 3 to 8 rings and zoom-ins of the brim of the hat, its feathers and the eye of Lena so we can better appreciate



FIGURE 2.15: Images produced by a diffraction limited system with $SNR = 34dB$ after deconvolution at (a) $\psi = 0\lambda$ and (b) $\psi = 2.0\lambda$.

the differences. These masks have been optimized with the generic power-law PSD model $S_{oo}(\nu) \propto \nu^{-2.5}$ and not the PSD of the scene, $S_{oo}(\nu) \propto |\tilde{O}(\nu)|^2$. The averaged Wiener filter used for deconvolution is also based on the generic power-law PSD. For all the deconvolved images in Fig. 2.16 we reach the goal of having a better sharpness and image quality than for the maskless system in Fig. 2.15.b. Of course, the sharpness is inferior to that obtained in Fig. 2.15.a, as the phase mask alters the optical transfer function of the system to extend the DoF. We note that the quality of the deconvolved images increases with the number of rings; with the 3-ring mask, all the features of the scene can be identified, but there is an important loss of sharpness, as well as ringing artifacts around high spatial frequency details, like the brim of the hat or the feathers. With the 4-ring mask, the ringing is greatly reduced, but there is a slight increase in blur as can be seen on feathers.

With the 5-ring mask the sharpness is increased and ringing is reduced even more; we can now identify finer feathers on the hat. With the 6-ring mask, there is a very slight increase in visual quality, mostly in contrast: this is consistent with the shape of the curve corresponding to $\psi_{\max} = 2$ in Fig. 2.14.a. The image obtained with a 7-ring mask corresponds to a more significant sharpness improvement, which is again consistent with the increase of IQ_{\min} observed in Fig. 2.14.a. Finally, passing from 7 to 8 rings decreases IQ_{\min} by 0.1dB. This somehow counter-intuitive result, also observed in Fig. 2.14.a, is due to the fact that the masks were optimized for a generic PSD model and not for the PSD of the scene. Indeed, this drop disappears in Fig. 2.14.b.



FIGURE 2.16: Image and zoom-ins of Lena obtained for defocus $\psi = \psi_{\max}$ with the simulated hybrid imaging system with masks optimized for $\psi_{\max} = 2.0\lambda$ and different numbers of rings.

2.5 Conclusions

In this chapter we have studied thoroughly the binary annular phase masks for depth of field extension, from the way we co-design them to their robustness to variations of the scene and optical system. Phase mask co-optimization is complicated for the BAPM since the optimization landscape is highly nonconvex and plagued with local maxima. Some of these local maxima have the interesting property of having very similar IQ values while having vastly different shapes, which can provide different choices when manufacturing.

Binary annular phase masks require more rings to reach higher DoF, but the best possible image quality decreases as the required DoF range increases, so that the DoF extension reachable with binary phase masks is bounded. Moreover, for a given value of the required DoF, there is a point where augmenting the amount of rings

does not improve the performance anymore, indicating that a limited number of rings is enough to obtain the best possible performance. The optimal masks with number of rings past the leveling point just add thin rings close to the border of the mask compared to the mask at the leveling point, showing that there is a common optimal pattern for a given optimization problem. These results are important for mask manufacturing, since the number and thickness of the rings reachable by technology may be limited given a numerical aperture and a target DoF.

The visual quality of the images, as a function of the number of rings, is shown to be consistent with the value of the image quality criterion used to optimize the masks. This is true even if the scene different than the generic model used for optimization or with the presence of aberrations, showing that our conclusions for the BAPM are robust even beyond our assumptions for optimizations. We have also defined an effective MTF that takes into account the deconvolution step. We have shown that BAPMs have a low-pass filtering effect and that the Wiener filter amplifies those frequencies. Moreover, we can relate the shape of the effective MTF to visual characteristics of the deconvolved images, making it an useful tool to analyze the performance of the optical system.

Other assumptions, such as monochromatic light or the diffraction limited system were not contested by studying broadband wavelengths nor aliasing effects. The broadband case is usually not considered for simulations, but it has been shown (Diaz, 2011) that it does not reduce dramatically the performance of the mask since the optical path differences caused by the mask at different wavelengths are similar. The sampling considerations will be introduced in chapter 4 where we will assess the feasibility of using phase masks for DoF extension in conjunction with super-resolution techniques.

In the next chapter we will use the tools developed this far to study continuous-profile phase masks, such as the QPM and the CPM introduced previously, as well as other masks with a free-form continuous phase. We will also compare their performance, using the BAPM as a baseline.

Chapter 3

Optimization and evaluation of different mask shapes

In chapter 2 we made an in-depth analysis of the performance of a specific hybrid imaging system for depth of field extension using a binary annular phase mask. We optimized these phase masks using the image quality criterion IQ_{\min} , defined in chapter 1. In that same chapter, we briefly showed that this quality criterion could be used to calculate the optimal profile of a cubic phase mask for DoF extension.

The tools used to optimize and to analyze the performance and robustness of BAPMs can be applied to masks with any profile, such as masks with continuous-phase profiles, which makes it possible to compare them on a quantitative basis. In this chapter we first demonstrate the superiority of the criterion IQ_{\min} defined in chapter 1 against another commonly used criterion, the Strehl ratio in the case of co-optimized hybrid optical systems. The rest of the chapter is dedicated to the use of this co-design criterion for the optimization and analysis of the performance of three generic types of continuous-phase masks in terms of their image quality, their MTF and visual inspection. We compare these results among the masks themselves and to the BAPMs we obtained in previous chapters.

3.1 Importance of the performance criterion

As we have established in chapters 1 and 2, the design of phase masks for DoF extension requires a careful choice of the optimization criterion. We have used the theoretical framework in the work of (Diaz et al., 2011) to show that the invariability of the MTF as a function of the defocus parameter ψ is not an ideal criterion to use with a hybrid optical system consisting of a phase mask and a digital deconvolution. We indeed show that the criterion must be able to take into account the deconvolution step, reason why we use the image quality IQ performance criterion.

In this section our priority is to perform a deeper analysis of the implications of choosing one performance criterion or another. We first introduce another criterion frequently used to evaluate the quality of imaging systems, the Strehl ratio. We then consider different types of systems, including a binary annular phase mask (BAPM), a quartic phase mask (QPM) and a cubic phase mask (CPM). We determine, for these systems, the masks that optimizes the Strehl ratio and the IQ_{\min} criterion. This enables us to draw conclusions about the relative merits of each criterion

3.1.1 The Strehl ratio

3.1.1.1 Definition of the Strehl ratio

The Strehl ratio is a metric commonly used in optical system design as a mean to evaluate the performance of the system when balancing aberrations (Maréchal, 1947). It is defined as the ratio between the maximum irradiance point of the aberrated PSF of an optical system and the maximum unaberrated (diffraction limited) PSF but it provides a fair prediction of an optical system's performance. The Strehl ratio is not, by any means, the only performance metric used by optical designers. In our hybrid system, this equates to compare the point of maximum irradiance of the PSF h_ψ^φ generated by a system with a phase mask $\varphi(x_P, y_P)$ at a defocus of value ψ with the on-axis value of the PSF of a focused maskless system, $h_0(0, 0)$, in other words:

$$\text{SR} = \frac{\max_{x,y} [h_\psi^\varphi(x, y)]}{h_0(0, 0)}. \quad (3.1)$$

The point of maximum irradiance of the PSF of a system with a circularly symmetric phase mask and no defocus is always on-axis. As mentioned briefly in chapter 1, this is not true for asymmetric masks, such as the cubic phase mask. For this reason, we cannot directly use other, simpler, definitions of the SR, such as using the on axis value of the aberrated PSF (Maréchal, 1947) instead of its maximum, or the statistical derivation found by (Mahajan, 1982).

3.1.1.2 Strehl ratio as a performance criterion

The interest of using the Strehl ratio in optical design is that it provides information on the proportion of the light from a point-source on the scene that is projected into a point - a pixel - on the detector and it is considered to be suitable for a conventional aberrated system when $\text{SR} > 0.8$ (Maréchal, 1947). In this section we will study its pertinence in co-design of phase masks for DoF extension.

The idea of using SR as a performance criterion for DoF extension has been used in several works (Mezouari and Harvey, 2002), in particular, we will use the approach of (Hu et al., 2013), where they use the convention of $\text{SR} > 0.8$ to define the effective DoF of the mask. As we will see later this approach exemplifies one of the limitations of the Strehl ratio as a performance criterion in co-design.

To study the behavior of the Strehl ratio we will consider a DoF of $\psi \in [-1.5, 1.5]\lambda$, a 34dB detection noise and a PSD model $S_{OO} \propto \nu^{-2.5}$ for the scene. For the analysis we will use two different quartic phase masks (QPM) of profile $\varphi(r) = \alpha_4 r^4 - \alpha_2 r^2$: the first one, named QPM_{SR}, and was analytically calculated in (Hu et al., 2013) so that the SR is symmetric around $\psi = 0$, and has parameters $\alpha_2 = \alpha_4 = 2.36\lambda$. The second mask, QPM_{opt} was optimized using the IQ_{\min} criterion and has parameters $\alpha_4 = 2.60\lambda, \alpha_2 = 2.29\lambda$. We also use the two cubic phase masks (QPM) of profile $\psi(x, y) = \alpha(x^3 + y^3)$ that were shown in chapter 1 section 1.4.1, one of them, CPM_{inv} is the mask with $\alpha = 10\lambda$ calculated to have an invariant PSF and the other mask, CPM_{opt}, is the optimized one with $\alpha = 1.96\lambda$. Finally, we use the 5-ring binary

annular phase mask optimized on 2 for $\psi_{\max} = 1.5\lambda$. On figure 3.1 we show the comparison of the SR between the five masks and compare it with the maskless system.

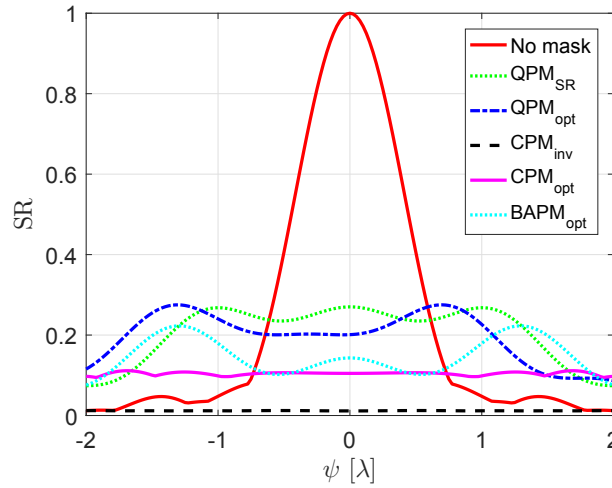


FIGURE 3.1: Comparison of the SR as a function of the defocus parameter ψ of: a conventional system (red), a QPM calculated to maximize the SR (green) on $|\psi| < 1.5\lambda$, an optimized QPM for the same range (blue), a CPM calculated for invariant defocus (violet) and an optimized BAPM for the same range.

At first glance, we can see that the conventional optical system has value of SR higher than any of the masks on the range $|\psi| < 0.65\lambda$, but, as we have seen in chapter 2, BAPMs have a superior performance beyond the limits of the Rayleigh criterion of $|\psi| > 0.25\lambda$. We can see that, the masks with the highest SR are both QPM, with a slight advantage for the optimized one if we consider the total DoF. On the other hand, the cubic phase masks have the lowest SR, particularly CPM_{inv} , which has a much more spread PSF. The 5-ring BAPM sits in the middle, having sections as low as the optimized CPM and others almost as high as the QPM_{SR} .

Continuing the analysis of Fig.3.1, we see that all the masks shown have a symmetric SR around $\psi = 0$, with the exception of the optimized QPM_{opt} , whose symmetry is shifted by -0.25λ , so that its effective DoF is $\psi \in [-1.75, 1.25]\lambda$; this coincides with the shift that spherical aberration causes on conventional systems. As we will see in the following, SR symmetries do not necessarily equate to symmetric image quality.

3.1.2 Comparison of SR-based and MSE-based performance criteria

3.1.2.1 Image quality as a function of the defocus

As established on chapter 2, the use of the image quality, $IQ(\varphi, \psi)$ as a performance criterion gives a good insight on the expected deconvoluted image. On figure 3.2 we show the comparison of the $IQ(\varphi, \psi)$ as a function of ψ for the different masks we have presented in section 3.1.1.2. The Wiener filters for deconvolution were calculated for the range $\psi \in [-1.5, 1.5]\lambda$. In particular, for the maskless system, the deconvolution is performed with a Wiener filter calculated with the averaged defocused PSFs.

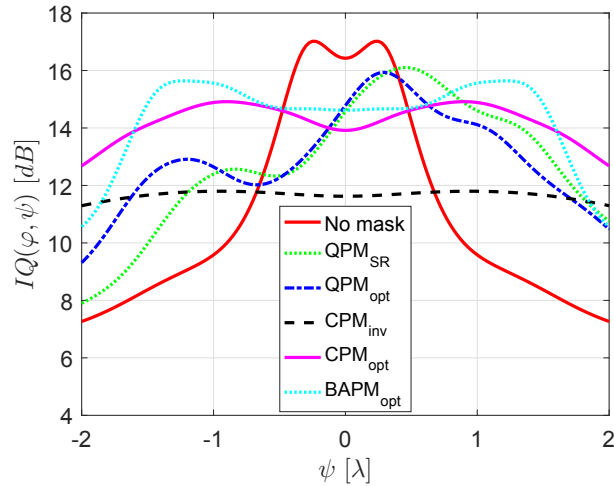


FIGURE 3.2: Performance comparison as a function of the defocus parameter ψ of: a conventional system (red), a QPM calculated to maximize SR (green) on $|\psi| < 1.5\lambda$, a QPM optimized for the IQ_{\min} criterion on the same DoF range (blue), a CPM calculated for invariance to defocus (black), a CPM optimized for the IQ_{\min} criterion (violet), and a BAPM optimized for the IQ_{\min} criterion.

As we can see, although all masks had a symmetric SR, the IQ of the deconvolved images from the QPMs is not; there is a steep decline for defocus values $\psi < 0$. Even more, on the positive side of the DoF the optimal CPM and BAPM have IQ values comparable to the QPM, with the extra perk of having a DoF which is twice as large. On figure we show the PSF of the QPM_{SR} at two symmetric defocus points: $\psi = -1.0\lambda$ and $\psi = 1.0\lambda$. We can see that although the maximum value of the PSF is identical, and so is the Strehl ratio, the point spread functions are vastly different and, since we are using a single deconvolution filter, the qualities of the deconvolved images are not the same.

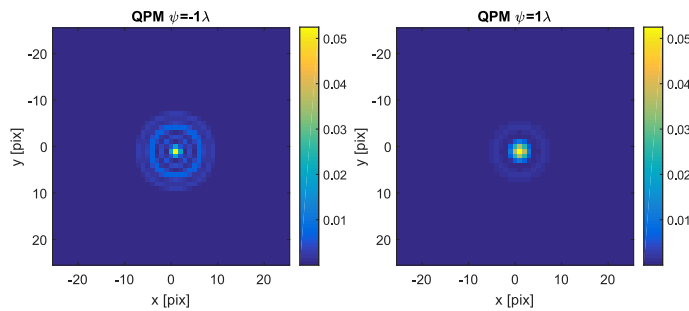


FIGURE 3.3: Point spread function of a system with the QPM_{SR} at the defocus points $\psi = -1.0\lambda$ and $\psi = 1.0\lambda$

This result shows how SR as a performance criterion for hybrid systems fails to give insight on the final image quality and why it is necessary that the criterion we chose considers the deconvolution step. Additionally, we have shown that the CPM is outperformed by other masks, such as the QPM and the BAPM, in DoF extension

problems involving only defocus aberration correction. This result is not a discouragement for using QPM for DoF, these masks have the property of compensating for other first order aberrations, such as spherical aberration, as we can see in (Mezouari and Harvey, 2002), (Mezouari, Muyo, and Harvey, 2006).

3.1.2.2 Mean and minimum image quality criteria

In chapter 1 we have defined two different performance criteria for optimization: the mean image quality, IQ_{mean} and the minimum image quality IQ_{min} . We explained our reasoning to use IQ_{min} for the optimizations in chapter 2, explaining that optimizing IQ_{mean} will always reach a performance that is, at best, the same as for IQ_{min} . In this section we further the discussion, using the quartic, cubic and binary annular phase masks to illustrate these decisions.

In figure 3.4 are plotted the values of the IQ_{mean} and IQ_{min} parameters calculated for a DoF range of $\psi \in [-1.5, 1.5]\lambda$. As we can see, the BAPM optimized for this range has the highest performance in both IQ_{min} and IQ_{mean} , being $\approx 0.5\text{dB}$ higher than the CPM_{opt} on each metric. The case of the QPMs is interesting, since their IQ_{mean} values are practically the same, the optimization algorithm could end up in either local maxima. On the other hand, their values of IQ_{min} are almost 2dB apart, making the QPM_{opt} a better mask. This result highlights why once we chose our performance metric, such as the image quality IQ , the way of evaluating it can affect the results we obtain from optimization.

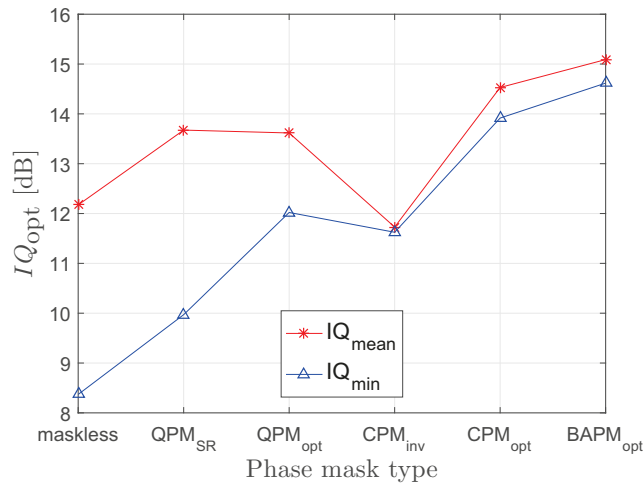


FIGURE 3.4: Comparison of the IQ_{mean} and IQ_{min} performance criteria for: a conventional system (red), a QPM calculated to maximize the SR (green) on $|\psi| < 1.5\lambda$, an optimized QPM for the same range (blue), a CPM calculated for invariant defocus (violet) and an optimized BAPM for the same range.

3.1.3 Visual inspection

The results obtained in section 3.1.2 show that the Strehl ratio is not an ideal performance criterion for DoF extension, but only shows this in the context of IQ evaluation. This analysis is incomplete without a visual inspection of real images, since it could be that IQ is not successfully representing the visual performance of the system. In figure 3.5 we have compared the effects of each hybrid system on the image of the butterfly from Fig. 2.9 at the defocus distances $\psi = \{-1.5, 0, 1.5\}\lambda$.

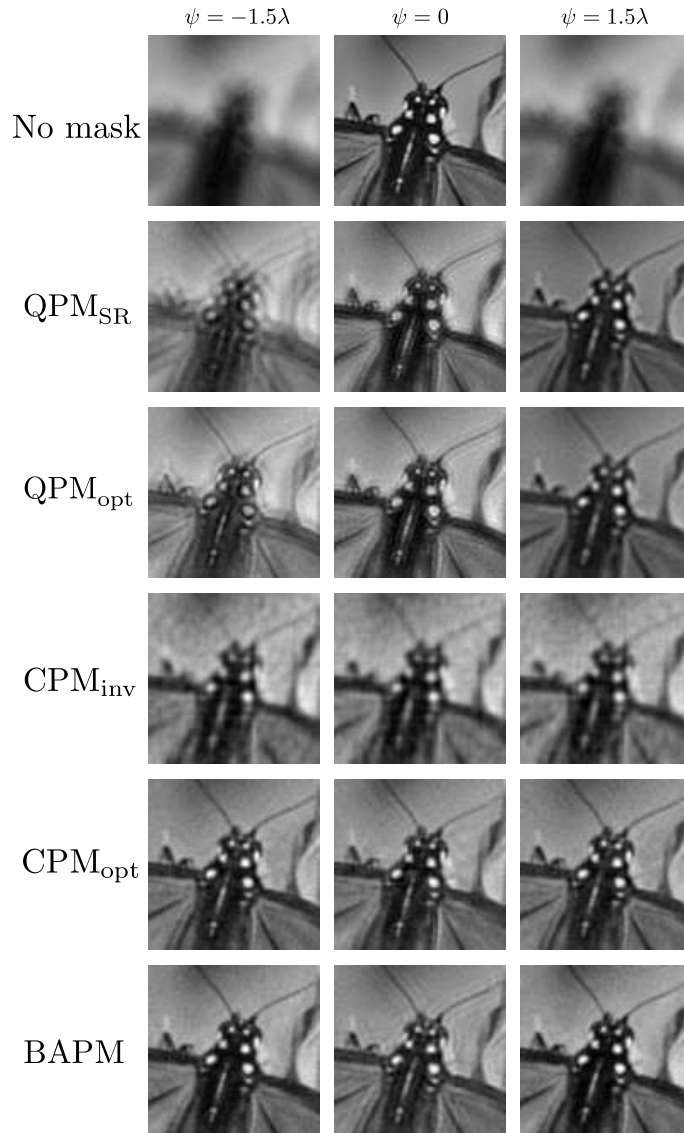


FIGURE 3.5: Comparison of the image at $\psi = \{-1.5, 0, 1.5\}\lambda$ produced by systems with, from top to bottom: No mask, a quartic phase mask

We can see that QPM_{SR} has a rather sharp image at $\psi = 1.5\lambda$, it presents some ringing at $\psi = 0$ and is blurred for $\psi = -1.5\lambda$, showing a strong dissymmetry, as with the $IQ(\varphi, \psi)$, despite the symmetrical SR. We see a similar effect for the optimized QPM_{opt} , but the artifacts on the negative ψ are weaker, since this mask was optimized for the full DoF. For both CPMs and the BAPM we have the results

we have already seen in chapters 1 and 2, although it is worth mentioning that the images generated by both QPMs are much sharper at $\psi = 1.5\lambda$ than for all the other masks. Additionally CPM_{inv} has a very strong noise amplification, and its visual quality could be considered worse than for the QPM_{opt} at $\psi = 1.5\lambda$. This coincides with the values of $IQ(\varphi, \psi = 1.5\lambda)$ shown on figure 3.2, where the image quality of the system with the CPM_{opt} is higher than for QPM_{SR} but lower than for QPM_{opt} .

The results from this section show the relevance, not only of the performance criterion chosen, such as SR or IQ , but also that in a problem such as DoF extension the way these criteria are evaluated and optimized is of critical importance to achieve the desired visual performance. We have pointed out several problems that come with using SR as a performance criterion in the context of co-design of phase masks for DoF extension, such as possible symmetries that do not reflect the actual imaging performance of these hybrid systems.

We have found that IQ is a strong metric that mirrors the actual visual image quality obtainable by a given system, but also that having a strong metric requires also to choose the right way to evaluate it during optimization. By the results shown in this chapter, plus many others leading to the optimal masks studied in chapter 2, we have reached the conclusion that IQ_{min} works consistently better than aiming for invariability of the PSF or optimizing the averaged IQ_{mean} .

3.2 Continuous phase masks for depth of field extension

In the previous section we have established the importance of the performance evaluation tools in the co-design process; now we will use these tools to study the relation between profile shapes and the capacity of extending the depth of field. This is done by making use of continuous phase masks, which have been extensively used in the literature to provide analytical solutions to DoF extension problems, as Dowski and Cathey did with the cubic mask (Dowski and Cathey, 1995), or as Mezouari et al. did with quartic phase masks for the mitigation of third order aberrations (Mezouari, Muyo, and Harvey, 2006).

In these works, a specific mask shape was analytically obtained in order to turn the PSF invariant to defocus or aberrations. The mask profiles proposed by them were exceptionally simple, with only one parameter to calculate since the analytical solution of a multi-parameter problem can be challenging or even impossible to obtain. In this section, we generalize the continuous phase mask profile shapes to include more terms. This is possible due to the co-optimization approach we use to obtain the mask shapes, allowing us to go beyond the limits of analytical solutions.

Continuous-phase masks encompass any mask whose profile is derivable at all points and has no occlusions within the pupil radius. This definition being very broad, we focus mainly on three kinds: masks with asymmetric polynomial profiles, circularly symmetric masks whose profile is defined by a polynomial generatrix curve and circularly symmetric masks whose profile is defined by a free-form generatrix. In the following we mathematically describe these masks and discuss the results of their optimization.

Throughout this section all the optimizations are made under the same assumptions as for BAPMS: a diffraction limited system with a phase mask in the pupil, with a generic scene of PSD $S_{OO} \propto \nu^{-2.5}$ and SNR of 34dB. For each mask we performed the

optimization for only the positive values of the DoF $\psi \in [0, \psi_{\max}]$, with $\psi_{\max} = 1.5\lambda$. The deconvolution is performed by an averaged Wiener filter as defined in equation (1.29).

3.2.1 Polynomial phase masks

We use the polynomial phase masks (PPM) as defined in (Caron and Sheng, 2008) for DoF extension in microscopes. Their profile is described by:

$$\begin{aligned} \varphi(x_P, y_P) = & \alpha(x_P^3 + y_P^3) + \beta(x_P^2 y_P + x_P y_P^2) + \gamma(x_P^5 + y_P^5) \\ & + \delta(x_P^4 y_P + x_P y_P^4) + \epsilon(x_P^3 y_P^2 + x_P^2 y_P^3) + \dots, \end{aligned} \quad (3.2)$$

where the profile of the mask is fully described by the value of the coefficients $\alpha, \beta, \gamma, \delta, \epsilon, \dots$. These masks are a generalization of the cubic phase mask used by (Dowski and Cathey, 1995) shown in chapter 1 and have the characteristic of producing PSFs that are symmetric on the DoF around $\psi = 0$ but have an asymmetric PSF spot shape. As was discussed in chapter 2, when analyzing figure 2.2, the PSF of asymmetric masks, such as the PPM is off-center by a distance proportional to the value of ψ and the *strength* of the mask profile, meaning the peak-to-valley difference of the mask profile. This off-centering of the PSF will cause the final image to be off-centered as well, and has to be taken into account during the optimization in order to properly evaluate the mask performance.

3.2.1.1 PPM optimization results

For the optimization of these masks we consider cases with different combinations of the polynomial coefficients. We optimize the following configurations:

- A third degree polynomial (cubic) phase mask, ($\alpha \neq 0$) denoted PPM_{α} .
- A third degree polynomial with crossed terms ($\alpha, \beta \neq 0$), denoted $\text{PPM}_{\alpha, \beta}$.
- A fifth degree mask ($\alpha, \gamma \neq 0$), denoted $\text{PPM}_{\alpha, \gamma}$.
- A fifth degree mask with crossed terms ($\alpha, \beta, \gamma, \delta, \epsilon \neq 0$), denoted $\text{PPM}_{\alpha, \beta, \gamma, \delta, \epsilon}$.
- A seventh degree mask ($\alpha, \gamma, \eta \neq 0$), denoted $\text{PPM}_{\alpha, \gamma, \eta}$.

This collection of masks lets us not only compare masks of different degrees, but also to see the difference between choosing crossed terms or not, since they add a significant amount of optimization parameters for a given polynomial degree.

As we mentioned in section 3.2, to correctly assess the performance of the PPM, image registration must be performed on the deconvolved image before calculating $IQ(\varphi, \psi)$ in order to properly compare the scene O and the final image \hat{O} . For our optimization we evaluate the shift by minimizing the mean squared error between the PSF of the system at $\psi = 0$ and at whichever evaluation point ψ_k is being analyzed. This intermediate step in the evaluation of $IQ(\varphi, \psi)$ makes the optimization process much slower than with other masks, limiting the amount of parameters we can optimize at the same time.

The profiles of the optimal masks found are shown in Fig. 3.6. We can appreciate how all the masks have the same overall shape, typical from odd-polynomial surfaces. We can see that $\text{PPM}_{\alpha,\gamma}$ and $\text{PPM}_{\alpha,\gamma,\eta}$ masks have a mask profile peak-to-valley difference of $\Delta\varphi_{PV} \approx 5.6\lambda$ whereas the PPM_{α} , $\text{PPM}_{\alpha,\beta}$ and $\text{PPM}_{\alpha,\beta,\gamma,\delta,\epsilon}$ have strengths of $\Delta\varphi_{PV} \approx 3.8\lambda$. Finally, we can see that the $\text{PPM}_{\alpha,\beta,\gamma,\delta,\epsilon}$ has a more rounded profile in the -45 deg diagonal, compared to the other four profiles; this is because in this diagonal the crossed terms have the most influence and this is the PPM with most crossed terms we have optimized.

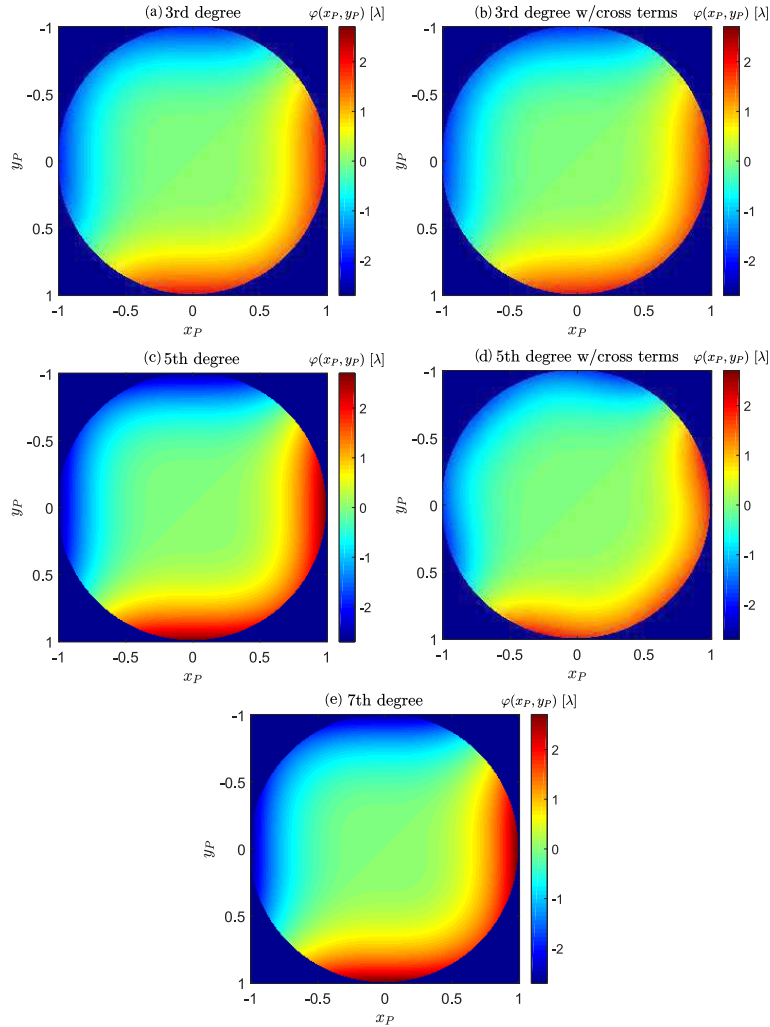


FIGURE 3.6: Comparison of PPM profiles of different degrees: a) PPM_{α} , b) $\text{PPM}_{\alpha,\beta}$, c) $\text{PPM}_{\alpha,\gamma}$, d) $\text{PPM}_{\alpha,\beta,\gamma,\delta,\epsilon}$, e) $\text{PPM}_{\alpha,\gamma,\eta}$.

3.2.1.2 PPM performance comparison

Studying BAPMs, we have found that the value of IQ_{opt} , for a given depth of field ψ_{max} , increased with the number of rings, and leveled-off at a certain amount. In the case of PPMs, the number and the value of each parameter modify the profile in a more complex way. In figure 3.7 we compare the performance of the five optimized PPM as a function of the defocus parameter ψ . We have increased the ψ axis by 0.5λ around the DoF range considered for optimization so we can appreciate the behavior

of the performance at the edges of this DoF range. If we analyze the behavior of the two 3rd degree PPMs, PPM_α and $PPM_{\alpha,\beta}$, they follow very similar trajectories, with a marginally better IQ_{opt} for $PPM_{\alpha,\beta}$, at $\psi = 1.5\lambda$. The same can be said for the $PPM_{\alpha,\gamma}$ and $PPM_{\alpha,\gamma,\eta}$, the 5th and 7th degree masks, with the difference that their performance is considerably better than for the 3rd degree masks around $\psi = 0$.

Finally we have the 5th degree with crossed terms mask, $PPM_{\alpha,\beta,\gamma,\delta,\epsilon}$ which performs overall better than all the other optimized PPMs. The image quality behavior is similar to $PPM_{\alpha,\gamma}$ and $PPM_{\alpha,\gamma,\eta}$, but with $IQ(\varphi, \psi)$ being $\approx 0.5\text{dB}$ higher at all points. The 5th and 7th degree masks have a very stable performance up until $\psi = 1\lambda$, where it starts decreasing steadily.

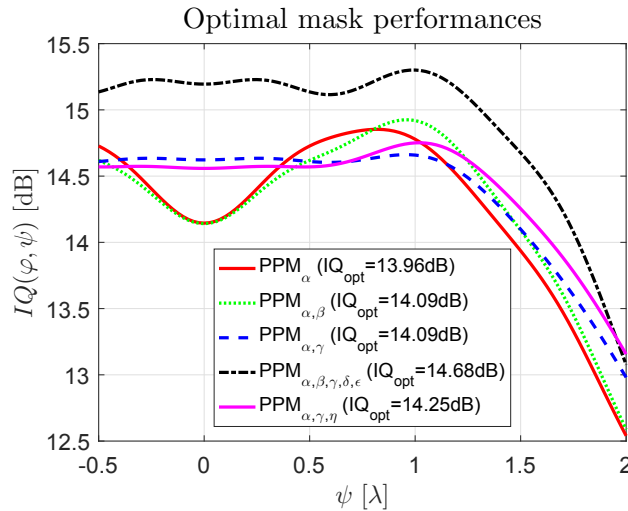


FIGURE 3.7: Comparison of the performance of hybrid systems with PPMs of 3rd, 5th and 7th degree polynomial profiles, for 3th and 5th degree polynomials, the crossed terms are also included.

It is worth noticing that, as for BAPMs, the PPMs have a total DoF of $|2\psi_{max}|$, reason why there is no decay on $IQ(\varphi, \psi)$ below $\psi = 0$, as we will see with the circularly symmetric continuous masks.

3.2.2 Aspheric phase masks

Aspheric phase masks (APM) have a phase profile defined by a rotationally symmetric polynomial (in other words, a surface of revolution where the generatrix curve is a polynomial), their phase profile can be defined as:

$$\varphi(\rho) = \sum_{i=1}^N \alpha_i \rho^i, \quad (3.3)$$

where N is the polynomial degree. In this case, the mask is defined by the parameters α_i . For an N^{th} degree polynomial, there will be N optimization parameters: we have fixed $\alpha_0 = 0$, since adding a constant phase has no effect on the wavefront. These masks are a generalization of the quartic phase mask of profile $\varphi_{QPM}(\rho) = \alpha_4 \rho^4 - \alpha_2 \rho^2$, which was shown earlier in this chapter.

3.2.2.1 APM optimization results

In order to see the effects of the polynomial degree N in the image quality of APMs, we have optimized masks of increasing polynomial degrees, from $N = 2$ up to $N = 7$, $N = 1$ was ignored since it just produces just a tip effect on the wavefront with no effect on the final quality. As with the BAPM optimization problem, we find that the solution landscapes are plagued with local maxima with very similar IQ_{opt} but vastly different profiles. To illustrate the different profiles found, we show in Fig.3.8 the generatrix of two of the optimal masks found for $\psi_{\text{max}} = 1.5\lambda$ and $N = 6$.

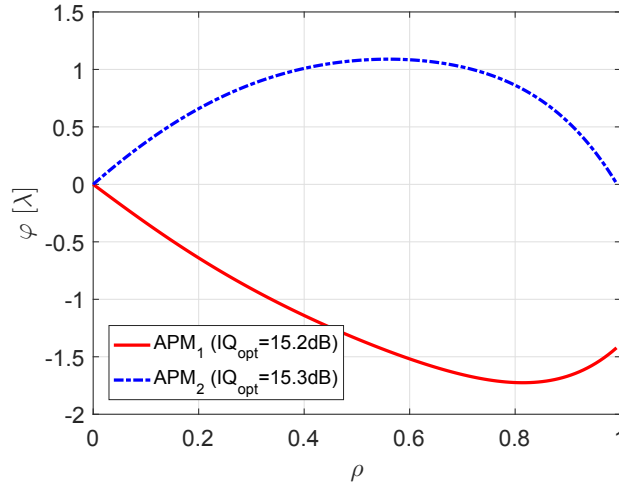


FIGURE 3.8: Profile comparison of two local maxima of aspheric phase masks optimized for $\psi_{\text{max}} = 1.5\lambda$ for $N = 6$.

As we can see in Fig.3.8, these two masks have very similar performance values IQ_{opt} , but their shapes have just a few similarities. The mask labeled APM₂, which has the best performance found for $N = 6$, has the profile with the least peak-to-valley change in phase; it increases, until it reaches its maximum at $\varphi(\rho = 0.6) = 1.1\lambda$ and then decreases until it reaches zero again. On the other hand, APM₁ seems to mirror APM₂ at low radii, growing in opposite directions at the same rate until $\rho = 0.2$, but while APM₂ slope becomes smaller, APM₁ continues to decrease until $\rho = 0.8$, where it increases slightly.

The two general mask behaviors that we observe in Fig. 3.8 were also found in most of the local optima, for all values of N , as we can see in Fig. 3.9 where we show the masks optimized for $N = \{2, 3, 4, 5, 6, 7\}$. The two patterns we have seen for $N = 6$ are all present here for masks with $N \geq 4$; we can appreciate that their IQ_{opt} values are very similar, increasing by only 0.1dB when passing from $N = 5$ to $N = 6$. It is interesting to notice that, as for the BAPMs, we have a quick increase of image quality when increasing the number of parameters, but we find an optimal shape — two in this case — at $N = 4$, and afterwards the performance levels-off.

Revolution polynomials are not commonly used to represent wavefronts in optical design, since they are usually unstable; after 40 particle swarm optimizations, with $20N$ random starting points, we have found the reported maxima only two to five times for $N \geq 5$. As briefly explained in section 2.4, more common polynomial bases to express wavefront shapes are the Zernike or Seidel polynomials, which are used

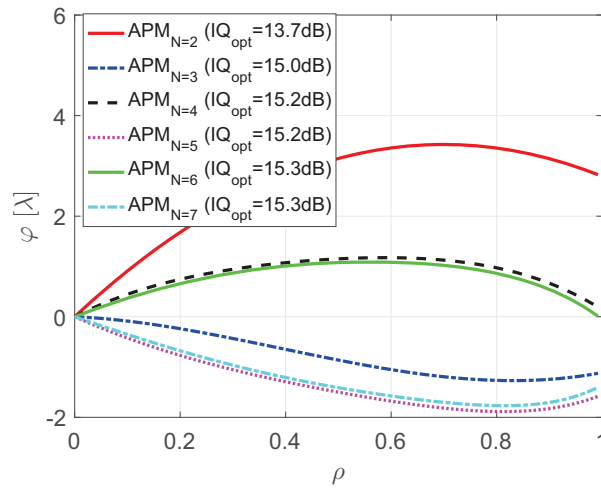


FIGURE 3.9: Profile comparison of different local maxima of aspheric phase masks optimized for $\psi_{\max} = 1.5\lambda$ for $N = \{2, 3, 4, 5, 6, 7\}$.

for aberrations but could be extended for phase masks for DoF extension. Another possible base are the Forbes polynomials (Forbes, 2010), proposed specifically for aspherical optical elements. Using the correct base to describe the phase mask will reduce the number of redundant optimization results and would ultimately provide optimal mask shapes more reliably. The only reference of such bases used for phase masks in DoF that we could find is relatively recent (Liu et al., 2016), and is used in photolithography, not in imaging optics, so there was no deconvolution stage.

3.2.2.2 APM performance comparison

In figure 3.10 we can see the image quality as a function of the defocus parameter ψ for the optimized APMs of degrees $N = \{2, \dots, 7\}$. We can appreciate that between $\psi = 0.25\lambda$ and $\psi = 1.25\lambda$, all masks have a performance between 15dB and 16dB and the main difference in their IQ_{opt} value comes to the point where their performance start dropping. As expected, masks with $N = 4, 6$ and $N = 5, 7$ have similar performance behaviors respectively. It is interesting to notice that the performances of $APM_{N=4}$ and $APM_{N=6}$ mirror almost perfectly the performance of $APM_{N=5}$ and $APM_{N=7}$ around $\psi = 0.75\lambda$, just in the middle of the desired DoF.

We can conclude from our observations of Fig. 3.9 and Fig. 3.10, that the two solutions found for $N = 6$ are equivalent, with negative mask profiles having slightly higher $IQ(\varphi, \psi)$ for the first half of the DoF while the masks with positive profiles having higher $IQ(\varphi, \psi)$ on the second half of the DoF range. We have found that this type of APMs have two local maxima of equivalent performance in opposite sides of the solution map.

3.2.3 Free-form phase masks

For a high enough number of parameters N , the aspheric polynomial masks can provide a great variety of rotationally symmetric continuous surface shapes, but the

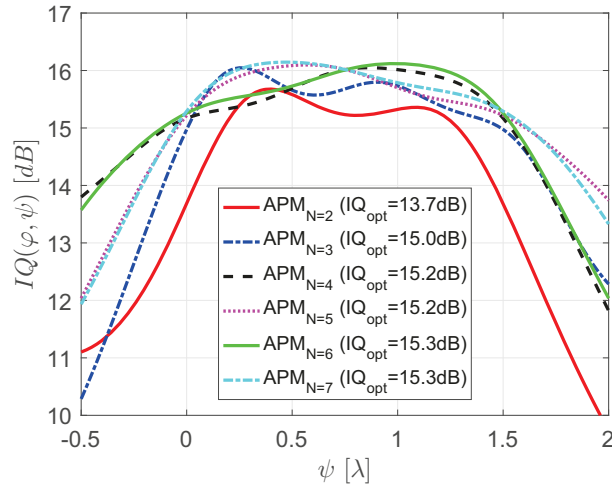


FIGURE 3.10: Performance comparison of aspheric phase masks optimized for $\psi_{\max} = 1.5\lambda$ as a function of ψ and for the polynomial order $N = \{2, 3, 4, 5, 6, 7\}$.

computational power to handle a large N , as well as the complexity of the problem, limit this versatility. For this reason, we propose the use of *free-form phase mask* (FFPM), a surface of revolution mask where the generatrix is a curve defined by a collection of evaluation points $\varphi_{ff}(\rho_{ff})$ of the phase over equidistant radii points $\rho_{ff} = \{\rho_0 = 0, \rho_1, \dots, \rho_{N-1}, \rho_N = 1\}$. These points are then connected by a cubic spline interpolation (Hazewinkel, 2001).

3.2.3.1 FFPM optimization results

Free form phase masks are conceived as a way to provide rotationally symmetric masks that can assume more freely a shape required by the DoF extension problem at hand. As we have seen on the optimizations of BAPM, PPM and APM, there are several local maxima that provide a similar performance; this is, unsurprisingly, also true for the FFPMs, the more optimization parameters are used in the optimization, the more local minima were found. We show in figure 3.11 optimal FFPM profiles, two for $N = 5$ and two for $N = 10$. These profiles have, for the same number of parameters, almost equal values of IQ_{opt} . Another important detail is that, although the shapes have considerably different values at each control point, the interpolated curves have points of inflection at very similar spots, reflecting each other's behavior, particularly for $\rho > 0.2$. This shows how that although several local maxima may exist, the optimal FFPMs tend to have similar effects on the wavefront.

We have plotted in figure 3.12 the generatrix curves of optimized FFPMs with control points $N \in \{2, 4, 6, 8, 10\}$. We do not show the odd-numbered profiles for the sake of conciseness and to not overcloud the other shapes. The main behavior that we can identify is that increasing the number of control points subsequently increases the complexity of the curve, producing several inflection points and even two crossings through zero for $N = 8$ and $N = 10$. It is interesting to notice that as the number of parameters increases, the masks seem to get a more stepped profile; with $N = 6$ we can recognize a rapid increase between $\rho \approx 0.2$ and $\rho \approx 0.3$, followed by a rather flat

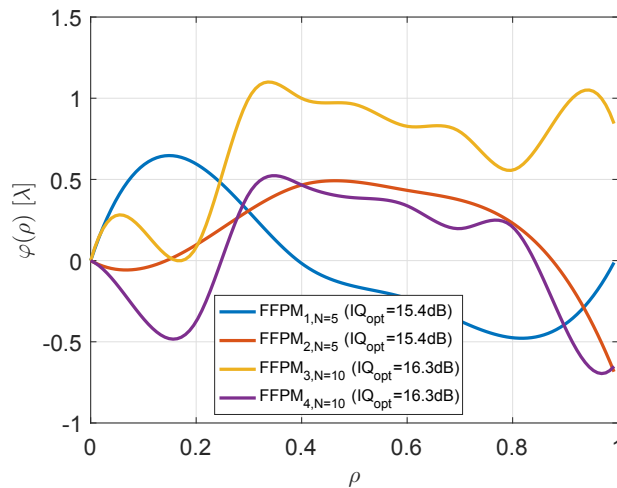


FIGURE 3.11: Profile comparison of four local maxima of free-form phase masks optimized for $\psi_{\max} = 1.5\lambda$ for $N = 5$ and $N = 10$.

area until $\rho = 0.8$, where the value of $\varphi(\rho)$ decreases again. This is true for $N = 8$ and $N = 10$, each one having steps and flat areas at similar values of ρ , but with a steeper change of profile at the steps as N increases.

Another interesting point coincides with what we have seen with APMs in the previous subsection: the best performing masks have shapes with values that stay closer to zero. This result may come from the fact that when having enough parameters, the mask can have the flexibility to vary more, better shaping the wavefront to the given need. On the other hand, when having less parameters the masks show stronger profiles. Since the effect on the wavefront of a point of the mask follows the rule $\varphi(\rho) + 1\lambda = \varphi(\rho)$, thus having profiles with values that cross $\varphi = 1\lambda$ effectively creates foldings on the profile, akin to the steps we see in more complex masks.

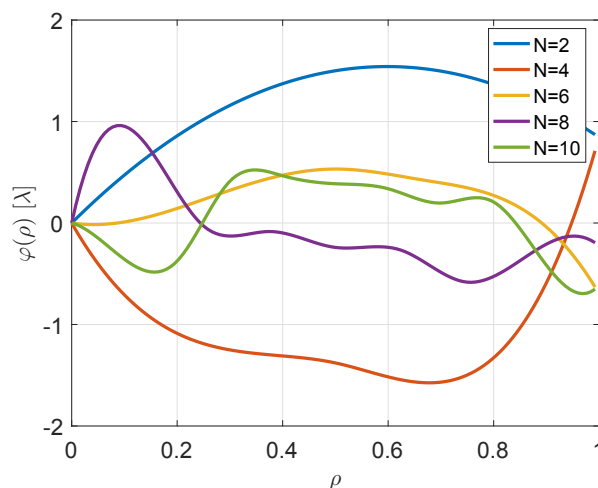


FIGURE 3.12: Profile comparison of FFPMs optimized for $\psi_{\max} = 1.5\lambda$ with $N = \{2, 4, 6, 8, 10\}$ equidistant control points.

3.2.3.2 FPPM performance comparison

To analyze the performance of the masks, we have plotted in figure 3.13 the value of $IQ(\varphi, \psi)$ as a function of the defocus parameter ψ for the cases with $N = \{2, 4, 6, 8, 10\}$ equidistant control points. We can see that the performance behavior is very similar when increasing the number of control points: a very fast increase on $IQ(\varphi, \psi)$ for $\psi > 0$, then a couple of semi-symmetric peaks around a shallow valley at $\psi \approx 0.75\lambda$ and then a steep descent after $\psi > \psi_{\max} = 1.5\lambda$.

Continuing the analysis of Fig. 3.13, we can see that, as the number of parameters increases, not only the value of IQ_{opt} increases, but also the performance becomes more symmetric throughout the DoF range, making the peaks flatter and the valley at the center more shallow.

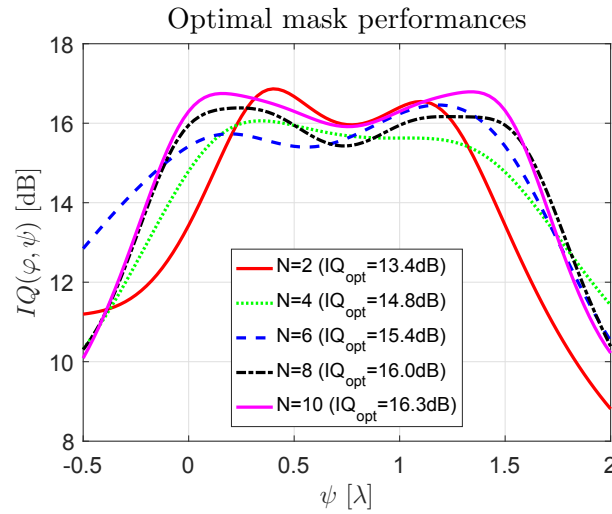


FIGURE 3.13: Performance comparison of FPPMs optimized for $\psi_{\max} = 1.5\lambda$ with $N = \{2, 4, 6, 8, 10\}$ equidistant control points.

This behavior has been observed for all the studied mask profiles; as the number of parameters increases, the gain in IQ_{opt} is less pronounced, but the masks tend to have a more stable performance, with less drops of $IQ(\varphi, \psi)$ throughout the DoF range.

3.2.4 Comparison of all optimized masks

We now study the best performing masks from each type of continuous phase masks we have explored throughout this section; the PPM, APM and FPPM. We compare them against each other and against the optimal BAPM found for the DoF $\psi_{\max} = 1.5\lambda$ with 5 rings. We start by comparing their profiles, as we did for each mask, and draw conclusions on their similarities and differences. Then, we compare their performance on the range $\psi \in [0, 1.5]\lambda$. Since the BAPM and the PPM masks have DoFs which are symmetric around $\psi = 0$, their effective DoF is of 3λ , so we end this section by comparing these two masks against APM and FPPM optimized for the same total DoF.

3.2.4.1 Different mask profile comparison

Figure 3.14 presents the 1-dimensional profiles of the PPM, APM, FFPM and BAPM. In the case of the PPM, we have chosen the profile along the x-axis, since it shows the largest phase amplitude of the mask and it is identical to the y-axis. We can see that all the masks have profiles of amplitude below 2λ , which coincides with our previous observations that optimal masks tend to have less ample profiles. An interesting comparison is between the FFPM and the BAPM: we see that their profiles tend to follow each other, with the FFPM having inflection points close to where the steps are on the BAPM, as well as similar (flat) areas between $\rho \approx 0.2$ and $\rho \approx 0.7$, although the FFPM seems to transition slightly later.

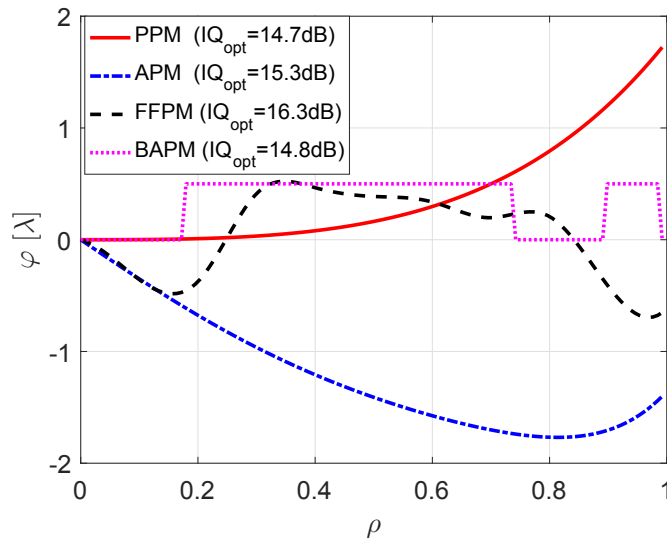


FIGURE 3.14: Profile comparison of the best polynomial, aspheric, free-form and binary phase masks optimized for the range $\psi \in [0, 1.5]\lambda$.

The fact that a mask with as much freedom on its profile as the FFPM converges to a profile that is akin to a BAPM is interesting. It supports the idea that, for a given DoF extension problem, there is an underlying optimal mask profile shape that co-optimized masks converge towards. It would seem that the BAPM is a binarization of this underlying mask profile folded at the points $\varphi(r) = \varphi(r) + 1$.

3.2.4.2 Performance comparison of different masks

As stated previously in this chapter, rotationally-symmetric continuous masks have a non-symmetric PSF around $\psi = 0$; for this reason, the revolution polynomials and the free-form masks optimized in this chapter have a DoF equivalent to the one used in optimization $[0, \psi_{\max}]$. On the other hand, PPM and BAPM have a DoF equivalent to $2\psi_{\max}$, but since the range of optimization was the same for all four masks, $[0, \psi_{\max}]$, we compare their performance as it is. At the end of this section we will include a comparison where the masks have the same full DoF.

In figure 3.15 the image quality is plotted as a function of the defocus value ψ for the best polynomial, aspheric, free-form and binary masks. We have expanded the

range to $\psi \in [-0.5, 2.0]\lambda$ so that we can better appreciate the drop on $IQ(\varphi, \psi)$ out of the desired DoF range. As it can be seen, the polynomial mask has the most stable value of $IQ(\varphi, \psi)$ over the DoF range; its performance is mostly flat and is higher than the BAPM up to half the DoF, at $\psi = 0.75\lambda$. On the other hand, we can see that the FFPM has a better performance than the other three, at all points, except a small area at the center of the DoF where its value $IQ(\varphi_{\text{FFPM}}, 0.75\lambda) = 15.9\text{dB}$ is slightly lower than the APM.

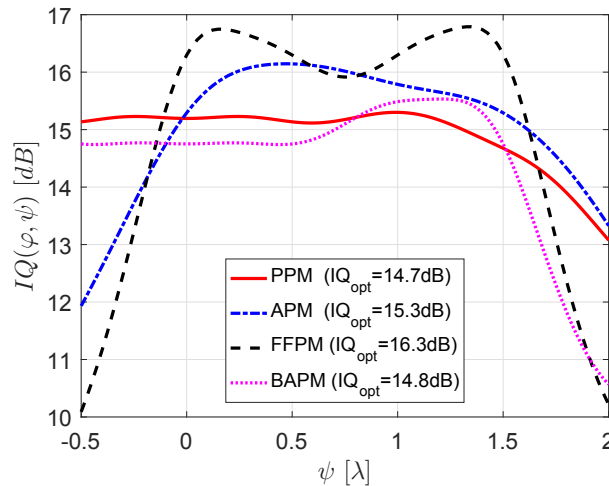


FIGURE 3.15: Performance comparison of polynomial, aspheric, free-form and binary phase masks optimized for $\psi_{\text{max}} = 1.5\lambda$ as a function of ψ .

3.2.4.3 Comparison at the full depth of field

On our examples throughout this chapter we have used a total DoF of 1.5λ for the APM and FFPM whereas the PPM and BAPM, having a symmetric IQ around $\psi = 0$, have a total DoF range of 3.0λ . To truly compare the mask performances, we have optimized new sets of masks for each relevant total DoF range. For a total DoF range of 1.5λ , we optimized a 4-ring BAPM and a 5th degree PPM on the $\psi \in [-0.75, 0.75]\lambda$ range. For a total DoF range of 3.0λ , we have also optimized a 6th degree APM and a FFPM with 10 control points for $\psi \in [0, 3]\lambda$. In figure 3.16 we show the values of $IQ(\varphi, \psi)$ as a function of ψ . We have plotted the IQ in such a way that the DoFs of each mask overlap, therefore for the PPM and the BAPM the range of ψ is shifted by a value of ψ_{max} towards the positive side of the DoF.

In Fig. 3.16.a) we can see that $IQ(\varphi, \psi)$ for the PPM, the FFPM and the BAPM have very similar M -shapes, with a valley just at the center of the DoF, whereas the APM has an asymmetric shape, with its maximum at $\psi \approx 0.5\lambda$. We can see that in this case, it is the BAPM who shows the best performance at all points, followed by the FFPM by 0.5dB in practically all the DoF and by the PPM by 0.7dB. On the other hand in Fig. 3.16.b) we can see a bigger difference on the profiles; the BAPM and the FFPM have similar M -shaped profiles, although the BAPM is vastly superior, whereas the PPM has a more flat shape with only lower values than the BAPM close to the edges of the DoF. In this instance, the APM copes similarly to the FFPM, but, as we have seen before, with a non-symmetric profile.

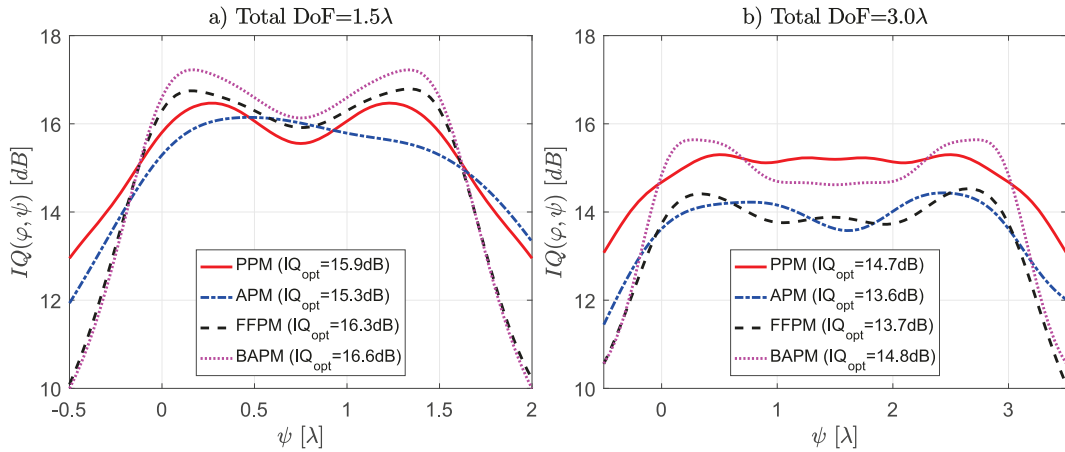


FIGURE 3.16: Performance comparison of polynomial, aspheric, free-form and binary phase masks with the same total DoF, the plots for the PPM and the BAPM have been shifted by ψ_{max} so that the total DoFs overlap. a) Masks optimized for a total DoF range of $2\psi_{\text{max}} = 1.5\lambda$ and b) masks optimized for a total DoF range of $2\psi_{\text{max}} = 3.0\lambda$.

From the observations of figure 3.16 we can gather that the BAPMs are the best performing masks for small DoF ranges, and are on-par to the PPMs for a total DoF range 3λ . Also that the optima we found for circularly symmetric masks such as APMs and FFPMs have a comparable performance to the BAPM and PPM for low DoF, but get quickly outclassed when the DoF increases. It is necessary to notice that due to the high complexity of the optimization problem, particularly for APMs and FFPM, we can never be sure to have found the true optimum, but we are confident that the results shown are representative of the behaviors of the masks. Indeed, the numerous initialization values led to solutions where most local maxima found for APM and FFPM had a similar IQ_{opt} value.

Finally, we can see that since the value of IQ_{opt} for BAPMs and PPMs is more similar when the DoF range doubles, it hints that for larger DoF ranges the PPMs may have better performance than the BAPMs. This result is in good agreement with the ones obtained by Frédéric Diaz in his doctoral thesis (Diaz, 2011) where it is shown that BAPMs have a better performance than PPMs for low DoF, but after a certain threshold, the performance of the PPM takes over.

3.3 Hybrid system response for different masks

Throughout this chapter we have studied the performance of a collection of masks used for depth of field extension. As we have shown, the MTF or PSF provide additional information on the performance behavior of these co-optimized systems and allow for a more thorough comparison of different masks when used along with the image quality criteria.

In this section we use the PSF and the effective MTF, defined in chapter 2, to analyze the different optimal masks we have studied throughout this chapter. We start by drawing the PSF spot as a function of the defocus, then we study the effective MTF

and we finally assess the visual quality of the image, so that we can draw conclusions based on our analysis of the MTF and PSF.

3.3.1 Impulse response comparison

In chapter 1 we have described the effect of the system on a point source of the object as the point spread function h_{ψ}^{φ} on equation (1.10). The PSF of the optical system with a mask is directly related to the final image quality, both due to its effect on the captured image and because it is essential to calculate the deconvolution filter (Eq. (1.29)).

In figure 3.17 we show a cut of the PSF across the X-axis calculated at values of defocus on the range $\psi \in [-2, 2]\lambda$ for the following masks: a PPM, an APM, a FFPM and a BAPM optimized for a DoF range of $\psi \in [0, 1.5]\lambda$. The PSF of the cubic phase mask and the quartic phase mask has already been shown on figure 2.2 on chapter 2 and, for the sake of conciseness, will not be included. We have also plotted the PSF cut a conventional maskless system for comparison. The first that can be observed is that for all the masks their PSF spot varies considerably across the ψ range, this is the result of the IQ_{\min} criterion since it does not require invariability. Even more, we can see a direct correlation between the variation of the PSFs of each mask and the variations of IQ shown on 3.16.

We can see that the PSF of the maskless system diverges greatly for values $|\psi| > 0.25\lambda$, as is expected from the Marechal criterion. In the case of the PPM, we see that the DoF is curved, as it is for the CPM, and extends quasi-invariantly beyond the required DoF and up to $|\psi| = 2.0\lambda$. The APM on the other hand presents an asymmetric PSF, being very weak out of the range $\psi \in [-0.25, 1.5]\lambda$. For the FFPM the PSF is better in the range $\psi \in [-0.25, 1.75]\lambda$, but is symmetric around $\psi = 0.75\lambda$ and has a rather similar profile to the BAPM but shifted towards positive values of ψ . If we go back to figure 3.15, we can see that the behavior of $IQ(\varphi, \psi)$ as a function of ψ correlates with the PSF: where $IQ(\varphi, \psi)$ is higher, the PSF is narrower, whereas the drops of $IQ(\varphi, \psi)$ correspond to points where the PSF is more disperse. It is worth noticing that although these results show a clear correlation between the PSF shape and the image quality, it is not possible to directly deduce the quality of the final image from the PSF since there is an intermediate deconvolution step.

On figure 3.18 we show the PSF spots produced by systems with the APM, PPM, FFPM and the BAPM for defocus values $\psi = \{0, 0.75, 1.5\}\lambda$. These PSF spots confirm the observations from 3.17 and show us the shape of the PPM PSF, which is similar to the PSF of the CPM but with a more curved spread. For the FFPM the central spot is the broadest at $\psi = 0.75\lambda$ while the much smaller spots at $\psi = 0$ and $\psi = 1.5\lambda$ are quasi-identical close to the center. We see some faint external rings on $\psi = 1.5\lambda$ which do not appear at $\psi = 0$; this difference does not seem to hamper the performance after deconvolution as seen on Fig. 3.15. The BAPM has a seemingly different spot at each value of ψ shown, having the central spot of $\psi = 0$ and $\psi = 0.75\lambda$ being rather similar but with fairly different rings around them. As we know, the value of $IQ(\varphi, \psi)$ at $\psi = 0$ and $\psi = 0.75\lambda$ is very similar and is over 0.8dB lower than for $\psi = 1.5$ (see Fig. 3.15), showing, as for the FFPM, that the central spot of the PSF has the largest influence in the performance. This last result shows that, once again, having a completely invariant PSF is not a requirement for DoF extension.

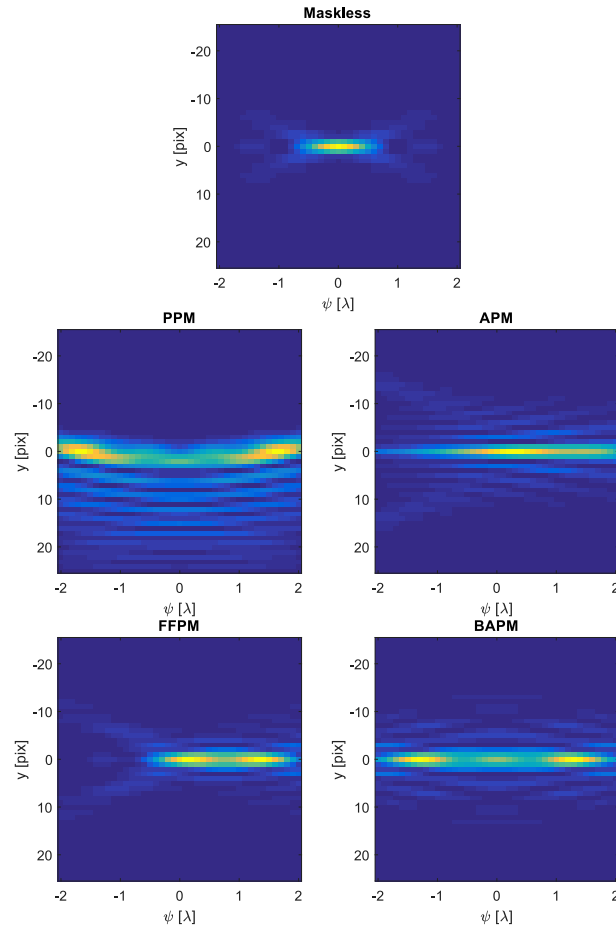


FIGURE 3.17: Comparison of the PSF profile across the DoF range of systems with polynomial, aspherical, free-form and binary annular phase masks optimized for $\psi_{\max} = 1.5\lambda$.

3.3.2 Frequency response comparison

Through chapters 1 and 2 we have shown how the frequency response of a hybrid optical system, with a phase mask and deconvolution, can be more effectively studied by using an effective modulation transfer function that considers the effects of the deconvolution in the final stage.

In figure 3.19 we have plotted the effective MTF for the systems with circularly symmetric masks optimized for $\psi_{\max} = 1.5\lambda$: the QPM, the APM, the FFPM and the BAPM at the defocus distances $\psi = \{0, 0.75, 1.5\}\lambda$. Since these masks and the PSD model of the scene are both circularly symmetric, the effective MTF of these masks is circularly symmetric as well and any radial profile of the MTF fully describes it. As a reference we also show the MTFs of each system with a phase mask before deconvolution. For the QPM we see that the effective MTF is different at each defocus value; at $\psi = 0$ in particular we can see a valley on the MTF at $\mu \approx 0.21$ which translates as strong decrease in contrast for that spatial frequency. Additionally, although the effective MTFs for $\psi = 0$ and $\psi = 0.75\lambda$ are different, we can see in figure 3.2 that their image qualities are similar at $IQ \approx 14.5\text{dB}$. The cutoff created by the mask is at $\mu = 0.5$ for $\psi = \{0, 0.75\}\lambda$ and $\mu = 0.37$ for $\psi = 1.5\lambda$, coinciding with the reduction of IQ at this defocus value compared to the other two. This low-pass effect we

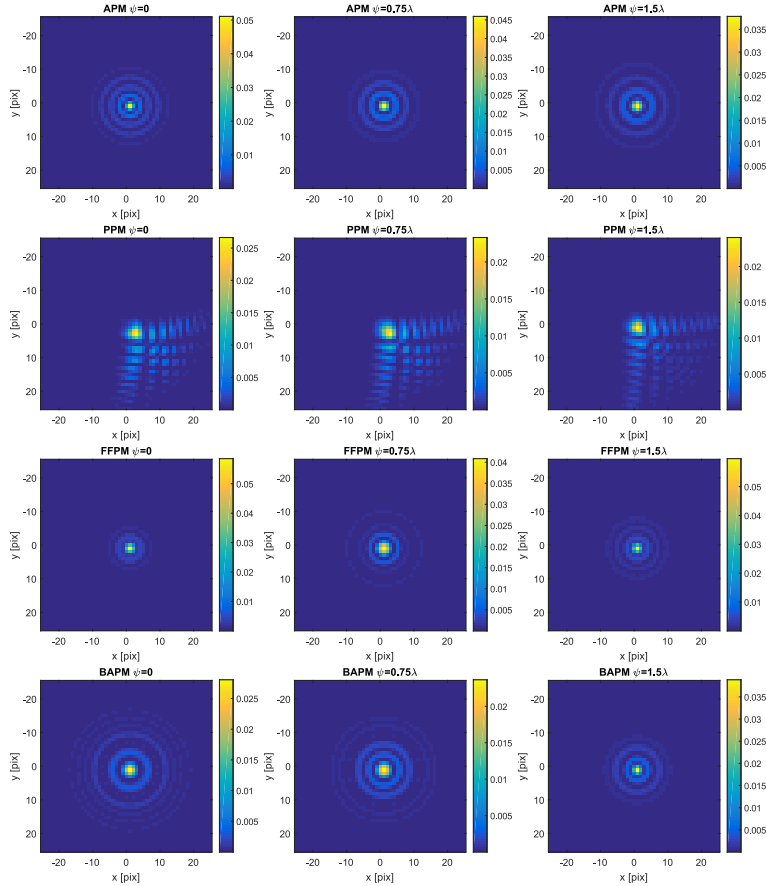


FIGURE 3.18: Comparison of the PSF generated by, from top to bottom: a system with an APM, a system with a PPM, a system with a FFPM and a BAPM at defocus distances $\psi = 0$ (left), $\psi = 0.75\lambda$ (middle) and $\psi = 1.5\lambda$ (right).

observe at all values of ψ explains the overall lower IQ of the QPM compared to the other masks which have a cutoff at higher spatial frequencies.

The effective MTF of the APM on Fig. 3.19 shows a cutoff at $\mu = 0.85$ for $\psi = 0$ and $\mu = 0.78$ for the other two defocus points. As for the QPM, the MTFs are not identical, but their shape does not diverge from each other as much as for the QPM. From figure 3.15, we can see that the image quality has a value $IQ \approx 15.4\text{dB}$ at $\psi = 0$ and $\psi = 1.5\lambda$, whereas it is slightly higher at $\psi = 0.75\lambda$. There is a correspondence between these values of the image quality and the shapes of the MTFs: the values of the MTF at $\psi = 0$ are lower than for $\psi = 0.75\lambda$ for most of the spatial frequencies, on the other hand, for $\psi = 1.5\lambda$ the MTF has a shorter cutoff frequency, which explains the lower IQ value.

Passing to the FFPM in figure 3.19 we see that the the effective MTF values for all defocus points are very similar until $\mu = 0.6$, where the MTF for $\psi = 0.75\lambda$ drops sharply to a cutoff frequency of $\mu_c = 0.65$ whereas the other two have their cutoff frequency at $\mu = 0.8$. This is very consistent with behavior of IQ on figure 3.15, where the performance at $\psi = 0$ and $\psi = 1.5\lambda$ are very similar and is significantly lower for $\psi = 0.75\lambda$.

The BAPM presents, on the other hand, an MTF that varies more across the DoF than

the FFPM and with a narrower cutoff than the APM and FFPM, which coincides with its relatively lower IQ value observed. Once again, we see in figure 3.19 that the defocus point with the highest IQ , $\psi = 1.5\lambda$, has also a cutoff that is slightly higher, at $\mu = 0.71$ than the other two ψ points at $\mu = 0.63$.

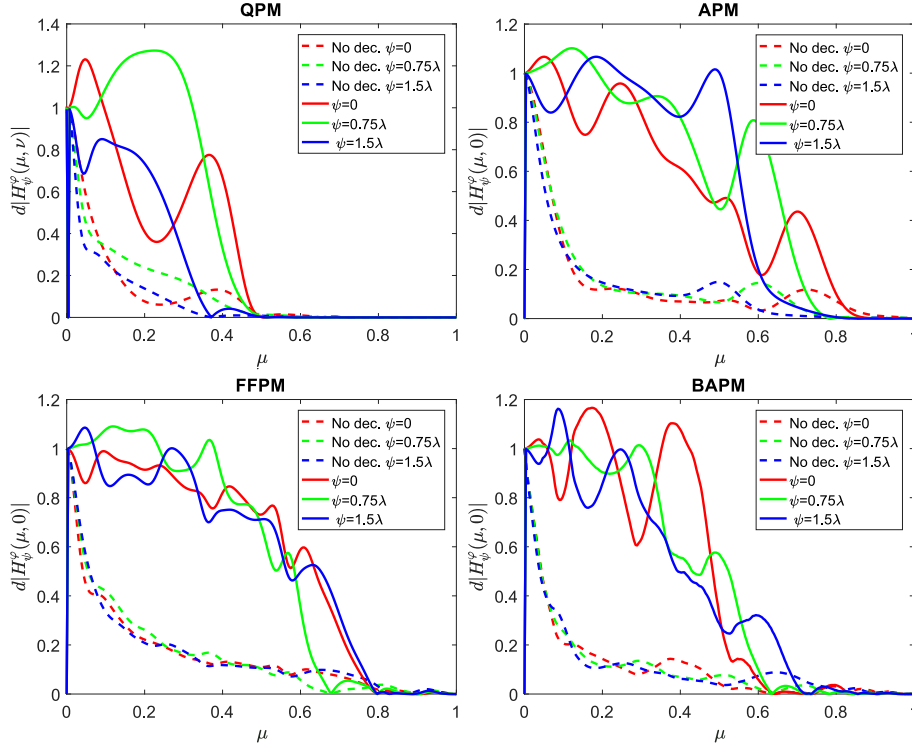


FIGURE 3.19: Comparison of the effective MTF at different defocus values produced by: a QPM, an APM, a FFPM and a BAPM

The analysis along the μ axis we performed of figure 3.19 was only possible because of the rotational symmetries of the system. Polynomial phase masks, as we have seen earlier in this section, do not possess a circularly symmetric profile, and thus their MTF is not either. For this reason, on figure 3.20 we show both the effective MTF over the μ axis and over the diagonal $\mu = -\nu$. At first glance, the plots on the μ axis make it look like these masks have better DoF enhancing properties than the other masks, having a larger cutoff frequency and MTF that does not diverge too much. But we see that on the diagonal this is not true; the CPM has some sharp drops on the MTF at low frequencies, particularly for $\psi = 0$ at $\mu = \nu = 0.16$ and the cutoff is down to $\mu = 0.6$.

For the PPM we have a similar behavior as for the CPM, we see again the drops on the MTF for low frequencies, but with a lower amplitude, and a faster drop towards the cutoff frequency than the cut across the μ axis. We saw previously on figure 3.15 that the PPM and the BAPM have comparable performances at this DoF range, and from the shape of their effective MTF we can conclude that, although the effective MTF of the PPM across the μ axis is better than the one of the BAPM, the fact that the effective MTF across the $\mu = -\nu$ diagonal is relatively worse ends up producing a similar IQ value.

This is an interesting result to consider in terms of applications, since the PPMs will introduce artifacts on the diagonal sections of the deconvolved image, whereas the

BAPMs introduce artifacts spread symmetrically around each spot. The choice of the mask therefore is strongly application dependent, in an industrial inspection environment, where the samples are neatly organized in a grid, it may be more interesting to have a very good spatial resolution across the x and y axes, whereas in a surveillance situation, the user does not a-priori know the scene and may prioritize having an acceptable resolution in all directions.

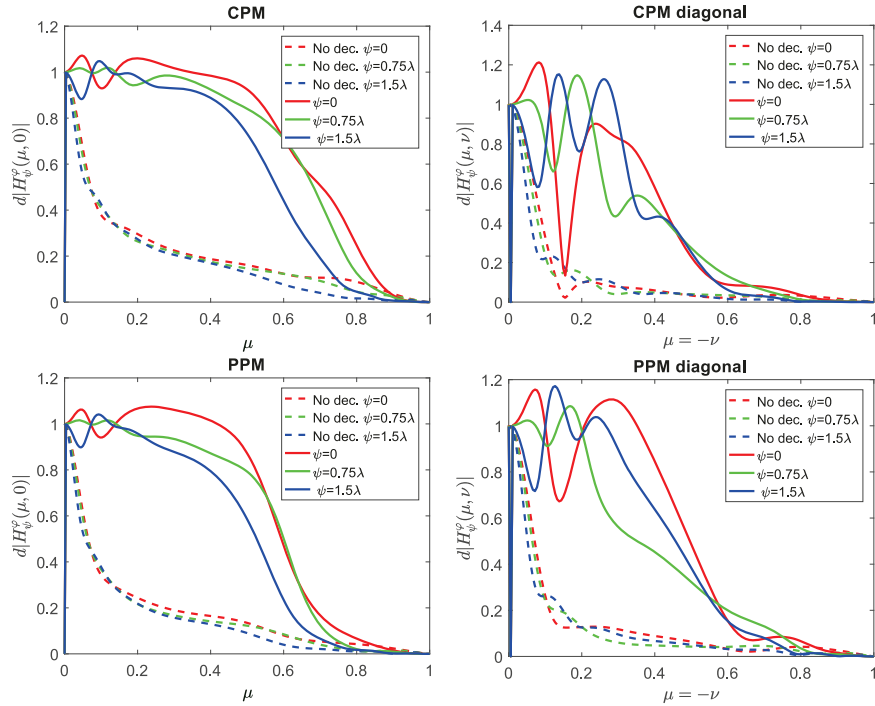


FIGURE 3.20: Comparison of the effective MTF at different defocus values produced by a CPM and a PPM: along the μ -axis (left) and on the $\mu = -\nu$ diagonal (right).

We have shown that most of the shown hybrid systems reduce the cutoff frequency as compared to the diffraction limited optical system they are based on. The final image quality comes as a trade off between keeping this new cutoff as large as possible and keeping the effective MTF high for the frequencies that fall below this cutoff. We have also shown that the use of a single averaged deconvolution filter naturally leads the system co-optimization to have MTFs through the DoF range that are similar, since disparities in the MTF are amplified when applying the Wiener filter, leading to a potential loss of contrast in certain frequencies at certain defocus distances.

3.3.3 Visual comparison of the frequency response

Throughout this section we have illustrated how the co-designed systems respond in the spatial domain with the PSF and, in the frequency domain, with the effective MTF. In this section we will study the cases of the BAPM and the CPM and we will draw connections between their effective MTFs and PSFs and the final images each co-designed system produces. A thorough analysis of the response of CPMs and its relation with artifacts was performed in (Demenikov and Harvey, 2010) where they

analytically find the causes of artifacts, but in their analysis they deconvolve using the inverse PSF on focus, instead of an averaged Wiener filter, and noise was not considered. They found that the artifacts in systems with CPMs can be predicted by analyzing the modulation and phase transfer functions and demonstrated that the artifacts are produced by phase mismatches between the deconvolution filter and the OTF of the optical system.

It is not always simple to visually interpret the behaviors seen in the system response on a natural scene, such as the picture of the butterfly (see Fig. 2.9) shown before. In figure 3.21 we have used a radial frequency target that allows us to clearly observe some of the artifacts that are apparent in the effective MTF. On Fig. 3.21 (top) we show the computer generated target (left) and the target after passing through a diffraction limited system for comparison. The ring radii go from 2 pixels, (which is $\nu = 1.0$, our Nyquist frequency) up to 16 pixels ($\nu = 0.13$) at the outer ring. On figure 3.21 (bottom) we show the same target after passing through the co-designed systems with a BAPM (left) and CPM (right). On the system with the BAPM we can see distinct "ripple" artifact at the edge of each ring and is particularly noticeable after the outer ring. On the system with the CPM we see the presence of a similar artifact on the bottom-right quadrant and less pronounced on the top-right and bottom-left quadrants. These artifacts are a vestige from a highly asymmetric and downwards spread PSF, typical of the polynomial-profiled masks we see in figures 2.2 and 3.18.

On figure 3.22 we show a detail on the bottom-right quadrant of the images shown in figure 3.21. We can see that the image produced by the BAPM system is blurred at the center, so much that the central dark spot has completely disappeared. We can spot other artifacts on this image, such as the gray lines on the center of most rings. For the CPM we see a clear blur spreading from the center towards the bottom-right corner of the image. It is interesting to notice that on the x and y axes the image is sharper than with the binary mask, confirming our predictions based on the effective MTFs, where we saw that the polynomial masks present MTFs with high values on the axes but gets lower on the diagonals.

3.4 Conclusions

In conventional design, the optical engineer usually optimizes the optical system based on the value of an objective function which is crafted based on several optical properties of the designed system, such as RMS value of different aberrations, Strehl ratio, MTF values, among others. On the case of hybrid optical systems, co-optimizing using these metrics only may lead to sub-optimal designs since they do not directly consider the deconvolution step. In chapters 1 and 2 we used the work of (Diaz, 2011) to develop a series of optimization and analysis tools that are more pertinent to the design of hybrid imaging systems.

We have shown in this chapter the importance of the choice of the metric and that IQ is a strong metric that, by design, yields better performances than other traditional ones such as the Strehl ratio, which may lead to wrong assumptions on the total DoF range, or the invariability of the MTF, which often produces masks with an unnecessarily strong profile causing artifacts and noise amplification upon deconvolution.

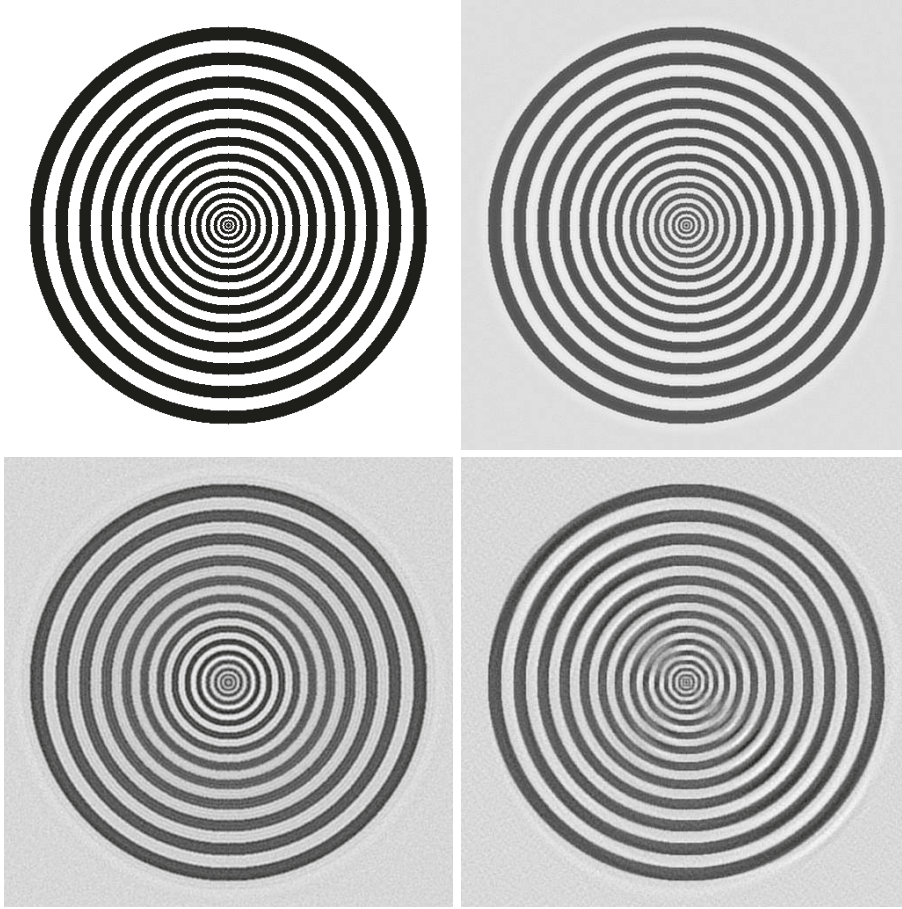


FIGURE 3.21: Comparison of the images of a bullseye target after passing through different optical systems at $\psi = 0$: (top-left) the scene, (top-right) an on-focus diffraction limited system without deconvolution, (bottom-right) a hybrid system with a CPM and (bottom-left) a hybrid system with a BAPM

Then we have shown that in the context of the IQ criterion, the maximin optimization produces masks with better performance than using the mean optimization or, as we mentioned before, the invariance over the DoF range.

We then made use of this criterion and optimization methodology to co-design and compare a series of types of continuous-phase masks commonly found in literature, such as the QPM, the CPM and their generalized forms, the APM and the PPM respectively. We proposed for analysis another mask, the FFPM, whose profile is defined by the phase values of a series of control points on the radius. There are other hybrid systems in literature we have not covered, such as the exponential phase mask (Yang, Liu, and Sun, 2007) or the sinusoidal phase mask (Zhao and Li, 2010), and we believe that the analysis tools presented in this chapter can be used by anyone interested in co-design for DoF extension and even other co-design tasks with any kind of wavefront coding masks.

We have obtained that most masks have an increasing performance as the parameters increase, and levels-off at a certain number of parameters, as we originally observed for the BAPMs.

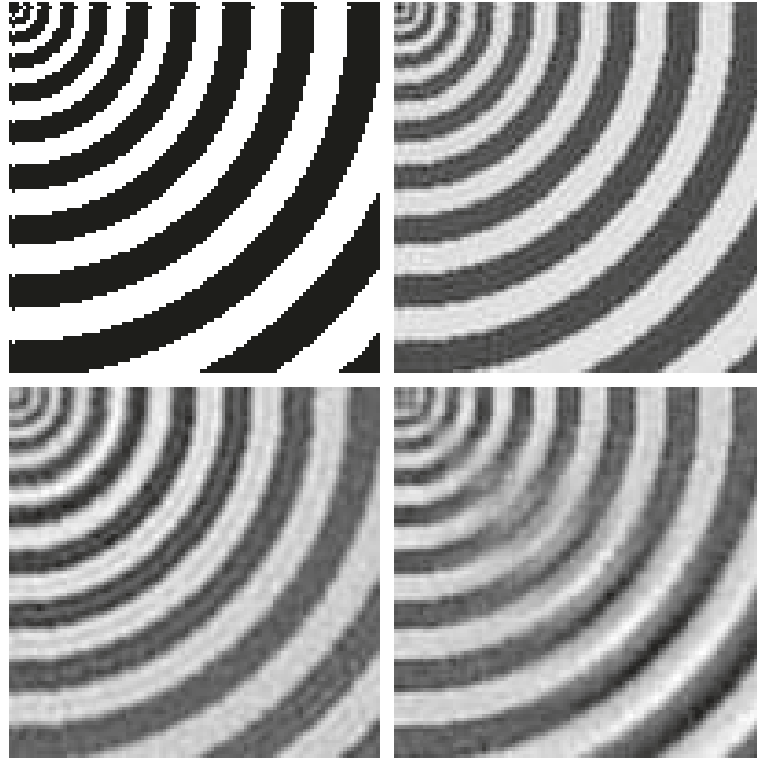


FIGURE 3.22: Detail of the images of a bullseye target after passing through different optical systems at $\psi = 0$: (top-left) the scene, (top-right) a diffraction limited system without deconvolution, (bottom-right) a hybrid system with a CPM and (bottom-left) a hybrid system with a BAPM

The case of the FFPMs is interesting; when enough parameters are added, the optimal FFPM masks seem to have steps, not unlike the profile of a BAPM although no condition was introduced enforcing this behavior. This agrees with the notion that there is an underlying mask profile that is ideal for a given optimization problem and for low total DoF ranges, such as 1.5λ , the BAPM seems to have the best performance from the studied masks. On the other hand, for larger DoF ranges, 3.0λ in our case, the PPM seems to perform marginally better than the BAPM, coinciding with the observations of (Diaz, 2011) when comparing phase masks.

The shape of the PSF is a preliminary indicator of the performance of the system; by seeing the PSF spot we can predict the general shape and distribution of the artifacts that may be present in the final image. With the diagram of the PSF as a function of ψ we can also draw connections between the overall performance, $IQ(\varphi, \psi)$, and the mask's shape. The main limitation of the PSF is that it does not consider deconvolution, so the observations do not necessarily predict performance. The effective MTF on the other hand has the advantage of showing the response with the filtering included. Thanks to this metric we have seen that most of the phase masks reduce the effective cutoff frequency of the optical system, causing information loss that cannot be recovered by deconvolution. The final image quality depends strongly of this cutoff frequency, but also on the contrast of the frequencies after deconvolution.

The analysis of the frequency response of the phase masks becomes more important when they are being added to optical systems that are not diffraction limited. When

considering the pixel size for example, an undersampled conventional system has a longer DoF than a system that is diffraction limited, since the pixel size is relatively larger than the PSF spot. Additionally, techniques such as superresolution make use of the aliasing of oversampled images to form a high resolution image past the diffraction limit. To achieve this, it requires the sampling frequency to be many times shorter than the cutoff frequency, therefore, a mask envisioned for both DoF extension and superresolution cannot have too-short cutoff frequency. We will devote the next chapter to the study of the performance of phase masks for DoF extension when the detector's sampling and possible aliasing are considered.

Chapter 4

Aliasing of hybrid systems and superresolution

Most modern optical systems work with solid state sensor arrays, which discretize the continuous image generated by the optical system in a process called sampling. Except for very specific systems, such as astronomical telescopes and some infrared systems, the discretization is such that the PSF of the diffraction limited system is not properly sampled. This means that the Nyquist frequency of the detector is smaller than the optical cutoff frequency of the diffraction limited system. In this case, frequencies above the Nyquist frequency (and below the cutoff frequency) will be folded below the Nyquist frequency leading to a loss of spatial resolution. In this case, we will say that there is undersampling.

We start this chapter by describing the discretization process and how undersampling in conventional systems generates an undesired artifact called aliasing. Then we illustrate the recovering of frequencies beyond the Nyquist frequency using superresolution, which combines a series of aliased low-resolution images to obtain one image with higher resolution after post-processing, using the simple shift-and-add algorithm (Elad and Hel-Or, 2001). We then present the experimental results obtained along with the industrial partner KLA-Tencor, where superresolution was used to improve the detection of imperfections in microcomponents. We conclude the chapter by considering the case of aliasing on hybrid systems for DoF extension and showcase the situations where superresolution is relevant.

4.1 Effects of sampling on a conventional system

In this section we mathematically describe the sampling process and show its effects on a conventional system. From this description we define the aliasing artifact and how it affects the quality of the captured image.

4.1.1 Sampling on a conventional system

In chapter one we described the image formation process of an optical system under the assumption that the system was well sampled, this is the cutoff frequency ν_c and the sampling frequency ν_s are such that $\nu_c/\nu_s < 0.5$. According to the Shannon-Nyquist theorem, the corresponding diffraction limited system has no loss of frequency information due to discretization. This assumption allowed us to disregard

the different effects of sampling from our calculations. In reality, many optical systems, such as photographic cameras and video cameras, are deliberately made so that $\bar{\nu}_c = \nu_c/\nu_s > 0.5$, where $\bar{\nu}_c$ is known as the effective cutoff frequency of the system. This measurement is rather useful, since the undersampling factor $2\bar{\nu}_c$ represents how much larger is the pixel pitch p as compared to a pixel pitch that satisfies the Shannon-Nyquist criterion.

To model the effect of sampling on the produced image, we start by the definition of the continuous image $I(x, y)$ of the scene $O(x_o, y_o)$ projected in the image plane after passing through the optical system of PSF h :

$$I(x, y) = h(x, y) * O(x, y).$$

If we consider a detector with squared pixels and a 100% fill factor, the pixel pitch and the pixel lateral size are identical and the sampling frequency is $\nu_s = 1/p$. In the following, we will work with the a detector of $N \times N$ pixels of size $p \times p$ so that we can model the sampled image $I_s(n, m)$ as:

$$I_s(ip, jp) = \text{III}_p(x, y) \cdot [\text{II}_p(x, y) * I(x, y)] + n(ip, jp), \quad (4.1)$$

where $\text{III}_p(x, y) = \sum_{i=0}^{N-1} \sum_{j=0}^{N-1} \delta(x - ip, y - jp)$ is 2-dimensional Dirac comb which represents the position of each pixel of the detector array and $\text{II}_p(x, y)$ is a box function defined as

$$\text{II}_p(x, y) = \begin{cases} 1 & |x| < p/2 \text{ and } |y| < p/2, \\ 0 & \text{otherwise,} \end{cases}$$

which represents the windowing produced by the pixel. The Fourier transform of the box function of width p is a sinus cardinal of pseudo-period $2/p$ and that for a comb function of period p the Fourier transform is a comb of period $\nu_s = 1/p$. We can now write equation (4.1) in a more convenient form in the Fourier domain:

$$\tilde{I}_s(\mu, \nu) = [\text{sinc}(\mu p) \cdot \text{sinc}(\nu p) \cdot \tilde{h}(\mu, \nu) \cdot \tilde{O}(\mu, \nu)] * \text{III}_{\nu_s}(\mu, \nu) + \tilde{n}(\mu, \nu). \quad (4.2)$$

From this expression we can recognize the MTF of the sampled system (called hereafter sampled MTF), $\tilde{h}_s(\mu, \nu)$ expressed as:

$$\tilde{h}_s(\mu, \nu) = [\text{sinc}(\mu p) \cdot \text{sinc}(\nu p) \cdot \tilde{h}(\mu, \nu)] * \text{III}_{\nu_s}(\mu, \nu). \quad (4.3)$$

The first zero of the centered $\text{sinc}(\mu p)$ functions is at $\nu_s = 1/p$ and the comb function produces replicas of the continuous MTF centered at ν_s . For this reason, as shown in figure 4.1, the replica MTFs are beyond the cutoff frequency and do not affect the system MTF. For such systems we used in previous chapters the approximation that $\tilde{h} \approx \tilde{h}_s$.

The pixel box function is usually overlooked in most calculations that involve sampling since the first zero of its Fourier transform is at the sampling frequency ν_s . From now on, we include the pixel windowing function directly in the PSF of the

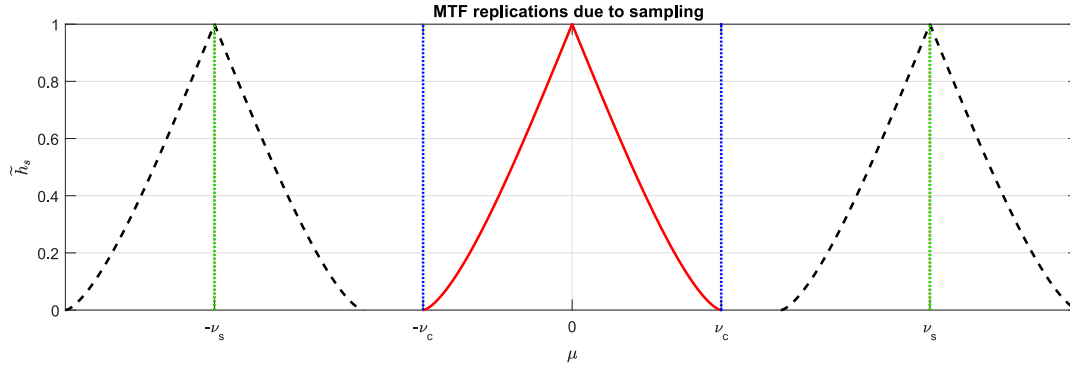


FIGURE 4.1: Replication of the MTF in a properly sampled optical system where $\bar{\nu}_c = 0.4$. The red line represents the detected MTF and the black dashed lines represent the replicas. The blue dotted lines marks the cutoff frequency, while the green dotted lines mark the sampling frequency.

optical system h , so that it will be included in all deconvolution filters in the following sections. With this assumption we can simplify equation (4.1) as:

$$I(i/\nu_s, j/\nu_s) = \text{III}_p(x, y) \cdot [h(x, y) * O(x, y)] + n(i/\nu_s, j/\nu_s), \quad (4.4)$$

$$= \sum_{i=0}^N \sum_{j=0}^N \delta(x - i/\nu_s, y - j/\nu_s) \cdot [h(x, y) * O(x, y)] + n(i/\nu_s, j/\nu_s), \quad (4.5)$$

$$= \sum_{i=0}^N \sum_{j=0}^N h(i/\nu_s, j/\nu_s) * O(i/\nu_s, j/\nu_s) + n(i/\nu_s, j/\nu_s), \quad (4.6)$$

where the nomenclature convention for the Dirac delta

$$f(k) = \delta(x - k)f(x) \quad (4.7)$$

has been used.

4.1.2 Aliasing

As it has been mentioned at the beginning of this chapter, many conventional optical systems do not satisfy the Shannon-Nyquist theorem. From equation (4.3), we can use the Dirac delta convention from (4.7) to separate the spurious signal from the initial MTF:

$$\tilde{h}_s(\mu, \nu) = \sum_{\tilde{i} \in \mathbb{Z}} \sum_{\tilde{j} \in \mathbb{Z}} \tilde{h}(\mu - \tilde{i}\nu_s, \nu - \tilde{j}\nu_s) \quad (4.8)$$

$$= \tilde{h}(\mu, \nu) + \sum_{\tilde{i} \in \mathbb{Z} \setminus 0} \sum_{\tilde{j} \in \mathbb{Z} \setminus 0} \tilde{h}(\mu - \tilde{i}\nu_s, \nu - \tilde{j}\nu_s). \quad (4.9)$$

Equation (4.9) is the classical result that the sampled MTF is the infinite sum of the initial MTFs shifted by integer multiples ν_s , or equivalently that the sampled MTF corresponds to the periodisation of the initial MTF. In figure 4.2 we show what happens to the sampled MTF \tilde{h}_s with an undersampling $\bar{\nu}_c = 0.75$. As we can see now, part of the replicas of the MTF are folded within the cutoff frequency.

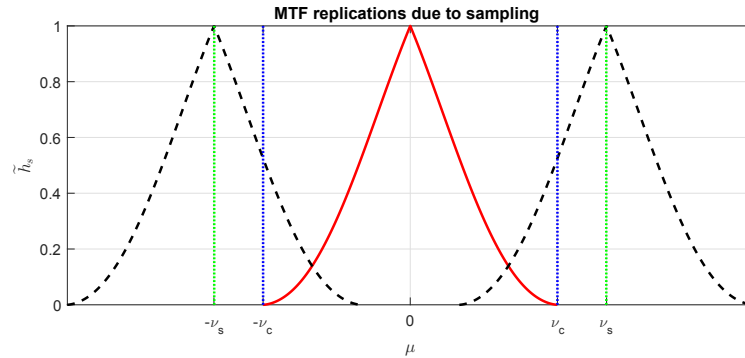


FIGURE 4.2: Replication of the MTF of a sampled optical system where $\bar{\nu}_c = 0.75$. The red line represents the portion of the MTF within the cutoff frequency and the black dashed lines represent the replicas. The blue dotted lines mark the cutoff frequency, while the green dotted lines mark the sampling frequency.

In figure 4.3 we show the effect of this folding on the sampled MTF. This artificially increases the contrast of some high spatial frequencies of the discrete image, which is commonly known as aliasing.

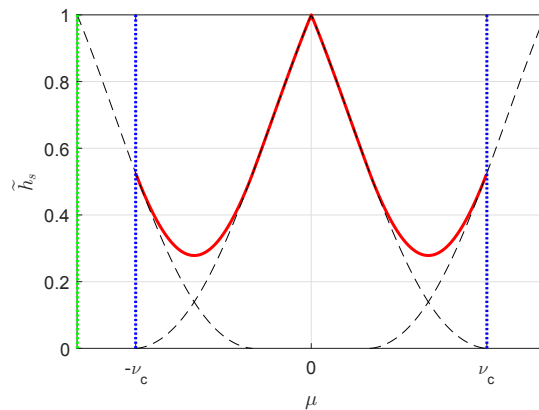


FIGURE 4.3: Sampled MTF \tilde{h}_s of an optical system where $\bar{\nu}_c = 0.75$. The red line represents the detected MTF and the black dashed lines represent the replicas. The blue dotted lines mark the cutoff frequency, while the green dotted lines mark the sampling frequency.

An example of aliasing on a one-dimensional signal is given in figure 4.4. We have plotted a sinusoidal continuous signal (in blue), the blue dots represent a sampling at twice the Nyquist frequency $\bar{\nu}_c = 0.25$ so the signal is properly sampled. The red dots on the other hand represent an undersampled system with a sampling frequency $\bar{\nu}_c = 0.75$; the dashed red line represents a cubic interpolation between the

undersampled points, which corresponds to an aliased signal of period three times larger than the original signal.

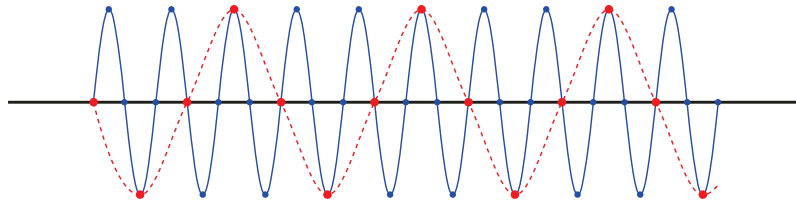


FIGURE 4.4: Aliasing of a one-dimensional sinusoidal signal. The blue line represents the continuous sinusoidal signal, the blue dots mark a sampling of $\bar{v}_c = 0.25$, the red dots mark an undersampling of $\bar{v}_c = 0.75$. The red dashed line represents a cubic interpolation of the undersampled points

Aliasing is a very common artifact in optical systems, typically seen in photography or video taken without an anti-aliasing filter. In figure 4.5 we see a typical example of an aliased image: a striped shirt. On the left we can see the image at full resolution whereas on the right we can see a simulated image with 1/5th of the resolution ($\bar{v}_c = 2.5$). We can see on the low-resolution image that on the areas where the shirt has folds, the strips of the shirt merge together and several spurious stripes appear. This effect is particularly noticeable on the right area, where curved horizontal lines appear over most of the length of the shirt.



FIGURE 4.5: Example of a scene prompt to aliasing due to sampling of $\bar{v}_c = 2.5$). On the left the properly sampled image and on the right an undersampled image suffering from aliasing

Most modern optical systems have methods to reduce aliasing; one way is to treat the continuous signal with a low-pass filter before the discretization step. In optics this would be done by modifying the pupil transmittance or in simulations with low-pass filters such as *sinc*, *Hann* or *Gaussian* filters. This actually is how most computer softwares deal with aliasing when shrinking images below their original resolution on-screen (Tucker, 2004). Another way is on the contrary to exploit the presence of aliasing using superresolution, where several low-resolution frames are combined to generate a high-resolution version of the scene. This will be studied further in section 4.2.

4.1.3 Effects of sampling on image quality

As mentioned, sampling has an effect on the MTF, such as modifying certain frequencies due to folding. Since the definitions of the MSE from equation (1.26) and the Wiener filter from equation (1.29) depend on the MTF of the system, the presence of aliasing has repercussions on the IQ value of the deconvolved image. In figure 4.6 we show the evolution of the image quality as a function of the undersampling factor $\bar{\nu}_c$ calculated for a generic scene model with $S_{OO} = \nu^{-2.5}$. The values represented by an asterisk are aliased whereas for the values represented by triangles the spatial frequencies of the scene $O(x, y)$ larger than $\nu_s/2$ have been filtered out before passing through the optical system. The values in blue, connected by dashed lines, represent sampled images deconvolved by an ideal Wiener filter. On the other hand the values in red, with continuous lines, represent sampled images without deconvolution, that is the images produced by the detector.

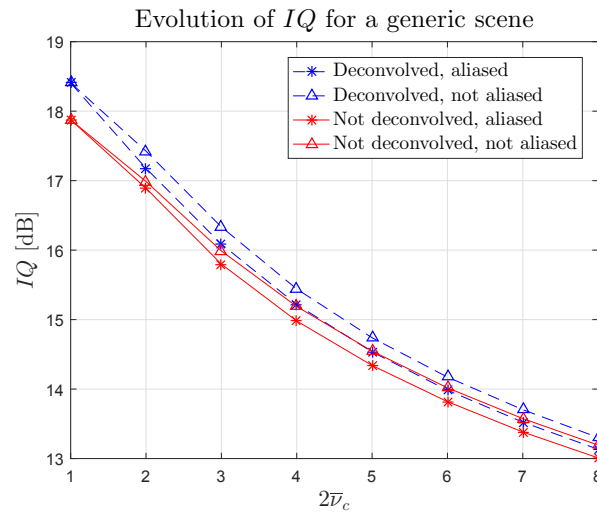


FIGURE 4.6: Evolution of the IQ of conventional systems as a function of the undersampling factor $2\bar{\nu}_c$ with deconvolution (asterisks) and without deconvolution (triangles). The red lines represent non-aliased systems whereas the blue lines represent aliased systems.

As for the phase masks, the highest impact on the IQ value comes from the loss of high frequencies, since the image quality steadily drops as the undersampling increases. The second impact comes from the presence of aliasing, in both the raw and deconvolved images, the ones with aliasing presenting a slightly lower IQ value. Finally, deconvolution by Wiener filter increases the quality of the image by practically the same amount for the aliased and non-aliased images. This last observation means that the presence of aliasing does not hinder the ability of the Wiener filter to deconvolve the images, which is vital for hybrid optical systems.

4.1.3.1 Aliasing reduction by filtering

A common problem in digital signal processing is to reduce the aliasing in a discretized signal. This is commonly achieved by filtering the continuous signal with a low-pass filter before the sampling step. When rescaling an already digitalized

image into a smaller one or when displaying an image in a screen with a lower resolution than the image itself, anti-aliasing is performed with numerical filters, as tackled below.

The simplest filter one can conceive to avoid aliasing is to multiply the Fourier transform of the high-resolution image by a box function $\Pi_{\nu_s}(\mu, \nu)$, discarding all the potentially aliased frequencies outside the box. This simple filter, or sinc filter, is not widely used in practice since it presents a ringing artifact, the well known Gibbs effect: since $\text{FT}(\Pi_{\nu_s}) = \text{sinc}(x\nu_s)$, the reverberations beyond the central lobe of the cardinal sinus are present throughout all the image, particularly on areas with sharp contrasts. Filters commonly used in the literature are the Gaussian filter, which has the advantage of being separable, so that it is simple to model analytically but leads generally to more blurred images, or the bicubic filter which does not suffer from either artifact.

In figure 4.7 is shown a resolution target, the aliased low-resolution (LR) image with $2\bar{\nu}_c = 4$ (4.7.(a)), and the LR image after filtering of the HR image by (b) a sinc filter, (c) a Gaussian filter and (d) a bicubic filter. On each case, the filter blurs out all the high-frequency details that appear aliased on 4.7.(a). As expected, the sinc filter produces ringing artifacts around high-contrast details, such as the sides of the wedge on the right. The Gaussian filter and the bicubic filter do not present these artifacts, with the Gaussian filter having some blur still present on the undersampled image.

The bicubic filter will thus be preferred for the simulation of undersampled optical systems in the following.

4.2 Superresolution

In the previous section we studied some of the consequences the discretization process has on the response of the optical system, such as aliasing. As noted earlier, in most mainstream optical systems, the optical cutoff frequency is high and the Nyquist frequency is considerably smaller, producing sharper and more visually pleasing images. In this section we will rather focus on situations where frequencies above the Nyquist frequency are to be recovered from spatially shifted low resolution frames to improve the spatial resolution closer to the diffraction limit of the optics. A simplistic 1D diagram of this principle is shown in figure 4.8, where three different samplings of the same sinusoidal signal are used to reconstruct a properly sampled signal.

4.2.1 Superresolution model

In section 4.1.2 we have seen that in sampled systems the frequencies higher than $\nu_s/2$ get cut out from the MTF, but they are still present on the MTF due to folding. In this work we define superresolution as a family of signal processing techniques that aim to take advantage of the information from the scene that is carried over due to folding to increase the resolution of an optical system and retrieve the lost spatial frequencies. It was proposed first in (Tsai and Huang, 1984) and then expanded upon by later works, see for example (Schultz and Stevenson, 1996; Hardie, Barnard, and Armstrong, 1997; Borman and Stevenson, 1998).

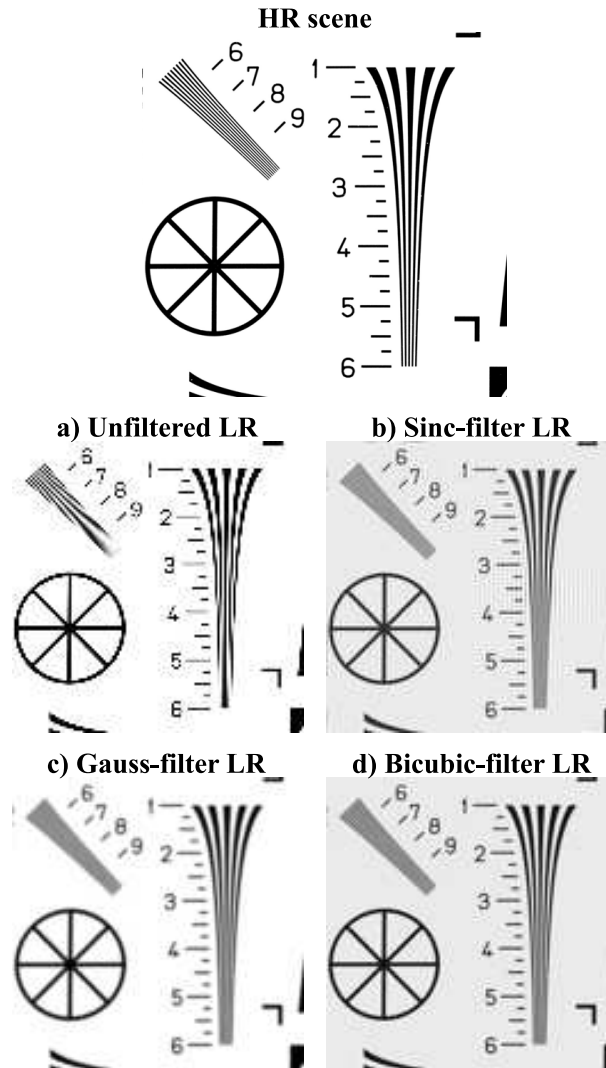


FIGURE 4.7: Resolution target used as scene (HR image), the aliased LR image with $2\bar{\nu}_c = 4$ (a), and the LR image after the scene was filtered with (b) a sinc filter, (c) a Gaussian filter and (d) a bicubic filter.

We will first start by modeling the shifted frames from the detector so that we can then model the superresolution technique. For the sake of conciseness we will write the mathematical expressions of this section only in one spatial dimension, re-indexing the pixels so that we can express them as a 1-dimensional signal, so that: $i \in \mathbb{Z}$. We can now express the value of the i th pixel of the detected image as:

$$I_i = h * O(i/\nu_s) + n_i. \quad (4.10)$$

To make the mathematical demonstrations simpler, from now onwards we will use the pixel size p as our implicit spatial unit, in this way $\nu_s = 1$ and $\bar{\nu}_c = \nu_c$, so that the undersampling factor is simply twice the optical cutoff frequency of the diffraction limited system. To be able to apply superresolution, we require a series of K frames F_k taken by the detector, each with an associated continuous shift τ_k relative to the detector:

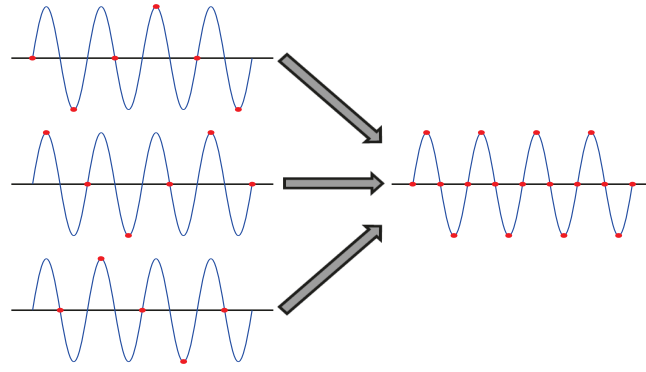


FIGURE 4.8: Diagram of the reconstruction of a well-sampled signal from several undersampled ones.

$$F_{k,i} = h * O(i - \tau_k) + n_{k,i}. \quad (4.11)$$

The values of the shifts τ_k can always be considered to take values between $0 \leq \tau_k \leq 1$, since it depends only on how the pixels were indexed in the first place. The two block diagrams shown in figures 4.9 and 4.10 are taken from (Champagnat, Le Besnerais, and Kulcsár, 2009). Figure 4.9 shows the steps of the image generation model starting from the continuous scene O to the K shifted scenes F_k .

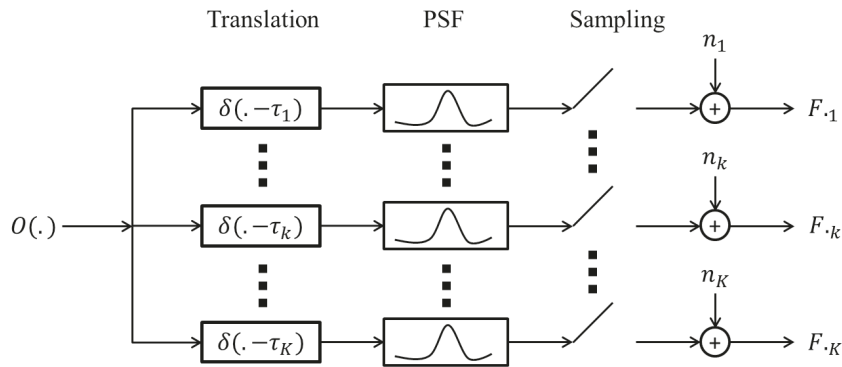


FIGURE 4.9: Block diagram modelling the generation of the K shifted low-resolution frames

In general terms, the reconstruction of the super-resolved (SR) image is a multichannel filtering, as shown by the diagram in figure 4.10.

The reconstructed image $\hat{O}(x)$ can be defined as:

$$\hat{O}(x) = \sum_i \mathbf{F}_i^T \mathbf{w}(x - i), \quad (4.12)$$

where $\mathbf{F}_i = [F_{i1}, \dots, F_{iK}]$, and $\mathbf{w}(x) = [w^1(x), \dots, w^K(x)]$ represents the filters in charge of processing each frame including shift compensation. In practice, we must define a practical magnification factor (PMF) M , that represents the relative increase in size between the LR frames and the SR reconstructed image. The value of M

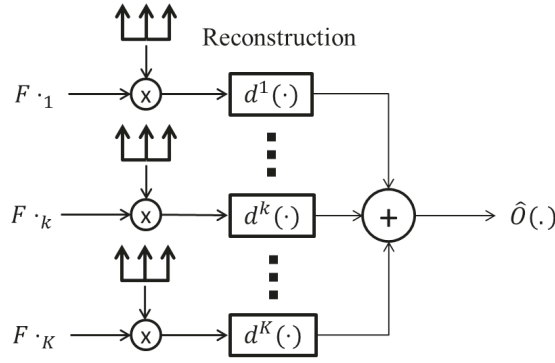


FIGURE 4.10: Block diagram of the general linear SR reconstruction with a multichannel filter

dictates how the pixels from the LR frames are allocated on the reconstructed image, so that:

$$\hat{O}(i'/M) = \sum_i \mathbf{F}_i^T \mathbf{w}(i'/M - i), \quad (4.13)$$

where $i'/M \in \mathbb{Z}$ are the pixel coordinates of the reconstructed image, so that i' is the pixel index of the SR image. This expression encompasses many linear SR reconstruction algorithms with pure translation motion, given by the definition of the multichannel filter $\mathbf{w}(i'/M - i)$. Following the same reasoning used in chapter 2 to define the DoF deconvolution filter, the optimal multichannel filter $\tilde{\mathbf{w}}_o$ that minimizes the MSE between the scene and the SR image is given, in the Fourier domain, by a Wiener filter under the form

$$\tilde{\mathbf{w}}_o(\nu) = \frac{S_{OO}(\nu) \tilde{\mathbf{h}}(\nu)^*}{S_{FF}(\nu)} \mathbf{v}_\nu, \quad (4.14)$$

where $S_{FF}(\nu) = \sum_i S_{OO}(\nu+i) |\tilde{\mathbf{h}}(\nu)|^2 \mathbf{v}_{\nu+i} \mathbf{v}_{\nu+i}^* + S_{nn} \mathbf{I}$ corresponds to the PSD of the captured frames and $\mathbf{v}_\nu = [\exp(2i\pi\nu\tau_1), \dots, \exp(2i\pi\nu\tau_K)]^T$ contains the phases produced by the shifts in the spatial domain (Champagnat, Le Besnerais, and Kulcsár, 2009).

4.2.2 Shift and add reconstruction

We will now concentrate on a simple, fast and relatively intuitive suboptimal solution for the SR problem described earlier this section, the *shift and add* (S&A) algorithm (Elad and Hel-Or, 2001). The results presented in this section come from (Champagnat, Le Besnerais, and Kulcsár, 2009). The S&A filter is a suboptimal version of the Wiener filter from equation (4.14), where the filter is separated into a two-step deconvolution:

$$\tilde{\mathbf{w}}_{SA} = \tilde{\omega}(\nu) \mathbf{v}(\nu), \quad (4.15)$$

where $\tilde{\omega}(\nu)$ is a scalar deconvolution filter. This expression of the multichannel filter has separated the shift compensation of the LR frames on one part with $\mathbf{v}(\nu)$ and the deconvolution filter on the other. The Wiener filter that minimizes the MSE between the scene and the SR image under constraint of this diagonal structure is:

$$\tilde{\omega}_o(\nu) = \frac{S_{OO}(\nu)\tilde{h}^*(\nu)}{\sum_i S_{OO}(\nu+i)|\tilde{h}(\nu+i)|^2 \frac{|\mathbf{v}_0^* \mathbf{v}_i|}{K} + S_{nn}}. \quad (4.16)$$

In practice, for the S&A method, the subpixel shifts estimated from the LR frames are projected by into the geometry of the SR image by multiplying them by the PMF and rounding to the closest integer value. Solving the MSE for $\tilde{\omega}_o(\nu)$ bounds the performance of this suboptimal approach by two cases: the lower bound is when all the shifts in the LR system are integer pixels, so that superresolution becomes simply an interpolation plus deconvolution problem, since no new information is obtained from the frames. The other boundary case is having all the subpixel shifts equispaced, which some systems achieve by having controlled shifts on the detector or the object observed (micro-scanning). In most cases, the shifts are randomly distributed, therefore, in our future simulations we will always consider the shifts as evenly distributed series of random observations.

Due to the random nature of the frame acquisition, after the SR processing some SR pixels may end up without having any LR pixel allocated, so that an inpainting algorithm has to be applied after each SR run. On the opposite, more than one LR pixel may be allocated to the same SR pixel, in this case the pixels are averaged. These two effects affect the SNR of the SR images, so that the noise prior in the Wiener filter may not coincide anymore with the noise characteristics of the image to be deconvolved. In the following, we will however consider them to be equal, in order to evaluate the performance in a simplified situation where the Wiener filter used for deconvolution does not depend on the shifts and number of frames.

4.2.3 Simulation results

We have conducted a series of simulations using the S&A plus Wiener algorithm to show its performance on a resolution target. For the Wiener filter we assume a SNR of 34dB and a generic PSD model of $S_{OO} = \nu^{-2.5}$. The images have been downsampled so that $2\bar{\nu}_C = 4$ and the PMF for the reconstruction is $M = 4$. In figure 4.11.a) we show the high resolution image of the resolution target. The numbers next to the wedges represent the number of lines per 10 pixels, so that a resolution marked as R implies $R/10$ lpp (lines per pixel). In figure 4.11.b) we can see one of the LR frames, interpolated to the size of the HR image. Aliasing begins to affect the resolution of the image at 0.375lpp, leading to a quite low IQ value.

On figure 4.11.c) we show that the image obtained with 16 equispaced LR frames; we see that the image quality has increased considerably and that the maximum resolution achieved is close to 1lpp. In 4.11.d), we show the reconstructed image from 16 LR frames with uniformly distributed random shifts. We see that the image quality is low, only 7.9dB. In the sequence, many SR pixels had no LR pixels allocated, so that inpainting was often necessary (done by interpolating the value of a pixel based on its neighbors). Regardless of this, the resolution has increased to about 0.6lpp. In 4.11.e) we processed 32 randomly shifted LR images, and we still

notice few artifacts due to inpainting. The resolution is close to 1lpp and the image quality has increased, but it is lower than for the equispaced case with 16 LR images in c). Finally, 4.11.f) shows the SR image reconstructed with 64 frames, leading to no inpainted pixels. The resolution is 1lppm and the image quality is similar to the IQ of the equispaced case. The apparent difference in contrast between the SR images comes from the ringing artifact commonly produced by the Wiener filtering, which produces pixels with values beyond and below the dynamic range of the scene. Although the dynamic range of the SR images was left as obtained, the contrast can be improved by limiting their dynamic range to the range of the LR frame.

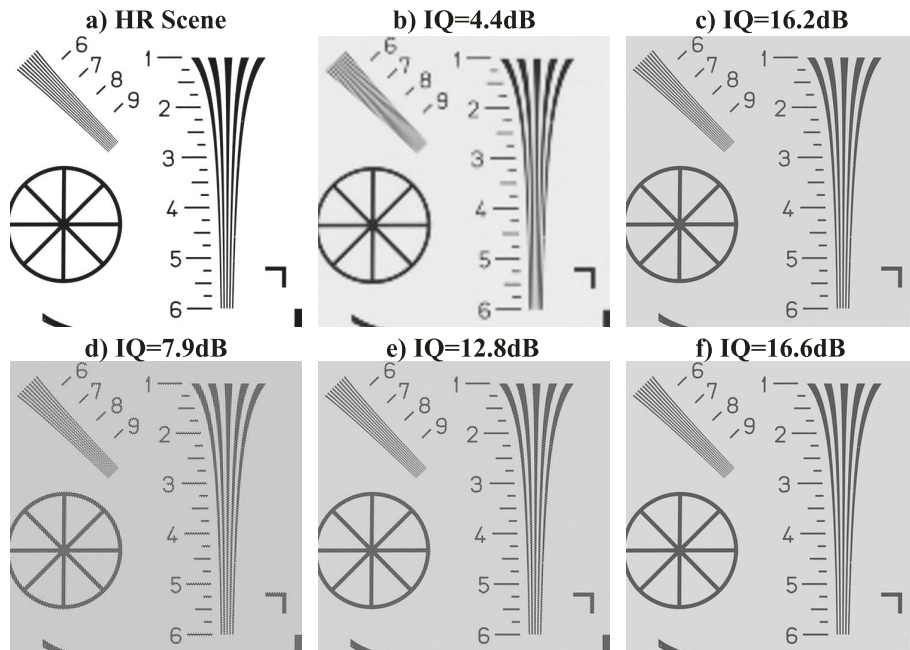


FIGURE 4.11: Simulations of superresolved images for an undersampling $2\bar{v}_c = 4$ and PMF $M = 4$. a) The high-resolution scene, b) one aliased low-res frame, c) a superresolved image with $K = 16$ known equispaced subpixel shifts d) a superresolved image with $K = 16$ known random subpixel shifts, e) a superresolved image with $K = 32$ known random subpixel shifts, f) a superresolved image with $K = 64$ known random subpixel shifts.

This shows the capabilities of the algorithm in a situation where the noise is relatively low, the shifts are known, or well estimated, and the number of frames K is high enough. The PMF of 4 leads to a rather severe rounding of the shifts, so that a higher PMF could lead to much better results if the number of frames is high enough. Also, the equispaced shifts case gives significantly better IQ values than the random shifts case. These results are globally consistent with that of (Champagnat, Le Besnerais, and Kulcsár, 2009).

4.3 Superresolution for industrial inspection

Semiconductor electronics is one of the fastest growing markets in the world, seeing a growth of 20.8% in 2017 with respect to the same trimester of the past year

(Vipress, 2017). This growth, parallel to the sophistication of semiconductor micro-components, makes it more important than ever to have a reliable and accurate way to guarantee that no faulty pieces leave the manufacturing process towards the final users' hands.

The industrial partner of this doctoral program is KLA-Tencor (Leuven, Belgium), specialized in the automation of the inspection of semiconductor microcomponents. Their optical inspection machines can observe cracks in microchip packaging molds and silicon components of few tenths of millimeters in width. But with further miniaturization of microcomponents comes the challenge of being able to observe even smaller details. In this section we explore experimentally the feasibility of applying superresolution techniques as part of the industrial inspection process.

4.3.1 Superresolution experimental setup

The experimental setup used was conceived to replicate, on an optical test bench, the conditions in which the inspection is done. The test bench is shown on figure 4.12 (left) and features an 8-bit (256 gray levels) monochromatic 25Mpx (5120×5120) ADIMEC IVC detector with a pixel pitch of $p = 4.5 \mu\text{m}$ working in the visible spectrum. The system was illuminated by a custom-made coaxial quasi-monochromatic led lamp at $\lambda = 470 \text{ nm}$. Two different lenses were used during the experiment, a $f/5.6$ lens with focal length $f = 120 \text{ mm}$, which we will for now on refer to as *system 1*, and a faster $f/4$ lens with focal length $f = 50 \text{ mm}$ which we will refer to as *system 2*. The known subpixel translations on the sample are made thanks to two ThorLabs DRV014 trapezoidal stepper motors that, according to the manufacturer, have a minimum step of 50 nm and a repeatability $< 1 \mu\text{m}$. The object size in the image plane was calculated using a caliber plate, with 2 mm inter-cross distance, shown on figure 4.12 (right).

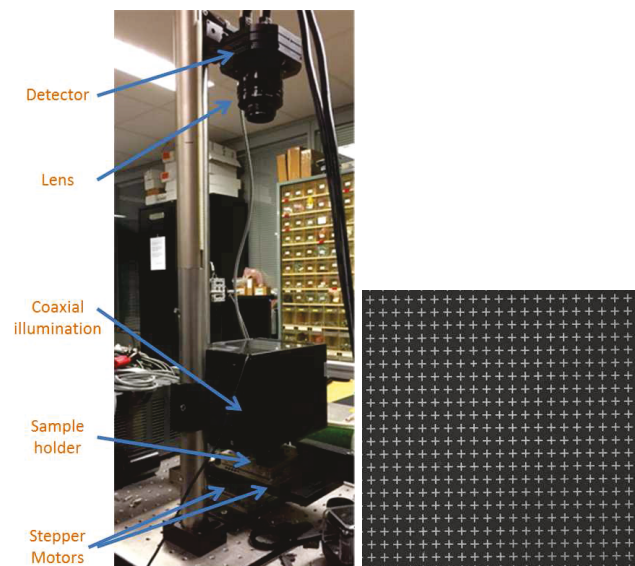


FIGURE 4.12: Setup for superresolution experiments. (Left) Experimental bench with 25Mpx detector, lens, coaxial illumination, sample holder, and two stepper motors. (Right) caliber plate used to measure the object size in the image plane.

During the calibration step we could confirm that the stepper motor specifications were reasonably correct, but throughout the experiment we observed that the repeatability of the positions was worse than $\delta\tau = 4\ \mu\text{m}$, probably due to vibrations in the room, thermal drift, etc. These problems, added to the fact that there is always an unknown angle between the camera XY axes and the dx , dy steps of the motor, imply that we cannot consider the subpixel shifts to be known. Thus a systematic estimation of the shifts via the *efficient subpixel image registration by crosscorrelation* algorithm (Guzar-Sicairos, Thurman, and Fienup, 2008) is performed.

Thanks to the caliber plate on figure 4.12 (right) we were able to calculate the spatial resolution of our systems. For system 1 we obtained a resolution of $y_1 = 8.33\ \mu\text{m}$ per pixel in the object plane, which translates to a theoretical Nyquist frequency corresponding to $\nu_1 = 60\text{lpmm}$ (lines per millimeter). On the other hand, system 2 had a resolution of $y_2 = 40.8\ \mu\text{m}$ per pixel in the object plane, so that the theoretical Nyquist frequency is $\nu_2 = 12.5\text{lpmm}$. This means that we should expect aliasing for spatial frequencies higher than those Nyquist frequencies.

For the Wiener deconvolution step we have assessed the SNR by estimating the noise levels in featureless areas of the captured images. The PSF of the system is also unknown a priori, so we have estimated it by using the approximation of the Airy pattern of a diffraction limited PSF as a Gaussian with standard deviation given by:

$$\sigma_i = 0.42(1 + m_i)N_i\lambda, \quad (4.17)$$

where $m_i = p/y_i$ is the magnification of the lens and N_i is the f -number of the lens. This means that system 1 has $\sigma_1 = 1.7\ \mu\text{m}$ and system 2 has $\sigma_2 = 0.9\ \mu\text{m}$.

4.3.2 Assessment on the resolution improvement

In general, it is difficult to evaluate the increase of quality of a real image, from a real system, beyond what we can visually assess. The problem is that, unlike for the simulations made in chapters 2 and 3, the exact values of the scene, optical system response, noise levels, etc., are difficult to obtain. Despite these limitations, carefully crafted experiments can help evaluate the response of the system (Landeau, 2014)

To assess the actual resolution of our optical systems before and after superresolution has been applied on the LR frames, we have used an Edmund Optics variable resolution target going from 5lpmm up to 120lpmm shown in figure 4.13.

For both systems, 64 frames were captured with 8×8 controlled displacements of the motors at steps of $dx = dy = 5\ \mu\text{m}$, in the understanding that the true shift differs due to the vibrations. We have estimated the standard deviation of the noise to be $\sigma_{1n} = 2.26$, and $\sigma_{2n} = 2.46$ (in gray levels), respectively. The scene model for deconvolution was set as $S_{OO} = \nu^{-2.3}$ for the frequency targets as it is the model that better fits the PSD of the resolution target along the x -axis, where most of the aliasing is observed. Due to the large size of the samples, superresolution was performed for a PMF $M = 8$, but only on an area of interest of 1000×300 pixels, along the x -axis, encompassing the theoretical Nyquist frequencies calculated for each system: $\nu_1 = 60\text{lpmm}$ for system 1 and $\nu_2 = 12.5\text{lpmm}$ for system 2). The resolution target is slightly rotated in-plane for both systems, so that the SR reconstruction is more visible.

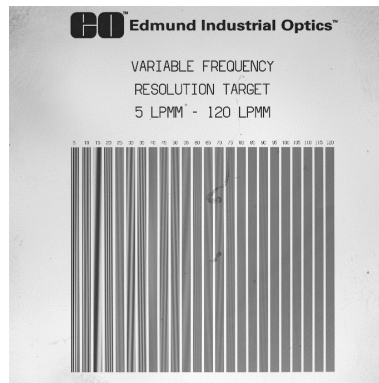


FIGURE 4.13: Variable frequency target used to measure the increase of resolution attainable by our optical systems

On figure 4.14 (top) we show two interpolated segments of the low-resolution frame captured by system 1. On the left, we see the portion between 40lpmm and 45lpmm, where we start to see aliasing. The theoretical limit calculated was originally 60lpmm, yet we see aliased lines at lower values; this is because ν_1 was calculated along the XY axes of the detector but in diagonal lines the sampling period is longer, producing aliasing at shorter spatial frequencies. On the right we show a portion of the target between 85lpmm and 90lpmm, which are aliased and blurred. After SR we are able to recover spatial frequencies up to 90lpmm, so we managed to double the resolution from 45lpmm. Beyond 90lpmm the deconvolved SR images are completely blurred. This blur can be associated to different causes, such as registration errors, the fact that the deconvolution filter was approximated based on measurements, the effect of detection noise on deconvolution or on the MTF of the pixel, that has very low values beyond the second lobe of the sinc function.

On figure 4.15(top) we show two segments of a LR frame obtained with system 2 presenting aliasing. On the left we show the portion between 10lpmm and 15lpmm. As for system 1, we see aliasing below the theoretical Nyquist frequency of $\nu_2 = 12.5$ lpmm due to the rotation of the target with respect to the detector. On the right we show the segment between 20lpmm and 25lpmm, which corresponds to the maximum observed resolution after SR has been applied. It is interesting to notice that in the LR frame, no typical aliasing patterns are noticeable for 25lpmm, yet we manage to observe the frequency details on the SR image, although with a rather poor contrast. In this case we have increased the resolution 2.5 times, from 10lpmm up to 25lpmm, 50% more than with system 1. This larger increase is due to the object pixel size: on system 2 it is $y_1 = 40.6 \mu\text{m}$, and therefore the 8×8 step motor shifts $dy \approx 5 \mu\text{m}$ are evenly spaced within a LR pixel, if we ignore vibrations of the bench. On the other hand on system 1 the object pixel size is $y_1 = 8.33 \mu\text{m}$, so that the step motor shifts are closer to the pixel size itself. These two results coincide with the performance bounds of the Wiener filter in equation 4.16 mentioned on section 4.2.2.

4.3.3 Tests on industrial samples

The industrial inspection devices that KLA-Tencor designs are conceived to detect cracks and fissures on the package or the semiconductor components themselves.

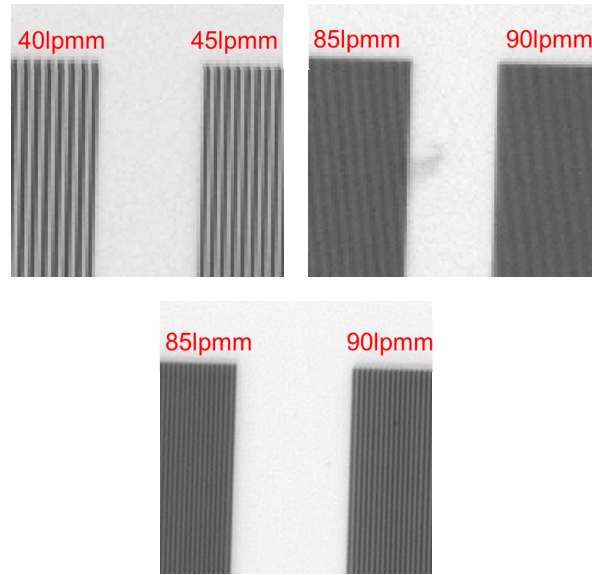


FIGURE 4.14: Test results for superresolution on system 1. (Top left) Segment of a low resolution frame showing aliasing starting between 40lpmm and 45lpmm, (top right) a segment of the LR frame between 85 and 90 lpmm. (Bottom) Segment of the superresolved frame, showing the maximum obtained resolution at 90lpmm.

This is achieved by pairing a high resolution detector with an image processing software that finds abnormal lines or patterns on the inspected surfaces and, upon confirmation, removes faulty components from the production line. The ability of the processing software to detect these cracks and fissures relies on the resolution of the optical system, which as we have seen, is undersampled and presents aliasing on very high frequencies.

4.3.3.1 Package molds

Package molds are an essential part of the semiconductors, as they protect them from impact and corrosion, disperse heat and keep the connection pins in place. To perform the superresolution tests, two packing molds were studied. The first one, P1, presenting a known crack of $\approx 11 \mu\text{m}$ at its thinnest point and the second, P2, with a known crack of $\approx 6 \mu\text{m}$ at its thinnest point. The cracks were measured with the help of an optical microscope of 100x magnification. We proceeded then to study P1 with the system 1 and P2 with system 2, since the crack of P2 was thinner than the crack of P1 and the system 2 has a lower resolution than the system 1. Once again, we captured 64 shifted frames for both systems, the PSD model for deconvolution was $S_{OO} = \nu^{-3.2}$, since this was the PSD that better fitted the PSD of the obtained frames.

The package mold P1, shown on figure 4.16 with a zoom-in of the crack, had a total area of $7\text{mm} \times 7\text{mm}$ which occupied an area on the detector of 812×812 pixels. The zoom-in shows a 145×145 pixel extract where the crack is the thinnest. We can see that although blurry and poorly resolved close to the center of the zoom-in, the crack is clearly visible even in the full-frame LR image.

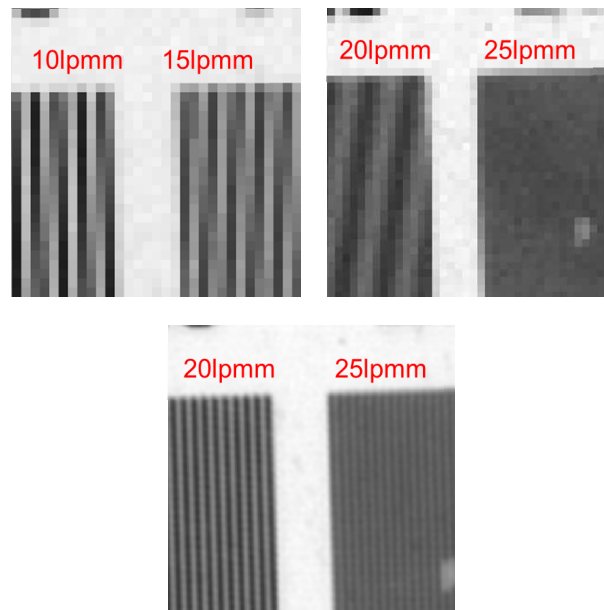


FIGURE 4.15: Test results for superresolution on system 2. (Top left) Segment of a low resolution frame showing aliasing starting between 10lpmm and 15lpmm, (top right) a segment of the LR frame between 20 and 25 lpmm. (Bottom) Segment of the superresolved frame, showing the maximum obtained resolution at 25lpmm.

We ran the superresolution algorithm on the 64 captured frames. On figure 4.17 we show the results on the same area we have zoomed-in on figure 4.16. On the left side of figure 4.17 we show the LR frames after a bicubic interpolation to resize them by PMF $M = 3$ (top) and $M = 8$ (bottom). To the right, we show the superresolved images calculated for the corresponding PMF. As we can see, for $M = 3$, the SR image is just marginally sharper than the interpolated image. On the other hand for $M = 8$ we have an important increase in contrast, sharpness and resolution. In particular, we can clearly see that at the center of the image, that the crack does not disappear, but just becomes thinner. This is consistent with the simulations from section 4.2, where we concluded that the shift and add SR technique performs better for large PMFs is, as long as there are enough frames to fill most of the SR image.

Now we pass to P2, where another packing mold of $7\text{mm} \times 7\text{mm}$ is observed through system 2, as seen in figure 4.18, along with a zoom-in around an area of interest. Since the focal length of this system is smaller than for system 1, its field of view is larger and the mold occupies an area of the detector of only 176×176 pixels. The area of interest in this case is 54×54 pixels. We can see that within the area of interest the crack is not clearly noticeable and seems rather straight.

Figure 4.19 shows the interpolated (left) and superresolved images (right). We can see that for $M = 3$, the interpolated image fails to show details on the center of the crack. On the other hand both the superresolved image for $M = 3$ and the interpolated image for $M = 8$ fully show the crack, although the superresolved image has better contrast. Finally, the superresolved image for $M = 8$ shows the sharpest image of the crack, where its width can be easily measured and we can see that is curved at some points, not just a straight line from top to bottom.

In this sample the crack is also in the LR image, as it was for P1, but it is thinner

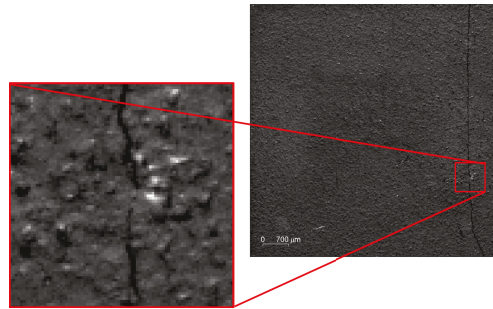


FIGURE 4.16: Cracked package mold P1 observed by system 1 and zoom-in of an area of interest

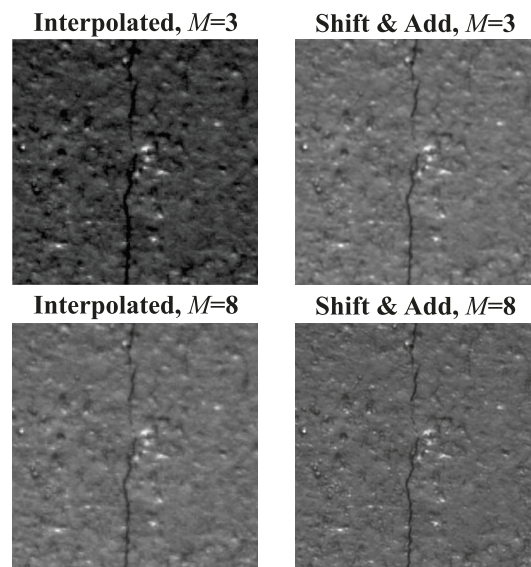


FIGURE 4.17: Sections of package 1 where a crack is visible. On the left are shown, low resolution frames interpolated by factors $M = 3$ (top) and $M = 8$ (bottom). On the right are shown the reconstructed SR images for practical magnification factors $M = 3$ (top) and $M = 8$ (bottom).

and less recognizable. The automated inspection system from KLA-Tencor discerns cracks from harmless scratches by distinguishing between their shapes. Scratches are mostly straight and thin while cracks are thicker and curvy. In this case the crack is so thin that it may be overlooked by the inspection machine, which could be prevented by superresolution.

4.3.3.2 Silicon microcomponent

The last sample studied is a silicon microcomponent of $7\text{mm} \times 7\text{mm}$ with a known crack of width $< 1\ \mu\text{m}$. Silicon components are different from the packing molds in that their surface is highly reflective, not rugged black, which makes searching for fine cracks a complicated yet interesting problem. In most cases the system is illuminated at a low angle, so the light scattered by the crack can be observed. This interesting solution has the drawback of requiring a different setup to study silicon

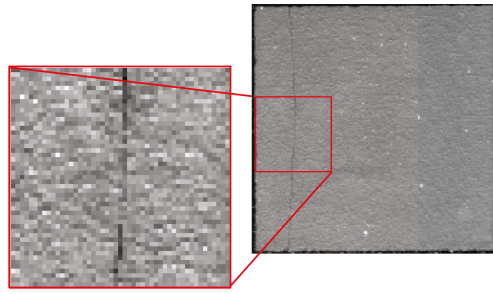


FIGURE 4.18: Cracked package mold P2 observed by system 2 and zoom-in of an area of interest

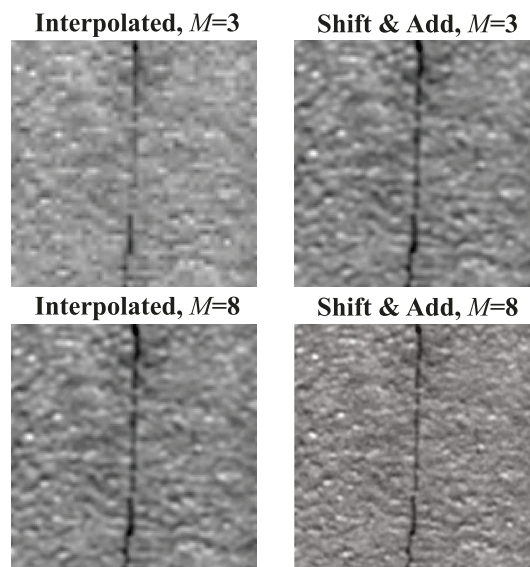


FIGURE 4.19: Sections of package 2 where a crack is visible. On the left are shown, low resolution frames interpolated by factors $M = 3$ (top) and $M = 8$ (bottom). On the right are shown the reconstructed SR images for practical magnification factors $M = 3$ (top) and $M = 8$ (bottom).

components from the packing molds, which increases the complexity, and the price, of the inspection equipment. For this component we used system 1, since it has the highest resolution.

In figure 4.20 we show the silicon microcomponent, occupying 786×784 pixels and the area of interest, which does not seem to show any features other than detection noise.

In figure 4.21 we show the processed images of the area of interest. We see that neither of the interpolated LR frames show the crack, there is just a slightly darker zone close to the left edge of the frame. The superresolved images on the other hand manage to show parts of the crack in both instances, being sharper for $M = 8$ but more contrasted for $M = 3$. This difference in contrast is likely to be related to the noise level; for lower PMF values, more LR pixels get averaged into one SR pixel, considerably reducing the noise on each of those pixels and increasing the overall contrast.

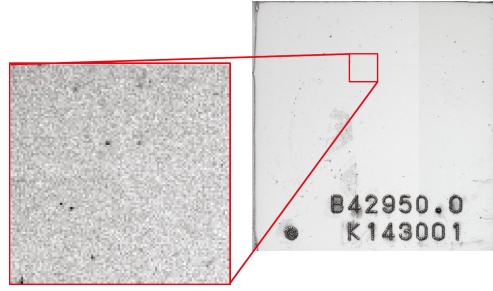


FIGURE 4.20: Silicon microcomponent observed by system 1 and zoom-in of an area of interest

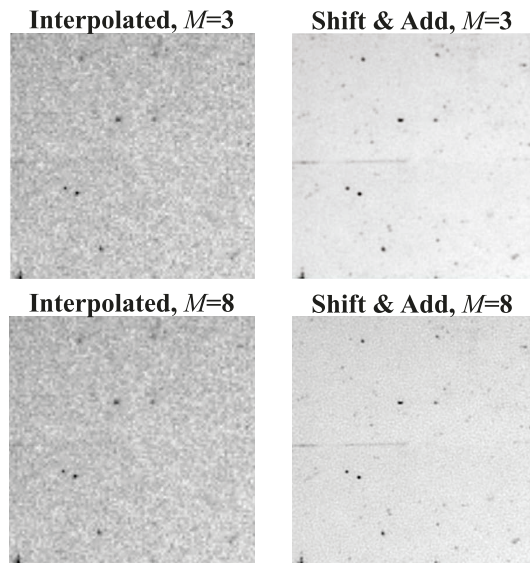


FIGURE 4.21: Sections of interest of the silicon microcomponent. On the left are shown, low resolution frames interpolated by factors $M = 3$ (top) and $M = 8$ (bottom). On the right are shown the reconstructed SR images for practical magnification factors $M = 3$ (top) and $M = 8$ (bottom).

4.4 Phase masks for Dof extension and superresolution

In the previous section we have shown the perks and limitations of the *shift and add* technique for industrial inspection. From the two systems studied the one with the shorter focal length, $f_2 = 50$ mm, has a larger field of view but less spatial resolution, so it would benefit more from superresolution. According to equation (1.9) shorter focal lengths also imply shallower DoFs, this opens up the question of the possibility of DoF extension and superresolution used together. In this section we explore this concept, study its limitations and the cases where it would be relevant.

4.4.1 Effects of the pixel size on the depth of field

As we have discussed in chapter 2, optical aberrations are produced by phase deviations of the wavefront in the pupil, these deviations cause the PSF to deform and,

usually, widen. This is the case as well for defocus, which we can use alongside paraxial optics to describe the DoF. Consider the optical system in figure 4.22, where we have represented the point in the scene A which is on-focus, and the points B and C which are at the edges of the DoF, so that $\psi \in [\psi_B, \psi_C]$.

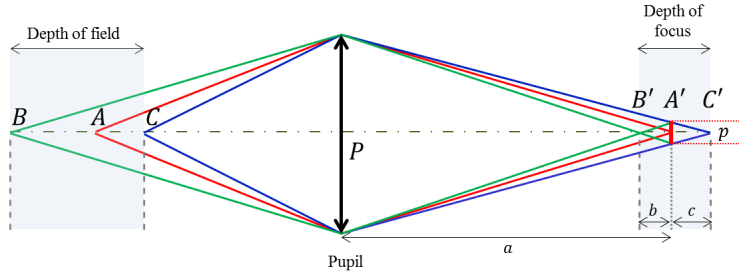


FIGURE 4.22: Paraxial optics diagram showcasing the dependency of the DoF on the pixel size

In chapter 1 we have shown the paraxial DoF equation (1.9) for a diffraction limited system. By substituting the notation from the diagram in figure 4.22 on equation (1.9) we can describe the defocus on the points B and C :

$$\psi_B = \frac{\pi R^2}{\lambda} \left(\frac{1}{BP} + \frac{1}{a} - \frac{1}{f} \right) = \frac{\pi R^2}{\lambda} \left(\frac{1}{a} - \frac{1}{a-b} \right), \quad (4.18)$$

$$\psi_C = \frac{\pi R^2}{\lambda} \left(\frac{1}{CP} + \frac{1}{a} - \frac{1}{f} \right) = \frac{\pi R^2}{\lambda} \left(\frac{1}{a} - \frac{1}{a+c} \right), \quad (4.19)$$

where R is the pupil radius, the left hand part of the equation was calculated from the paraxial optics property $(AP)^{-1} + (A'P)^{-1} = f^{-1}$ and the relations between the distances a , b and c . Now if we use the similar triangle theorem to prove that:

$$b = \frac{ap}{2R + p},$$

$$c = \frac{ap}{2R - p},$$

we can use equations (4.18) and (4.19) to calculate the DoF solely as a function of the pixel size p , the distance a and the pupil radius R :

$$\text{DoF} = \psi_C - \psi_B = \left[\frac{\pi R p}{2\lambda a} \right] - \left[-\frac{\pi R p}{2\lambda a} \right] = \frac{\pi R p}{\lambda a}. \quad (4.20)$$

In equation (4.20) we see that the DoF is directly proportional to the pixel size p , therefore an increase of the pixel size of $2\bar{\nu}_c$ times would increase the nominal DoF of a conventional system by the same amount.

4.4.2 Aliasing on phase masks

As has been mentioned in chapter 3, most phase masks behave as low-pass filters when introduced in the optical system. Since the cutoff frequency of these masks is lower than the nominal cutoff frequency of the diffraction limited system, introducing a BAPM or a QPM on the system's pupil would reduce the value of $\bar{\nu}_c$, potentially eliminating alias from the detected scene. As in chapters 2 and 3, we define the cutoff frequency of a phase mask, ν_c^{PM} , as the first zero-valued point of the MTF. On table 4.1 we show the cutoff frequencies of the optimal BAPMs reported in chapters 2 and 3, the cutoff frequencies shown correspond to the lowest cutoff frequency among the $\psi_k = \{0, \dots, \psi_{\max}\}$ evaluation points used to calculate the Wiener filter. The values of ν_c^{PM} shown are normalized with respect to the cutoff frequency of a diffraction limited system of the same aperture.

TABLE 4.1: Cutoff frequency of BAPMs ν_c^{PM} , normalized with respect to the diffraction limited cutoff frequency ν_c , optimized for DoF $\psi_{\max} = 0.75, 1.0, 1.5, 2.0, 2.5, 3.0$, column 2 shows the number of rings of each optimal mask

$\psi_{\max}[\lambda]$	N rings	ν_c^{PM}/ν_c
0.75	3	0.70
1.00	4	0.65
1.50	5	0.59
2.00	6	0.51
2.50	7	0.46
3.00	6	0.47

As we can see, all masks would lead to aliased images if the undersampling factor of the diffraction limited system satisfies

$$\frac{\nu_c^{PM}}{\nu_s} > 0.5, \quad (4.21)$$

which is true in most modern optical systems, so that phase masks could be introduced in such systems to assess the performance of SR combined with DoF extension. These masks could then be used without modification since, as shown in chapter 2, BAPMs are robust to the small amounts of aberrations that would be present in commercial optical systems. For example, according to the expression for the diffraction limited cutoff frequency: $\nu_c = (\lambda N)^{-1}$, we can approximate the undersampling factor of the systems presented in section 4.3 to be $\bar{\nu}_{1c} = 1.7$ and $\bar{\nu}_{2c} = 2.4$. Since $\nu_c^{PM}/\nu_s = (\nu_c^{PM}/\nu_c) \cdot \bar{\nu}_c$, and using the values of ν_c^{PM}/ν_c provided in table 4.1, we see that all the optimized BAPMs satisfy equation (4.21) in both systems.

4.4.3 Superresolution and DoF extension

We have established the conditions an optical system should satisfy so that systems with phase masks produce aliased images. In this section we make use of this information to simulate a hybrid optical system for DoF extension and superresolution. In figure 4.23 we show the deconvolved images from two optical systems aliased with an undersampling factor of $2\bar{\nu}_c = 4$, one having a 5-ring mask optimized for

$\psi_{\max} = 1.5\lambda$ (top) and the other having a 6-ring mask optimized for $\psi_{\max} = 3.0\lambda$ (bottom) at defocus points $\psi = \{0, \psi_{\max}/2, \psi_{\max}\}$. In all cases, the images were upscaled by bicubic interpolation to the size of the HR scene to calculate IQ . We can observe aliasing in both images from 0.375lpp, just like the conventional maskless system from figure 4.11.

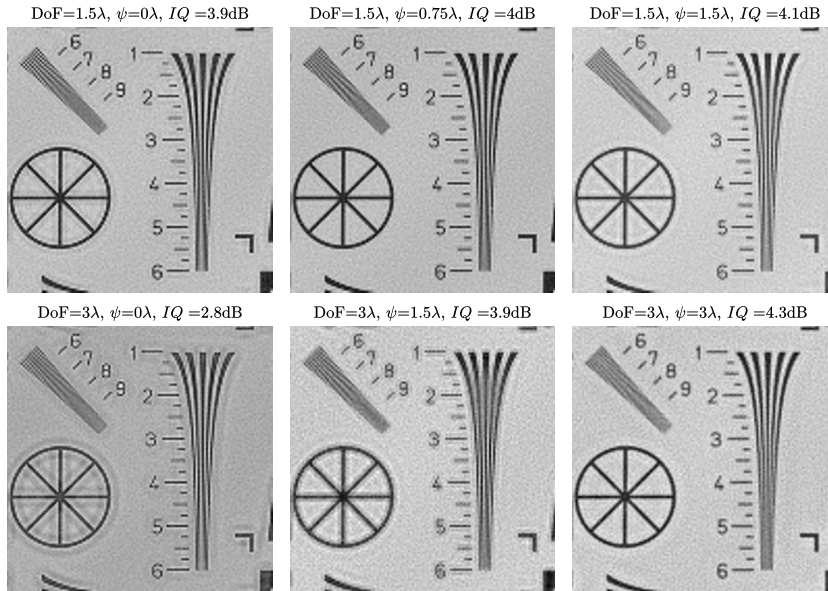


FIGURE 4.23: Deconvolved images from an aliased optical system with $\bar{\nu}_c = 2$ and BAPMs optimized for (top) $\psi_{\max} = 1.5\lambda$ and (bottom) $\psi_{\max} = 3.0\lambda$. The images show the defocus points $\psi = \{0, \psi_{\max}/2, \psi_{\max}\}$. The frames shown were interpolated to the size of the HR scene for comparison.

For the superresolution simulations we use again the shift and add algorithm. We simulated 16 LR frames with known equispaced subpixel shifts, a SNR=34dB and an undersampling factor $2\bar{\nu}_c = 4$. We have chosen the equispaced case since every LR pixel is allocated only once on each SR pixel, providing the same SNR for the SR grid, before deconvolution, than for the LR frames.

For the deconvolution we use the Wiener filter defined in equation (4.15) for shift and add, but we substitute the OTF of the conventional optical system \tilde{h} for the averaged OTF $\sum_k \tilde{h}_{\psi_k}$ that appears in the averaged Wiener filter for DoF extension in equation (1.29).

On figure 4.24 we show the images produced by the superresolution and DoF extension model we have just described. We can see that in all cases, we have doubled the resolution, going from 0.375lpp in the LR frames up to, at least, 0.75lpmm in the SR image. This increase in resolution has a clear effect on the values of IQ , which increased considerably compared to the deconvolved LR frames..

In the zoom-ins we can appreciate that the system with the 5-ring mask optimized for $\psi_{\max} = 1.5\lambda$ has its lowest resolution at $\psi = 0$, of value 0.8lpp, and its best resolution at $\psi = 1.5\lambda$, of value 0.95lpp, which is consistent with the MTFs we have shown on figure 3.19, where this BAPM has the same value of ν_c^{PM} for $\psi = 0$ and $\psi = 0.75\lambda$ and higher ν_c^{PM} for $\psi = 1.5\lambda$. The IQ values we see are related to the artifacts we observe in the images; the reconstructed images for $\psi = 0$ and $\psi =$

1.5λ have $IQ = 12.2\text{dB}$, and they also have a strong ringing around high frequency details. On the other hand, the image for $\psi = 0.75\lambda$ has $IQ = 13.2\text{dB}$ and presents almost no ringing.

Similar observations can be made for the 6-ring mask optimized for $\psi_{\max} = 3.0\lambda$. Its best resolution, of value 0.85lpp , is seen at $\psi = 3\lambda$, whereas the other two defocus points have a resolution of 0.75lpp . The image qualities vary less than for the mask optimized for $\psi_{\max} = 1.5\lambda$, but we still see that the stronger the ringing, the lower the IQ value is.

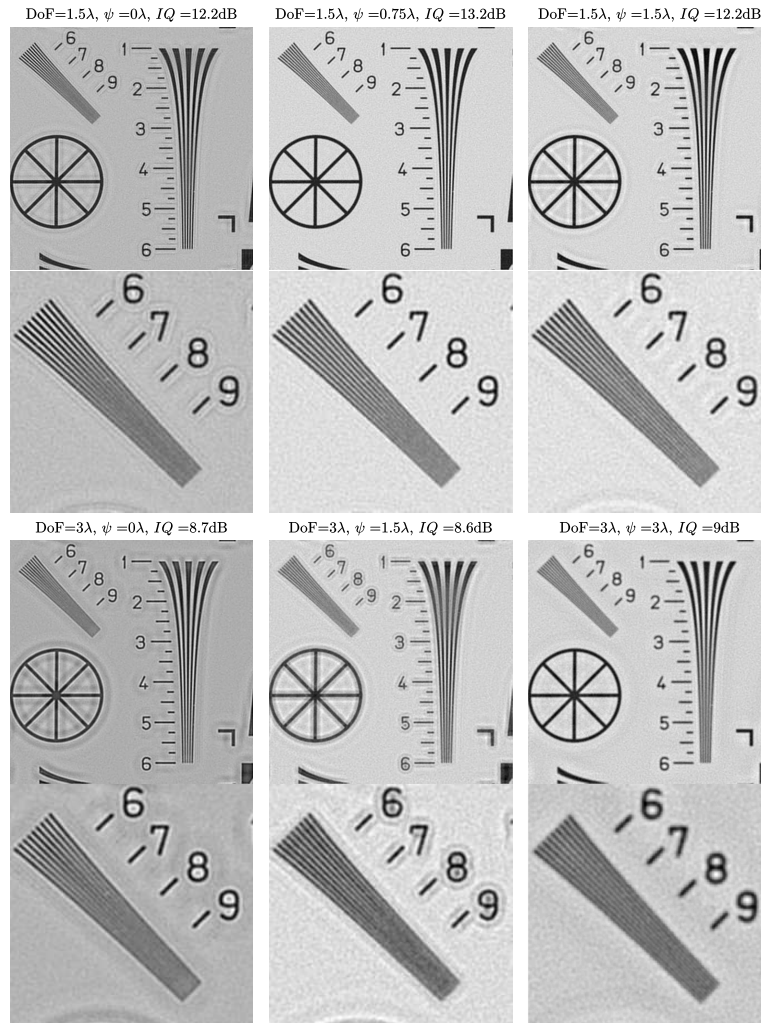


FIGURE 4.24: Deconvolved images, and detail of the high frequency resolution wedge, from superresolved images with BAPMs optimized for (top) $\psi_{\max} = 1.5\lambda$ and (bottom) $\psi_{\max} = 3.0\lambda$. The images show the defocus points $\psi = \{0, \psi_{\max}/2, \psi_{\max}\}$.

The artifacts we see in many of the images, and particularly the ringing and the noise amplification are a consequence of deconvolution on this type of scene, indeed, binary images, with very sharp black and white transitions between their elements tend to produce ringing artifacts upon deconvolution in systems without or with phase masks. We have shown that, in an equispaced subpixel shift scenario, phase

masks are capable of extending the depth of field of SR system as long as the condition $\nu_c^{PM}/\nu_s > 0.5$ is satisfied.

4.5 Conclusions

In this chapter we introduced the concept of undersampling and its main repercussion in the captured image, aliasing. We have defined the consequences of aliasing and the different ways it is tackled, either by preventing it through low-pass filters or exploiting it to achieve superresolution. A superresolution algorithm has been implemented, and tested through the shift and add method.

We have used this scheme to prove the feasibility of using superresolution in industrial inspection of microcomponents thanks to our cooperation with the enterprise KLA-Tencor. We have proven that, without changing the current optical systems the company uses, it is possible to double their spatial resolution and detect defects on the components that were undetectable before. These results have been obtained with the simple S&A algorithm and a suboptimal deconvolution filter; this means that a dedicated algorithm tailored for their needs could bring faster computation times using an optimized implementation and even better resolutions than what our feasibility experiment achieved.

The S&A algorithm also allowed us to prove for the first time, to the best of our knowledge, that BAPMs are a viable option to perform both DoF extension and superresolution with a single hybrid optical system. Although phase masks are typically considered low-pass filters and thus not adapted to superresolution, most modern optical systems have an undersampling large enough to allow DoF extension without sacrificing the possibility of superresolving such system. The reachable increase of resolution is restricted to the inherent cutoff frequency of the phase mask and the right management of the noise, so for a given application, the mask and the Wiener filter should be jointly optimized through a criterion that accounts for the SR processing as well.

General conclusions

In this work we have made a thorough study of the co-design, performance and applications of phase masks for depth of field extension (Dowski and Cathey, 1995), (Cathey and Dowski, 2002), (Robinson and Stork, 2007). We have used a rigorous mathematical model for the joint optimization that considers both the phase mask and the Wiener deconvolution filter. We have chosen the so-called image quality (Diaz, 2011) to evaluate the performance of the co-designed system. For optimizations, our performance criterion, IQ_{\min} , is the minimal value of IQ within the desired DoF.

The phase mask we chose to co-optimize is the binary annular phase mask, consisting of N concentric rings of optical path difference modulation 0 or λ . These masks feature several interesting properties, such as a circularly symmetric PSF spot, the same performance around the point of best focus and a relatively easy to manufacture profile. We have shown that the co-optimization of binary annular phase masks, in terms of the image quality, is a complicated endeavor, since its solution landscape is highly nonconvex and non-derivable at all points. We have decided to optimize the masks using the particle swarm global optimization algorithm, which probes many areas of the optimization landscape simultaneously, akin to having several optimizations running simultaneously.

For the joint optimization of the masks we have supposed a generic scene model. We have successfully co-optimized BAPMs with increasing number of rings for DoF ranges from 4 to 12 times larger than in a conventional diffraction limited system. We show that for a given DoF the value of IQ_{opt} of the optimal masks increases rapidly with the number of rings and levels-off at a certain amount of rings (Falc3n, Kulcsar, and Goudail, 2016). On the other hand, for a given number of rings, the value of IQ_{opt} decreases as the DoF increases, so that the performance of BAPMs for DoF extension is bounded. We also show that this behavior is robust when the scene changes, when aberrations are present and even when the masks are optimized using different priors for the scene model (Falc3n et al., 2017).

We have shown that other common performance criteria in traditional optical design, such as the Strehl ratio and the invariability of the modulation transfer function are not adapted for co-design, since they do not account for the deconvolution step. In particular, the MTF used in conjunction with the deconvolution filter can give insight on the mask performance, but its interpretation is more complex than the image quality.

The methodology for optimization and analysis used for the BAPMs was applied to other phase masks found in the literature such as the polynomial-profile phase mask, aspheric-profile phase masks and a circularly symmetric mask with a free-form generatrix. We have found that in the context of DoF extension, the aspheric phase masks do not perform as well as the others, since they have a narrower DoF. The polynomial phase masks show a slightly lower performance than the free-form

masks and BAPMs at low DoF ranges and a performance very similar to BAPMs at higher DoF. The optimal free-form had a performance similar to BAPM at low DoF but a lower performance at high DoF. Interestingly, the optimized freeform masks had a profile that resembles a BAPM, as its continuous profile shows sharp changes of phase modulation.

Throughout this manuscript the relation between the phase masks frequency response and the final performance has been evidenced. Due to the scene model we have chosen, the value of the MTF at low frequencies influences the final image quality value much more than at high frequencies. For this reason, optimal masks tend to have a very pronounced cutoff frequency and a Wiener filter that amplifies only the frequencies lower than the cutoff. Due to this dynamic of the phase masks, they are usually considered to perform as low-pass filters. This raises the question whether DoF extension could be used in conjunction with superresolution, an image processing technique that exploits the presence of folded high frequencies in a sequence of low resolution images in order to improve the resolution.

Superresolution is only possible when the Nyquist frequency of the detector is lower than the cutoff frequency of the optical system, producing an effect called aliasing. In collaboration with our industrial partner, KLA-Tencor, we have implemented the well known shift and add SR algorithm (Elad and Hel-Or, 2001) and tested it in both simulated low-resolution frames and in a laboratory setup. We have shown that SR is efficient in industrial inspection, doubling the resolution of two of the company's optical systems on which the experiments were conducted, and allowing the clear detection of defects in electronic microcomponents.

We have also shown that aliasing in the captured images does not affect gain brought by the deconvolution step, a critical part in DoF extension with phase masks. We have demonstrated that all the BAPMs we have optimized have a cutoff frequency high enough to permit superresolution to be used. We show with simulations that it is advantageous to perform the shift and add technique on raw image sequences from a system with a BAPM, using a deconvolution filter adapted to the phase mask.

The optimization and analysis tools in this manuscript are of great interest for an optical engineer in order to make informed decisions when co-designing a system for DoF extension before proceeding to the test bench.

Perspectives

Throughout this manuscript we have studied binary annular phase masks optimized solely for depth of field extension and proved them robust in situations they were not optimized for, such as the presence of residual aberrations, different scenes or even using them alongside superresolution. This raises the question: how much would the performance increase if these conditions were considered in the optimization.

Some works have shown that phase masks can be used to simultaneously extend the DoF and mitigate optical aberrations (Ojeda-Castañeda, Andres, and Diaz, 1986), (Mezouari and Harvey, 2002), (Prasad et al., 2004). It could be of interest to use the performance criterion presented in this work for co-optimization of system presenting aberrations and compare them to the masks in this work in terms of criteria such as performance, number of necessary parameters or robustness to other aberrations.

In this work we have used different tools to compare the performance of five different optimized masks. Many other masks for DoF extension exist in the literature, (Sauceda and Ojeda-Castañeda, 2004), (Sherif, Cathey, and Dowski, 2004), (Yang, Liu, and Sun, 2007), and works comparing these masks usually include only a handful of them (Hu et al., 2013). An analysis and comparison methodology such as the one presented in chapters 2 and 3 on other phase mask profiles would be of interest. Such a comparison has been done in the context of the image quality (Diaz, 2011), but restricted to the optimization criterion and not other analysis methodologies, such as the impulse response, robustness to scene model or robustness to aberrations. These analyses can be useful to discriminate which type of phase mask is more adapted to a given optical design problem.

We have shown, for the first time to our knowledge, the potential of phase masks for DoF extension to be used in conjunction with superresolution. This has been done using shift and add, one of the simplest SR algorithms in the literature, with a suboptimal Wiener filter and a phase mask that was not optimized for this purpose. The proof of concept we have done could also be expanded upon, with a phase mask and a postprocessing co-optimized for the purpose of DoF extension of super-resolved systems. For this optimization, not only the quality of the images would be of concern, but also the resolution improvement, so the research for a suitable optimization criterion is necessary.

Most of the results shown in this manuscript are the product of simulated systems. The logical next step is to experimentally validate these results. Binary annular phase masks optimized for different DoF ranges and number of rings would need to be manufactured and compared in a laboratory setting with well sampled detector. The scene for the experiment has to include different depths, so an on-focus maskless camera has to present blur on the out-of-focus elements of the scene. At the moment of this publication, a number of BAPMs that we consider of scientific interest have been selected for manufacture and the experimental set up is already being designed. For the validation of superresolution, these masks would have to be included in an undersampled system, with a scene that has frequency targets at different out-of-focus points. We can then observe the change of resolution after deconvolution at different focal distances. These two experimental setups can help us draw a link between the modeled performance and the one experimentally obtained.

Résumé de la these

Co-conception des systèmes optiques avec masques de phase pour l'augmentation de la profondeur du champ : évaluation de la performance et contribution de la super-résolution.

Depuis le début de l'ère numérique, la conception des systèmes optiques a progressé considérablement avec l'apparition de logiciels capables d'optimiser des systèmes complexes impossibles à modéliser analytiquement. D'autre part, les progrès des moyens de calcul ont conduit à l'utilisation, dans les systèmes optiques, d'algorithmes de traitement d'image conçus pour améliorer la qualité des images, augmenter l'information qu'on peut en extraire ou simplement les rendre plus agréables visuellement. Dans cette thèse, on utilise un modèle de co-conception optique, où sont optimisés de manière conjointe les paramètres du système optique et du processus de traitement d'image pour obtenir la meilleure qualité d'image possible.

Masques de phase pour l'augmentation de la profondeur du champ

Les masques de phase sont des dispositifs réfractifs situés généralement au niveau de la pupille d'un système optique pour en modifier la réponse impulsionnelle (PSF en anglais), par une technique connue sous le nom de codage de front d'onde. Ces masques sont mis dans la pupille des systèmes d'imagerie pour corriger des aberrations, athermaliser ou, dans le cas qu'on étudie, augmenter la profondeur du champ (DoF en anglais) sans diminuer la quantité de lumière qui entre dans le système. L'utilisation des masques de phase pour l'augmentation du DoF a été proposée pour la première fois par (Dowski and Cathey, 1995), où ils utilisent un masque de phase cubique pour générer une PSF ayant une plus grande invariance à la défocalisation. Cependant, plus le DoF est grand et plus l'image acquise est floue, et une opération de déconvolution doit alors lui être appliquée (Cathey and Dowski, 2002). Par conséquent, la conception des masques de phase doit prendre en compte ce traitement pour atteindre le compromis optimal entre invariance de la PSF à la défocalisation et qualité de la déconvolution (Robinson and Stork, 2007; Diaz et al., 2009).

Le système d'imagerie hybride que l'on considère dans cette thèse consiste en une lentille idéale, un masque de phase placé dans la pupille du système optique et un filtre de déconvolution numérique qui traite l'image obtenue par le capteur. Dans cette étude, on considère une plage spectrale quasi-monochromatique proche de la

fréquence nominale λ . L'image produite $\widehat{O}(r)$ par ce système optique peut être modélisée par :

$$\widehat{O}(r) = d(r) * [h_{\psi}^{\varphi}(r) * O(r) + n(r)], \quad (4.22)$$

où $O(r)$ est la scène nette de moyenne nulle, $*$ représente l'opérateur de convolution, h_{ψ}^{φ} est la PSF du système optique, $n(r)$ est le bruit de détection, $d(r)$ représente le filtre de déconvolution et r représente les coordonnées spatiales. On suppose que la lentille a une ouverture de rayon R , la réponse impulsionnelle h_{ψ}^{φ} est une fonction des paramètres du masque de phase φ et du déphasage dans la pupille par délocalisation ψ . Pour évaluer la qualité d'image produite par le système optique, on utilise l'écart quadratique moyen (MSE en anglais) entre l'image traitée et l'image nette (Diaz et al., 2009) :

$$MSE(\varphi, \psi) = \mathbb{E} \left[\int |\widehat{O}(r) - O(r)|^2 dr \right], \quad (4.23)$$

où $\mathbb{E}[\cdot]$ représente l'espérance mathématique. Le bruit $n(r)$ et l'image nette $O(r)$ sont supposés être des processus stationnaires de moyenne nulle. Ce critère est capable de prendre en compte à la fois le flou de l'image finale $\widehat{O}(r)$ et l'amplification du bruit produite par la déconvolution, qui doivent être minimisés et équilibrés de manière simultanée par l'optimisation pour garantir une bonne qualité d'image finale. Pour optimiser le système optique, on minimise le MSE sur une DoF donnée par un ensemble de K valeurs de $\psi = \{\psi_1, \psi_2, \dots, \psi_K\}$, la valeur maximale de la DoF est notée ψ_{\max} avec $|\psi_k| \leq |\psi_K| = \psi_{\max}$. Donc, le filtre moyen de Wiener $\tilde{d}_{\psi}^{\varphi}$ qui minimise $\sum_k MSE(\varphi, \psi)$ a pour expression en Fourier :

$$\tilde{d}_{\psi}^{\varphi}(\nu) = \frac{\frac{1}{K} \sum_k (\tilde{h}_{\psi_k}^{\varphi}(\nu))^*}{\frac{1}{K} \sum_{k=1}^K |\tilde{h}_{\psi_k}^{\varphi}(\nu)|^2 + \frac{S_{nn}(\nu)}{S_{oo}(\nu)}}, \quad (4.24)$$

où $*$ représente la conjugaison complexe. Dans cette thèse, on utilise la « qualité d'image » (IQ), une quantité plus pratique définie par :

$$IQ(\varphi, \psi) = 10 \log_{10} \left(\frac{E_O}{MSE(\varphi, \psi)} \right), \quad (4.25)$$

où E_O est l'énergie de la scène définie par $E_O = \int |O(r) - \mathbb{E}[O(r)]|^2 dr$. On peut donc définir le critère d'optimisation en termes de qualité d'image :

$$IQ_{\min}(\varphi) = \frac{E_O}{MSE_{\max}(\varphi)}, \quad (4.26)$$

où $MSE_{\max}(\varphi) = \max_k [MSE(\varphi, \psi_k)]$. Donc, le profil du masque optimal peut être écrit comme :

$$\varphi_{\text{opt}} = \arg \max_{\varphi} [IQ_{\min}(\varphi)]. \quad (4.27)$$

On peut alors définir la qualité d'image optimale comme :

$$IQ_{\text{opt}} = IQ_{\min}(\varphi_{\text{opt}}), \quad (4.28)$$

qui est un critère qui maximise la qualité d'image la plus basse dans la plage de défocalisation. Le diagramme représenté dans la figure 4.25 montre les étapes nécessaires pour l'optimisation conjointe du masque de phase et du filtre de déconvolution.

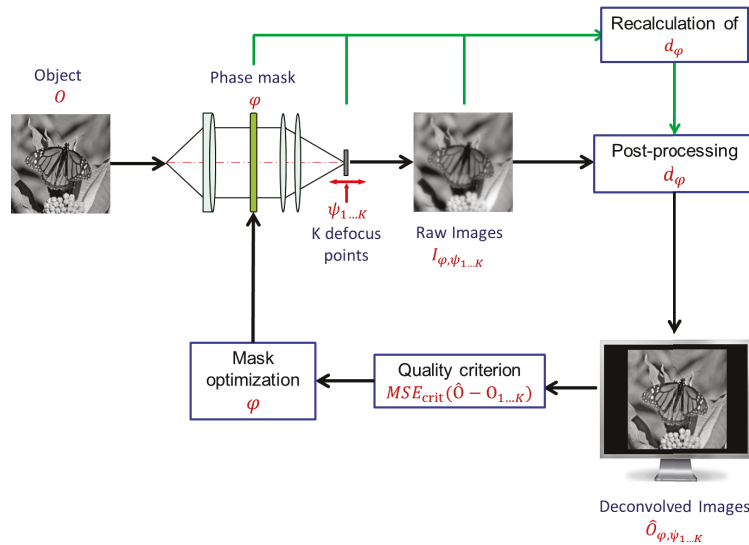


FIGURE 4.25: Diagramme de co-conception optique, marquant les étapes nécessaires pour optimiser conjointement le masque et le filtre de déconvolution

Limites des masques de phase pour l'augmentation de la DoF

Dans la littérature ont été proposés plusieurs types de profils de masques de phase pour l'augmentation de la profondeur de champ : les masques polynomiaux, qui peuvent être modélisés mathématiquement, les masques quartiques qui compensent aussi quelques aberrations. Dans la première partie de la thèse, on se concentre sur les masques annulaires binaires (BAPM en anglais), qui possèdent des caractéristiques intéressantes, comme une PSF symétrique autour du point $\psi = 0$, une tache de PSF circulaire et le fait de pouvoir les fabriquer relativement facilement. Les BAPM consistent en N régions annulaires concentriques de modulation de phase 0 ou π en alternance. Chaque région annulaire correspond à un anneau, de sorte qu'un masque avec N anneaux est paramétré par $N - 1$ valeurs normalisées de rayons $\varphi = \{\rho_1, \dots, \rho_{N-1}\}$ où la i ème transition de phase se place à $r_i = \rho_i R$ et satisfait la condition $0 < \rho_1 < \dots < \rho_{N-1} = 1$ (voir Fig.4.26).

Le problème d'optimisation de ces multiples paramètres est très compliqué, particulièrement pour des BAPM, car le paysage d'optimisation contient plusieurs maxima locaux avec des valeurs très similaires. Pour cette raison on utilise un algorithme d'optimisation globale appelé, en anglais, *particle swarm*, où un *essaim* de particules sonde le paysage d'optimisation en cherchant le point optimal. Pour les optimisations sont considérés : un modèle de scène $S_{OO} = \nu^{-2.5}$, un rapport signal-sur-bruit (SNR en anglais) de 34dB et des DoF $\psi_{max} = \{1.01.52.02.53.0\}\lambda$. On montre que quand le nombre d'anneaux est incrémenté, le masque optimal présente une forme similaire à la forme précédente, avec les nouveaux anneaux apparaissant près du

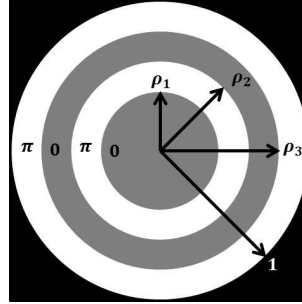


FIGURE 4.26: Exemple d'un masque de phase annulaire binaire de 4 anneaux. Les régions grises correspondent à une phase $\varphi = 0$ et les régions blanches à une phase $\varphi = \pi$.

bord du masque. On montre également, voir la figure 4.27, que pour toutes les DoF, la qualité d'image augmente rapidement avec le nombre d'anneaux puis se stabilise.

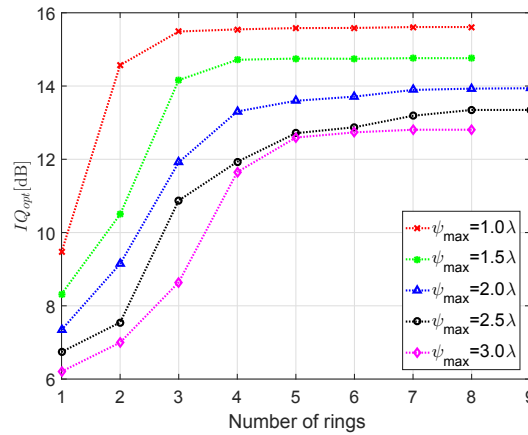


FIGURE 4.27: Comparaison des performances de masques annulaires binaires avec divers nombres d'anneaux pour $\psi_{\max} \in \{1.0, 1.5, 2.0, 2.5, 3.0\}\lambda$. Le cas où le nombre d'anneaux vaut 1 est équivalent à n'avoir aucun masque.

On a confirmé que ce comportement est conservé même si on change la PSD de la scène et en présence d'autres aberrations optiques telles que l'aberration sphérique, la coma, l'astigmatisme ou une combinaison des trois. On peut aussi observer l'effet du système hybride sur des images réelles : dans la figure 4.28 on montre les images obtenues avec un système hybride simulé avec des masques optimisés pour $\psi_{\max} = 2.0\lambda$ et un nombre d'anneaux croissant. Les images sont montrées pour une défocalisation de $\psi = \psi_{\max} = 2.0\lambda$. On observe que la qualité visuelle des images change avec le nombre d'anneaux du masque, de la même façon que la valeur de IQ : elle augmente rapidement jusqu'à 5 anneaux, il y a une amélioration marginale de 5 à 6 anneaux, de 6 à 7 anneaux quelques détails s'améliorent et pour 8 anneaux, il n'y a plus aucune différence.



FIGURE 4.28: Image et zoom de l'image de Lena obtenus avec le système hybride simulé pour la défocalisation $\psi = \psi_{\max}$ et des masques optimisés pour $\psi_{\max} = 2.0\lambda$ et pour un nombre d'anneaux croissant.

Optimisation et évaluation des divers masques de phase

Le choix du critère de performance est justifié en comparant IQ_{\min} avec d'autres critères qui apparaissent dans la littérature, comme le rapport de Strehl, la forme de la fonction de transfert de modulation (MTF en anglais) et IQ_{mean} , un critère similaire à IQ_{\min} où au lieu de maximiser la valeur de IQ_{\min} on maximise la valeur $IQ_{\text{mean}} = E_O(1/K \sum_k [MSE_k])^{-1}$. On montre qu'utiliser seulement le SR ou la MTF comme critères de performance n'est pas suffisant dans le contexte de l'imagerie hybride car ils ne prennent pas en compte la contribution du bruit et le processus de déconvolution. D'autre part, un masque optimisé par IQ_{mean} peut présenter des valeurs très hautes et très basses dans la plage de défocalisation et, par définition, la valeur de IQ la plus basse obtenue en optimisant la moyenne sera toujours plus basse qu'en optimisant le minimum.

On applique ensuite les outils d'analyse utilisés pour les BAPM aux masques de phase continus qui apparaissent communément dans la littérature, non seulement pour évaluer et comparer leurs avantages, mais aussi parce qu'en analysant leurs différences il est possible de mieux comprendre leurs propriétés.

Le premier masque analysé est le masque de phase polynomial (PPM), dont le profil est donné par les coefficients de $\varphi(x_P, y_P) = \alpha(x_P^3 + y_P^3) + \beta(x_P^2 y_P + x_P y_P^2) + \gamma(x_P^5 + y_P^5) \dots$, le masque cubique (CPM) étant un cas particulier de ce masque où seulement $\alpha \neq 0$ (Dowski and Cathey, 1995; Diaz, 2011). Pour ce masque on montre

que les valeurs croisées de degré inférieur influencent la qualité d'image finale de manière plus importante que les valeurs prises séparément.

La deuxième masque qu'on étudie est le masque de phase asphérique (APM) de profil $\varphi(\rho) = \sum_{i=1}^N \alpha_i \rho^i$, le masque quartique (QPM) étant un cas particulier de ce masque ou $\alpha_2 = -\alpha_4 \neq 0$. Ces masques ont une performance très similaire pour $N \geq 3$. En général, ces masques sont moins performants que les autres étudiés dans ce chapitre, mais ils sont populaires dans la littérature car ils permettent de corriger d'autres aberrations optiques (Robinson and Stork, 2007).

Enfin, on utilise un masque de phase de profil *free-form* (FFPM), pour lequel le profil est donné par la surface de révolution produite avec une génératrice $\varphi_{ff}(\rho_{ff})$ définie par des points d'évaluation équidistants $\rho_{ff} = \{\rho_0 = 0, \rho_1, \dots, \rho_{N-1}, \rho_N = 1\}$. Ces points sont connectés par une interpolation cubique pour former la génératrice du FFPM. Les masques optimisés de ce type tendent à avoir un profil comparable aux BAPMs quand le nombre de paramètres N augmente. Cette similarité est observée aussi au niveau des performances, où les masques optimisés pour une même DoF se comportent de manière similaire aux BAPM optimaux correspondants.

Dans la figure 4.29 on compare les performances des BAPM, PPM, APM et FFPM optimisés pour la même DoF. On voit que pour la plus faible DoF, $2\psi_{\max} = 1.5\lambda$, le BAPM fonctionne marginalement mieux que les autres masques. Pour une DoF plus grande, $2\psi_{\max} = 3.0\lambda$, le BAPM et le PPM ont des performances comparables et considérablement supérieures aux deux autres masques. Ces observations sont cohérentes avec les résultats rapportés par (Diaz, 2011).

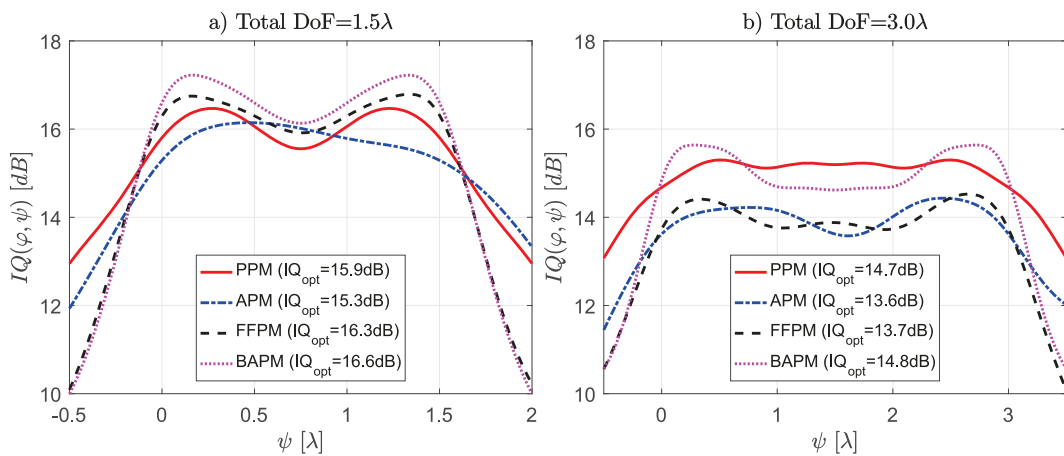


FIGURE 4.29: Comparaison des performances des masques polynomiaux, asphériques, *free-form* et binaires optimisés pour la même DoF. Les valeurs pour le BAPM et le PPM ont été décalées de ψ_{\max} de manière à ce que leur DoF totale coïncide avec celle des autres masques. a) Masques optimisés pour une DoF totale $2\psi_{\max} = 1.5\lambda$ et b) masques optimisés pour une DoF totale $2\psi_{\max} = 3.0\lambda$.

Ces observations sont confirmées aussi en analysant les fonctions de transfert de modulation effectives, $MTF_{eff} = \tilde{d} \cdot \tilde{h}$, c'est-à-dire la MTF multipliée par le filtre de Wiener de chaque masque. On voit qu'il y a une corrélation entre la performance du système hybride et sa fréquence de coupure.

Aliasing des systèmes hybrides et super-résolution

Le théorème de Shannon-Nyquist impose que pour qu'un système optique soit bien échantillonné pendant la capture numérique de l'image il doit satisfaire $\bar{\nu}_c = \nu_c/\nu_s < 0.5$: la fréquence de coupure optique ν_c doit être inférieure à la fréquence de Nyquist $\nu_s/2$. La majorité des systèmes optiques commerciaux sont conçus avec $\bar{\nu}_c > 0.5$ car ils produisent des images plus nettes. Ce sous-échantillonnage produit une périodisation de la MTF du système lors de la capture de l'image, induisant un phénomène connu sous le nom de repliement de spectre ou *aliasing* en anglais. Un exemple unidimensionnel est montré dans la figure 4.30, où le signal sinusoïdal de fréquence ν_c est sous-échantillonné par un capteur de fréquence d'échantillonnage $\bar{\nu}_c = 0.75$, qui produit un signal aliasé (donc incorrect) de période 3 fois plus grande que le signal original. Ces artefacts sont visibles quand le système optique ne respecte pas la condition de Shannon-Nyquist mais également communément quand une image numérique haute-résolution (HR) est modifiée en une image de plus basse résolution (LR) sans utilisation d'un filtre anti-aliasing.

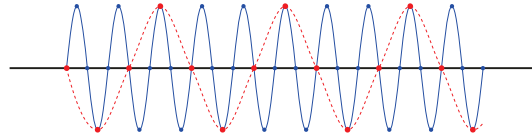


FIGURE 4.30: Aliasing d'un signal unidimensionnel sinusoïdal. La courbe bleue représente le signal sinusoïdal continu, les points bleus marquent un échantillonnage de $\bar{\nu}_c = 0.25$, les points rouges marquent un sous-échantillonnage de $\bar{\nu}_c = 0.75$. La courbe pointillée rouge représente une interpolation cubique des points sous-échantillonnés.

La technique de reconstruction numérique connue sous l'appellation de *super-résolution* (SR) utilise des images d'une même scène affectées de repliement pour augmenter la résolution du système optique. Cette technique dépend de l'obtention de plusieurs images de la même scène avec des décalages subpixelliques de manière à ce qu'une quantité suffisante d'information relative aux hautes fréquences spatiales de la scène soit présente. Le diagramme de la figure 4.31, repris de (Champagnat, Le Besnerais, and Kulcsár, 2009), montre les étapes d'un tel système. On commence à gauche par le processus de génération des scènes décalées, avec passage par le système optique de K images, l'échantillonnage et l'ajout de bruit. Les images LR obtenues, F_{ik} , sont ensuite reconstruites par filtrage linéaire pour obtenir une image SR \hat{O} .

L'algorithme choisi pour la SR est ici le *shift-and-add* (SA) où, après avoir fixé un facteur de SR M (PMF en anglais, qui fixe le ratio entre la taille de l'image super-résolue et celle de l'image LR), on affecte chaque pixel LR F_{ik} , où i est l'index du pixel LR et k est l'index de l'image dans la séquence, à une position i' dans l'image super-résolue \hat{O} :

$$\hat{O}(i'/M) = \sum_i \mathbf{F}_i^T \mathbf{w}(i'/M - i), \quad (4.29)$$

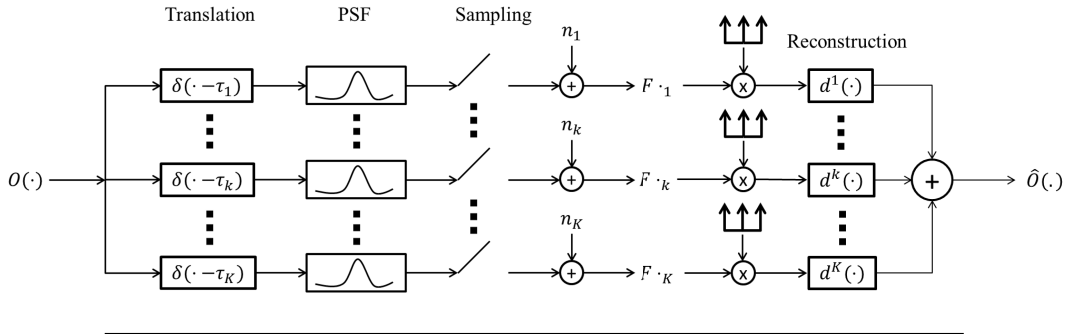


FIGURE 4.31: Schéma de simulation d'une séquence d'images et de reconstruction SR par l'algorithme de *shift-and-add*.

où $\mathbf{F}_i = [F_{i1}, \dots, F_{iK}]$ et $\mathbf{w}(\mathbf{x}) = [w^1(x), \dots, w^K(x)]$ est un filtre multicanal chargé d'additionner les pixels des images de la séquence LR dans l'image super-résolue et d'appliquer un filtre de Wiener pour prendre en compte la PSF du système optique. Les décalages, estimés au préalable, sont supposés connus. Dans la figure 4.32 on montre une image affectée d'aliasing correspondant à un facteur de sous-échantillonnage de $2\bar{\nu}_c = 4$ et l'image SR reconstruite à partir de 64 images LR et un PMF de $M = 4$. On peut voir que l'image SR est passée d'une résolution de 1 lpp (lignes par pixel) à une résolution de 0.375 lpp (il présente de l'aliasing au point marqué 3.75). L'image SR a récupéré les hautes fréquences jusqu'à 0.8 lpp, et les plus hautes fréquences ont été perdues à cause du bruit et de la MTF du détecteur.

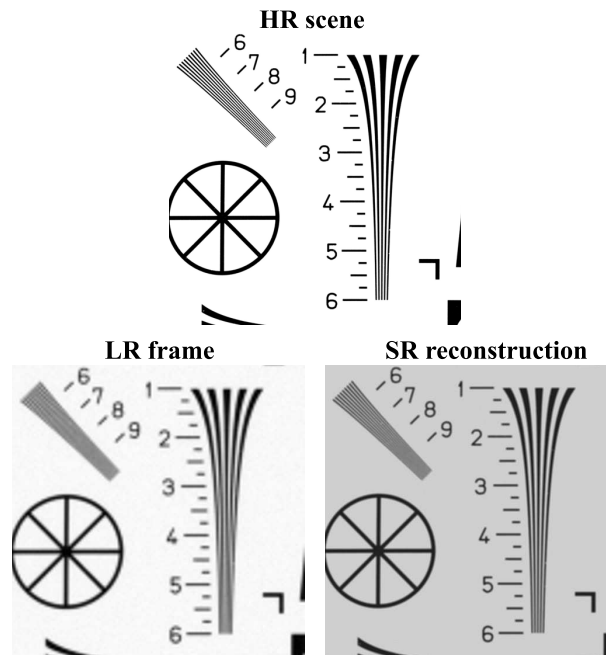


FIGURE 4.32: Simulation des images dans un système de SR : (en haut) la scène nette, (en bas à gauche) image basse résolution aliasée avec $2\bar{\nu}_c = 4$, (en bas à droite) image reconstruite par l'algorithme SA

Les masques de phase fonctionnent comme des filtres passe-bas sur des systèmes limités par la diffraction, réduisant en pratique les phénomènes de repliement spectral. Il est donc intéressant d'évaluer la pertinence de la super-résolution sur des systèmes où l'échantillonnage ne respecte pas la condition de Shannon-Nyquist,

mais conçus pour l'augmentation de la profondeur de champ. Dans la figure 4.33 on montre les images reconstruites par SA et déconvoluées par un filtre de Wiener conçu pour une MTF du système optique correctement échantillonnée. Dans les deux cas, on a réussi à récupérer des hautes fréquences de la scène grâce à la SR. On voit qu'il y a certains artefacts présents dans les images, particulièrement pour $\psi = 0$, lesquels probablement apparaissent car le filtre de Wiener utilisé est un filtre générique adapté uniquement à l'augmentation de la profondeur de champ sans prendre en compte la super-résolution.

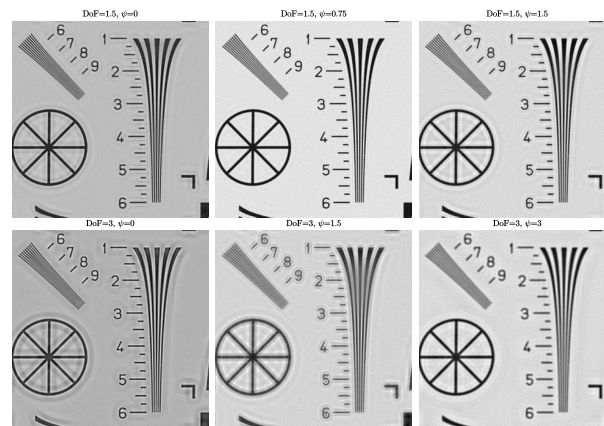


FIGURE 4.33: Simulation des images dans un système avec super-résolution incluant des BAPM : (en haut) masque optimisé pour une DoF de $\psi_{\max} = 1.5\lambda$ (en bas) masque optimisé pour une DoF de $\psi_{\max} = 3.0\lambda$. Les images sont montrées pour des défocalisations de $\psi \in \{0, \psi_{\max}/2, \psi_{\max}\}$

On a démontré que les systèmes hybrides pour l'augmentation de la profondeur de champ pouvaient être utilisés en conjonction avec des systèmes sous-échantillonnés et traités par super-résolution. À notre connaissance, cela n'a jamais été fait, mais suite à cette preuve de faisabilité, il serait intéressant de considérer le problème de SR global pour un système à extension de DoF, et de concevoir également des filtres de déconvolution mieux adaptés à l'augmentation de la profondeur de champ dans le cas de méthodes de SR de type shift-and-add.

Cette problématique de super-résolution a été explorée suite à une période de détachement chez le partenaire industriel de la thèse, KLA-Tencor, à Louvain (Belgique). J'y ai appliqué l'algorithme shift-and-add sur des séquences d'images expérimentales pour évaluer la pertinence d'utiliser la super-résolution dans le cadre de l'inspection industrielle. J'ai réussi à doubler la résolution d'un système d'inspection industrielle de semi-conducteurs sur un banc d'essai, ce qui permet de détecter des imperfections précédemment invisibles par optique traditionnelle. Dans la figure 4.34 on montre le micro-composant étudié, un zoom dans une de ses imperfections connues, observable seulement au microscope et invisible dans le système conventionnel. On a utilisé 64 images de la scène et un filtre de Wiener générique pour reconstruire les images montrées en bas. Dans le cas $M = 3$, les détails plus fins de l'image sont encore flous, mais la rayure au milieu de l'image est bien visible. L'image pour $M = 8$ l'image est plus nette, mais ne donne pas de nouvelles informations concernant la rayure.

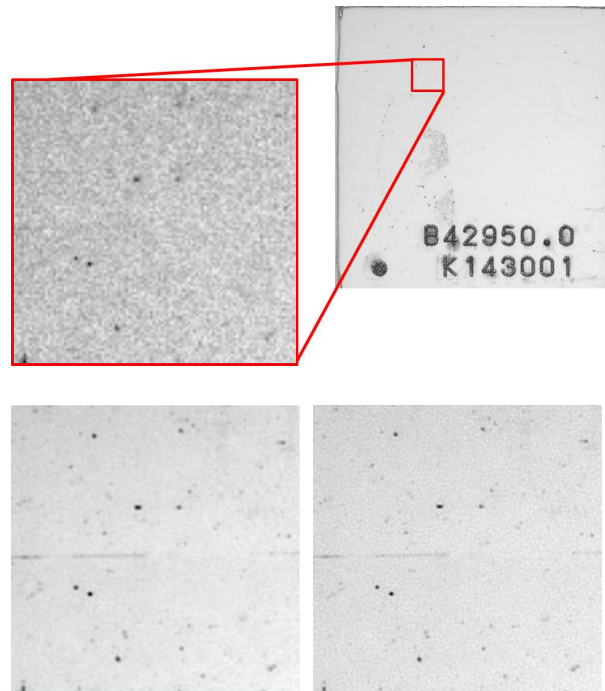


FIGURE 4.34: Exemple d'une scène réelle améliorée par la super-résolution (algorithme SA), obtenue chez le partenaire industriel de la thèse KLA-Tencor. En haut : l'image LR du micro-composant. En bas : images récupérées pour $PMF=3$ (à gauche) et $PMF=8$ (à droite).

Conclusions

Le travail développé dans cette thèse présente les caractéristiques et les limites de performance des systèmes hybrides avec masques de phase pour l'augmentation de la profondeur de champ. On a concentré les efforts sur les BAPM, qui possèdent des caractéristiques intéressantes. On a démontré que la performance des systèmes hybrides avec les BAPM augmente avec le nombre d'anneaux, puis se stabilise rapidement. Ce comportement est intéressant pour la fabrication des masques, car l'utilisation d'un nombre limité d'anneaux permet de gagner en temps de fabrication et en coût de production.

On a aussi comparé divers masques de phase et critères d'optimisation. On a montré que le critère de performance IQ est plus adapté que d'autres critères plus conventionnels, tels que le rapport de Strehl ou la MTF. On a montré que les BAPM ont une performance supérieure à plusieurs masques continus de la littérature. On a montré enfin qu'il existe une corrélation entre la fréquence de coupure du masque et la qualité d'image.

Dans la dernière partie de la thèse, on a montré la faisabilité d'utiliser des techniques de super-résolution dans deux contextes différents : l'inspection industrielle et l'augmentation de la profondeur de champ avec des masques de phase. On a montré que les masques de phase permettent l'utilisation de techniques de super-résolution même si le filtre de déconvolution n'est pas optimal. Pour l'inspection industrielle, on a réussi à trouver des imperfections dans les micro-composants étudiés qui étaient invisibles pour un système conventionnel.

Les résultats de cette étude ont permis de répondre à plusieurs questions de co-conception optique autour des masques de phase, mais d'autres questions restent en suspens : trouve-t-on des limites de performance similaires dans les autres masques de phase ? Est-il possible d'optimiser encore plus les systèmes hybrides pour l'augmentation de la DoF afin de prendre en compte d'autres traitements, comme la super-résolution ? Il serait aussi intéressant de réaliser les masques optimaux conçus dans cette thèse afin de corroborer de manière expérimentale les résultats observés par simulation.

Bibliography

- Borman, Sean and Robert L Stevenson (1998). "Super-resolution from image sequences—a review". In: *Circuits and Systems, 1998. Proceedings. 1998 Midwest Symposium on*. IEEE, pp. 374–378.
- Born, M., E. Wolf, and A.B. Bhatia (1999). *Principles of Optics: Electromagnetic Theory of Propagation, Interference and Diffraction of Light*. Cambridge University Press. ISBN: 9780521642224. URL: <https://books.google.fr/books?id=aoX0gYLuENoC>.
- Burcklen, M-A et al. (2015). "Experimental demonstration of extended depth-of-field f/1.2 visible High Definition camera with jointly optimized phase mask and real-time digital processing". In: *Journal of the European Optical Society-Rapid publications* 10.
- Caron, Nicolas and Yunlong Sheng (2008). "Polynomial phase masks for extending the depth of field of a microscope". In: *Applied optics* 47.22, E39–E43.
- Castro, Albertina and Jorge Ojeda-Castañeda (2004). "Asymmetric phase masks for extended depth of field". In: *Applied optics* 43.17, pp. 3474–3479.
- Cathey, W Thomas and Edward R Dowski (2002). "New paradigm for imaging systems". In: *Applied optics* 41.29, pp. 6080–6092.
- Champagnat, Frédéric, Guy Le Besnerais, and Caroline Kulcsár (2009). "Statistical performance modeling for superresolution: a discrete data-continuous reconstruction framework". In: *JOSA A* 26.7, pp. 1730–1746.
- Courant, Richard and David Hilbert (1965). *Methods of mathematical physics*. Vol. 1. CUP Archive, p. 474.
- Demenikov, Mads and Andrew R Harvey (2010). "Image artifacts in hybrid imaging systems with a cubic phase mask". In: *Optics express* 18.8, pp. 8207–8212.
- Diaz, Frédéric (2011). "Système d'imagerie hybride par codage de pupille". PhD thesis. Paris 11.
- Diaz, Frédéric et al. (2009). "Increase in depth of field taking into account deconvolution by optimization of pupil mask". In: *Optics letters* 34.19, pp. 2970–2972.
- Diaz, Frédéric et al. (2011). "Real-time increase in depth of field of an uncooled thermal camera using several phase-mask technologies". In: *Optics letters* 36.3, pp. 418–420.
- Dowski, Edward R and W Thomas Cathey (1995). "Extended depth of field through wave-front coding". In: *Applied optics* 34.11, pp. 1859–1866. URL: <https://www.osapublishing.org/ao/abstract.cfm?uri=ao-34-11-1859>.
- Elad, Michael and Yacov Hel-Or (2001). "A fast super-resolution reconstruction algorithm for pure translational motion and common space-invariant blur". In: *IEEE Transactions on Image Processing* 10.8, pp. 1187–1193.
- Endler, John A (1986). *Natural selection in the wild*. 21. Princeton University Press.
- Falcón, Rafael, Caroline Kulcsar, and François Goudail (2016). "How Many Rings for Binary Phase Masks Co-optimized for Depth of Field Extension?" In: *Computational Optical Sensing and Imaging*. Optical Society of America, CTh1D–5.
- Falcón, Rafael et al. (2017). "Performance limits of binary annular phase masks code-signed for depth-of-field extension". In: *Optical Engineering* 56.6, pp. 065104–065104.

- Forbes, GW (2010). "Robust and fast computation for the polynomials of optics". In: *Optics express* 18.13, pp. 13851–13862.
- Gies, Dennis and Yahya Rahmat-Samii (2003). "Particle swarm optimization for reconfigurable phase-differentiated array design". In: *Microwave and Optical Technology Letters* 38.3, pp. 168–175.
- Guizar-Sicairos, Manuel, Samuel T Thurman, and James R Fienup (2008). "Efficient subpixel image registration algorithms". In: *Optics letters* 33.2, pp. 156–158.
- Hardie, Russell C, Kenneth J Barnard, and Ernest E Armstrong (1997). "Joint MAP registration and high-resolution image estimation using a sequence of undersampled images". In: *IEEE Transactions on Image Processing* 6.12, pp. 1621–1633.
- Hazewinkel, Michiel (2001). "Spline interpolation, *Encyclopedia of Mathematics*". Springer. ISBN: 1402006098. URL: http://www.encyclopediaofmath.org/index.php?title=Spline_interpolation&oldid=11892.
- Hu, Jiangfei et al. (2013). "Comparative study of wavefront coding imaging with rotational and non-rotational symmetric phase masks". In: *ISPDI 2013-Fifth International Symposium on Photoelectronic Detection and Imaging*. International Society for Optics and Photonics, 89110Z–89110Z.
- Hudyma, Russell (2000). *High numerical aperture ring field projection system for extreme ultraviolet lithography*. US Patent 6,033,079.
- Landeau, Stéphane (2014). "Evaluation of super-resolution imager with binary fractal test target". In: *Electro-Optical and Infrared Systems: Technology and Applications XI*. Vol. 9249.
- Liu, Jiang et al. (2016). "Phase only pupil filter design using Zernike polynomials". In: *Journal of the Optical Society of Korea* 20.1, pp. 101–106.
- Mahajan, Virendra N (1982). "Strehl ratio for primary aberrations: some analytical results for circular and annular pupils". In: *JOSA* 72.9, pp. 1258–1266.
- Maréchal, André (1947). "Étude des effets combinés de la diffraction et des aberrations géométriques sur l'image d'un point lumineux". In: *Rev. Opt* 26, pp. 257–277.
- Mezouari, Samir and Andrew R Harvey (2002). "Primary aberrations alleviated with phase pupil filters". In: *Proc. SPIE*. Vol. 4768, pp. 21–31.
- Mezouari, Samir, Gonzalo Muyo, and Andrew R Harvey (2006). "Circularly symmetric phase filters for control of primary third-order aberrations: coma and astigmatism". In: *JOSA A* 23.5, pp. 1058–1062.
- Mino, M and Y Okano (1971). "Improvement in the OTF of a defocused optical system through the use of shaded apertures". In: *Applied Optics* 10.10, pp. 2219–2225.
- Ojeda-Castañeda, Jorge, P Andres, and A Diaz (1986). "Annular apodizers for low sensitivity to defocus and to spherical aberration". In: *Optics Letters* 11.8, pp. 487–489.
- Prasad, Sudhakar et al. (2004). "Pupil-phase optimization for extended-focus, aberration-corrected imaging systems". In: *Optical Science and Technology, the SPIE 49th Annual Meeting*. International Society for Optics and Photonics, pp. 335–345.
- Robinson, M Dirk and David G Stork (2007). "Joint design of lens systems and digital image processing". In: *Contract Proceedings 2006*. International Society for Optics and Photonics, 63421G–63421G.
- Ruderman, Daniel L (1997). "Origins of scaling in natural images". In: *Vision research* 37.23, pp. 3385–3398.
- Sauceda, Angel and Jorge Ojeda-Castañeda (2004). "High focal depth with fractional-power wave fronts". In: *Optics letters* 29.6, pp. 560–562.

- Schultz, Richard R and Robert L Stevenson (1996). "Extraction of high-resolution frames from video sequences". In: *IEEE transactions on image processing* 5.6, pp. 996–1011.
- Sherif, Sherif S, W Thomas Cathey, and Ed R Dowski (2004). "Phase plate to extend the depth of field of incoherent hybrid imaging systems". In: *Applied optics* 43.13, pp. 2709–2721.
- Shi, Yuhui and Russell Eberhart (1998). "A modified particle swarm optimizer". In: *Evolutionary Computation Proceedings, 1998. IEEE World Congress on Computational Intelligence., The 1998 IEEE International Conference on*. IEEE, pp. 69–73.
- Shokooch-Saremi, Mehrdad and Robert Magnusson (2007). "Particle swarm optimization and its application to the design of diffraction grating filters". In: *Optics letters* 32.8, pp. 894–896.
- Smith, Warren J (1966). *Modern optical engineering*. Tata McGraw-Hill Education, pp. 64–71.
- Suematsu, Y et al. (2008). "The solar optical telescope of Solar-B (Hinode): the optical telescope assembly". In: *The Hinode Mission*. Springer, pp. 143–166.
- Tsai, RY and TS Huang (1984). "Multiframe image restoration and registration". In: *Advances in Computer Vision and Image Processing*, JAL Press Inc.
- Tucker, Allen B (2004). *Computer science handbook*, pp. 39–1–39–31.
- Tucker, Sara C, W Thomas Cathey, and Edward R Dowski (1999). "Extended depth of field and aberration control for inexpensive digital microscope systems". In: *Optics Express* 4.11, pp. 467–474.
- Vipress (2017). *Le marché mondial des semiconducteurs a bondi de 20,8premier semestre*. URL: <http://www.vipress.net/marche-mondial-semiconducteurs-a-bondi-de-208-premier-semestre/> (visited on 08/23/2017).
- Wiener, Norbert (1949). *Extrapolation, interpolation, and smoothing of stationary time series*. Vol. 7. MIT press Cambridge, MA.
- Yang, Qingguo, Liren Liu, and Jianfeng Sun (2007). "Optimized phase pupil masks for extended depth of field". In: *Optics Communications* 272.1, pp. 56–66.
- Yıldız, Ali Rıza (2009). "A novel particle swarm optimization approach for product design and manufacturing". In: *The International Journal of Advanced Manufacturing Technology* 40.5, pp. 617–628.
- Zhao, Hui and Yingcai Li (2010). "Optimized sinusoidal phase mask to extend the depth of field of an incoherent imaging system". In: *Optics letters* 35.2, pp. 267–269.
- Zhao, Tingyu et al. (2014). "Axial intensity distribution analysis for a depth-of-field-extended optical system using a low-frequency binary phase mask". In: *Applied optics* 53.17, pp. 3782–3786.

Title : Co-design of optical systems with phase masks for depth of field extension: performance evaluation and contribution of superresolution

Keywords : Computational imaging, Optical co-design, Superresolution

Abstract : Phase masks are wavefront encoding devices typically situated at the aperture stop of an optical system to engineer its point spread function (PSF) in a technique commonly known as wavefront coding. These masks can be used to extend the depth of field (DoF) of imaging systems without reducing the light throughput by producing a PSF that becomes more invariant to defocus; however, the larger the DoF the more blurred the acquired raw image so that deconvolution has to be applied on the captured images. Thus, the design of the phase masks has to take into account image processing in order to reach the optimal compromise between invariance of PSF to defocus and capacity to deconvolve the image. This joint design approach has been introduced by Cathey and Dowski in 1995 and refined in 2002 for continuous-phase DoF enhancing masks and generalized by Robinson and Stork in 2007 to correct other optical aberrations. In this thesis we study the different aspects of phase mask optimization for DoF extension, such as the different performance criteria and the relation of these criteria with the different mask parameters. We use the so-called image quality (IQ), a mean-square error based criterion defined by Diaz et al., to co-design different phase masks and evaluate their performance. We then compare the relevance of the IQ criterion against other optical design metrics, such as the Strehl ratio, the modulation transfer function (MTF) and others. We focus in particular on the binary annular phase masks, their performance for various conditions, such as the desired DoF range, the number of optimization parameters, presence of aberrations and others. We use then the analysis tools used for the binary phase masks for continuous-phase masks that appear commonly in the literature, such as the polynomial-phase masks. We extensively compare these masks to each other and the binary masks, not only to assess their benefits, but also because by analyzing their differences we can understand their properties. Phase masks function as a low-pass filter on diffraction limited systems, effectively reducing aliasing. On the other hand, the signal processing technique known as superresolution uses several aliased frames of the same scene to enhance the resolution of the final image beyond the sampling resolution of the original optical system. Practical examples come from the works made during a secondment with the industrial partner KLA-Tencor in Leuven, Belgium. At the end of the manuscript we study the relevance of using such a technique alongside phase masks for DoF extension.



Titre : Co-conception des systèmes optiques avec masques de phase pour l'augmentation de la profondeur du champ : évaluation de la performance et contribution de la super-résolution

Keywords : Imagerie numérique, Co-conception Optique, Super-résolution)

Résumé : Les masques de phase sont des dispositifs réfractifs situés généralement au niveau de la pupille d'un système optique pour en modifier la réponse impulsionnelle (PSF en anglais), par une technique habituellement connue sous le nom de codage de front d'onde. Ces masques peuvent être utilisés pour augmenter la profondeur du champ (DoF en anglais) des systèmes d'imagerie sans diminuer la quantité de lumière qui entre dans le système, en produisant une PSF ayant une plus grande invariance à la défocalisation. Cependant, plus le DoF est grand plus l'image acquise est floue et une opération de déconvolution doit alors lui être appliquée. Par conséquent, la conception des masques de phase doit prendre en compte ce traitement pour atteindre le compromis optimal entre invariance de la PSF à la défocalisation et qualité de la déconvolution. Cette approche de conception conjointe a été introduite par Cathey et Dowski en 1995 et affinée en 2002 pour des masques de phase continus puis généralisée par Robinson et Stork en 2007 pour la correction d'autres aberrations optiques. Dans cette thèse sont abordés les différents aspects de l'optimisation des masques de phase pour l'augmentation du DoF, tels que les critères de performance et la relation entre ces critères et les paramètres des masques. On utilise la qualité d'image (IQ en anglais), une méthode basée sur l'écart quadratique moyen définie par Diaz et al., pour la co-conception des divers masques de phase et pour évaluer leur performance. Nous évaluons ensuite la pertinence de ce critère IQ en comparaison d'autres métriques de conception optique, comme par exemple le rapport de Strehl ou la fonction de transfert de modulation (MTF en anglais). Nous nous concentrons en particulier sur les masques de phase annulaires binaires, l'étude de leur performance pour différents cas comme l'augmentation du DoF, la présence d'aberrations ou l'impact du nombre de paramètres d'optimisation. Nous appliquons ensuite les outils d'analyse exploités pour les masques binaires aux masques de phase continus qui apparaissent communément dans la littérature, comme les masques de phase polynomiaux. Nous avons comparé de manière approfondie ces masques entre eux et aux masques binaires, non seulement pour évaluer leurs avantages, mais aussi parce qu'en analysant leurs différences il est possible de comprendre leurs propriétés. Les masques de phase fonctionnent comme des filtres passe-bas sur des systèmes limités par la diffraction, réduisant en pratique les phénomènes de repliement spectral. D'un autre côté, la technique de reconstruction connue sous l'appellation de "super-résolution" utilise des images d'une même scène perturbées par du repliement de spectre pour augmenter la résolution du système optique original. Les travaux réalisés durant une période de détachement chez le partenaire industriel de la thèse, KLA-Tencor à Louvain, Belgique, illustrent le propos. À la fin du manuscrit nous étudions la pertinence de la combinaison de cette technique avec l'utilisation de masques de phase pour l'augmentation du DoF.

